CurateND

UNIVERSITY OF NOTRE DAME | HESBURGH LIBRARIES

Flow Field and Acoustic Measurements of a Blunt Trailing Edge

Daniel W Shannon

Publication Date

20-04-2007

License

This work is made available under a All Rights Reserved license and should only be used in accordance with that license.

Citation for this work (American Psychological Association 7th edition)

Shannon, D. W. (2007). *Flow Field and Acoustic Measurements of a Blunt Trailing Edge* (Version 1). University of Notre Dame. https://doi.org/10.7274/4t64gm82f29

This work was downloaded from CurateND, the University of Notre Dame's institutional repository.

For more information about this work, to report or an issue, or to preserve and share your original work, please contact the CurateND team for assistance at curate@nd.edu.

FLOW FIELD AND ACOUSTIC MEASUREMENTS OF A BLUNT TRAILING EDGE

A Dissertation

Submitted to the Graduate School

of the University of Notre Dame

in Partial Fulfillment of the Requirements

for the Degree of

Doctor of Philosophy

by

Daniel W. Shannon, M.S. A.E., B.S. Eng.

Scott C. Morris, Director

Graduate Program in Aerospace and Mechanical Engineering

Notre Dame, Indiana

April 2007

FLOW FIELD AND ACOUSTIC MEASUREMENTS

OF A BLUNT TRAILING EDGE

Abstract

by

Daniel W. Shannon

This dissertation presents experimental results regarding the phenomenon of trailing edge noise. The objective of the present research was to experimentally measure flow field and acoustic variables in order to develop an understanding of the mechanisms that generate trailing edge noise in incompressible, high Reynolds number flows. This includes the measurement of the local velocity field, the unsteady surface pressure, and the radiated sound. These data have supplied a unique database of both the turbulence and the radiated far field pressure. In addition, two-component velocity measurements were acquired using Particle Image Velocimetry (PIV) in order to spatially resolve the local velocity field. The data show velocity field realizations that were typical of wake flow containing an asymmetric periodic vortex shedding. Beamforming methods were utilized in conjunction with a pair of 40 microphone arrays to isolate trailing edge noise from unwanted tunnel noise. The measured acoustic sources show good agreement with numerical results obtained through LES.

DEDICATION

I dedicate this work to my wife Sarah and my two children Eion and Eva. Your constant love and support has been an essential part of this process. Thank you and I love you.

CONTENTS

FIGURES v

SYMBOLS xi

CHAPTER 1: INTRODUCTION AND MOTIVATION. 1

CHAPTER 2: AEROACOUSTIC THEORY 5
2.1: Lighthill's Equation 6
2.2: Curle's Equation 7
2.3: Ffowcs Williams and Hawkings Equation 8
2.4: Vortex Sound 9
2.5: Half-Plane Green's Function 10
2.6: Prediction of Trailing Edge Noise 11
2.6.1: Predicting Unsteady Surface Pressures from Flow Measurements 12
2.6.2: Predicting Sound from Measured Surface Pressures 13
2.6.3: Predicting Sound from Flow Measurements 14

CHAPTER 3: PARTICLE IMAGE VELOCIMETRY MEASURMENTS 16
3.1: Flow Visualization 19
3.2: Instantaneous Results 20
3.3: Time Averaged Results. 22
3.4: Phase Averaged Results 27
3.4.1: Algorithm. 28
2.6.3: Predicting Sound from Flow Measurements 31

CHAPTER 4: EXPERIMENTAL SETUP & BOUNDARY CONDITION MEASUREMENTS 40
4.1: Anechoic Wind Tunnel. 40
4.2: Boundary Condition Measurements 44
4.2.1: Pressure Distribution 45
4.2.2: Boundary Layer Measurements 46
4.2.3: Near Wake Turbulence 52
4.2.4: Vortex Shedding Frequency 56

CHAPTER 5: UNSTEADY SURFACE PRESSURE MEASUREMENTS 51
5.1: Unsteady Surface Pressure Spectra 52
5.2: Spanwise Correlation Length Scales 52
5.3: Phase Averaged Surface Pressure. 54

CHAPTER 6: BEAMFORMING METHODS. 57
6.1: Processing Techniques 57
6.1.1: Delay-Sum Beamforming 58
6.1.2: Weighted CSM Beamforming 59
6.1.3: DAMAS 62
6.2: Array Calibration 65
6.3: Simulated Monopole Source. 66
6.4: Measured Array Data 67
6.4.1: Array Data Acquisition Parameters 67
6.4.2: Monopole Source Test 68
6.4.3: AWT Background Noise 70

CHAPTER 7: TRAILING EDGE SOUND MEASUREMENTS 83
7.1: Beamforming Maps 84
7.2: Trailing Edge Spectra 85
7.3: Comparison with Numerical Results 93
7.4: Acoustic-Surface Pressure Correlations 95
7.5: Phase Averaged Acoustic Pressure. 97

CHAPTER 8: OPTIMIZED TRAILING EDGE SOUD MEASUREMENTS 99
8.1: Beamforming Maps for Optimized Trailing Edge 100
8.2: Optimized Trailing Edge Spectra 101

CHAPTER 9: CONCLUSIONS 108

REFERENCES 112

FIGURES

1.1 Schematic of trailing edge geometry. 3

2.1 Illustration of relationships between unsteady surface pressure, turbulence and far field acoustics in trailing edge flows 5

2.2 Nonzero components of $\nabla_y G(\vec{x}, \vec{y}, f)$ for an infinite half-plane. The observation location was $\vec{x}k_o = \{0, 10, 0\}$ with respect to the origin. 11

3.1 Schematic of PIV experimental setup. 17

3.2 Schematic of particle diffuser. 18

3.3 Two realizations of streakline flow visualization 20

3.4 Instantaneous PIV realization. 21

3.5 Time averaged PIV results.. 23

3.6 Root mean square velocities. 24

3.7 Time averaged Reynolds stress. 25

3.8 Two-point correlation coefficients for with respect to the trailing edge. 26

3.9 The streamwise average of the first four eigenmodes in the downstream wake. 29

3.10 Second eigenmode of Karhunen-Loeve decomposition compared to a Taylor vortex profile. 30

3.11 Second coefficient for KL decomposition for the vector map illustrated in Figure 3.4. 30

3.12 Histogram of 1000 PIV realizations sorted into 10 phase bins. 31

3.13 Contours of phase averaged streamwise velocity with streamlines.. 32

3.14 Contours phase averaged vorticity with streamlines. 33

3.15 Root mean square of phase fluctuating streamwise velocity. 34

3.16 Root mean square of phase fluctuating normal velocity. 34

3.17 Contours of phase averaged Reynolds stress. 35

3.18 Two-point correlation coefficient for phase fluctuating streamwise velocity. 36

3.19 Two-point correlation coefficient for phase fluctuating normal velocity. 37

3.20 Turbulent length scale related to the phase fluctuating component of streamwise velocity plotted with the values of $\omega_z(\phi)$ and $v_{rms}(\phi)$ at $\vec{x}/y_f = \{0.5, 0\}$. Two cycles are shown. 38

4.1 Sketch of the Anechoic Wind Tunnel at Notre Dame. Flow is from left to right. . . . 41

4.2 Comparison of acoustic spectra for both the old and new collector designs in 1/3rd octave bands. 42

4.3 Stretched logarithmic microphone placement for phase acoustic array. The array size is 120cm by 60cm. 43

4.4 Model foil surface pressure distribution compared to the data of Blake (1975). 46

4.5 Boundary layer profiles for suction side of model. The images on the left show the mean components and the images on the right show the rms components 48

4.6 Evolution of boundary layer parameters over the suction side of model. 49

4.7 Example Clauser plot for suction side boundary layer at x/c = 0.78. 50

4.8 Evolution of wall skin friction for the suction side boundary layer. 51

4.9 Boundary layer profiles for pressure side of model including mean velocity, turbulent velocity, and Reynolds stress. 52

4.10 Evolution of boundary layer parameters over the pressure side of model.. 53

4.11 Evolution of wall skin friction for the pressure side boundary layer.. 53

4.12 Mean streamwise and normal velocity components for Re = 1.9×10^6 in the near wake of the trailing edge 54

4.13 Root mean square streamwise and normal velocity components for Re = 1.9×10^6 in the near wake of the trailing edge 54

4.14 Reynolds stress profiles for Re = 1.9×10^6 in the near wake of the trailing edge . . . 55

4.15 Non-Dimensionalization parameter yf in the near wake of the trailing edge. 56

5.1 Spanwise surface pressure array. Dimensions are in centimeters. 57

5.2 Unsteady surface pressure spectra in boundary layer at sensor location M. 58

5.3 Spectra of the unsteady surface pressure for the spanwise sensor array for *Re* = 1.9×10^6. 59

5.4 Spanwise coherence length scale at vortex shedding. 60

5.5 Phase fluctuating part of broadband unsteady surface pressure signal. Referenced to the broadband root mean square pressure. 62

6.1 The point spread function or directivity pattern for the microphone array shown in Figure 2 at a distance of 170.5cm.. 61

6.2 Array beamwidth as a function of acoustic wavelength for both the x and y directions. 62

6.3 Error associated with each beamforming method for speaker data. 69

6.4 Background Sound Pressure Levels in empty AWT test section with no flow. 71

6.5 Beamforming (a-d) and DAMAS (e-h) maps of tunnel noise with an empty test section at U_∞^5 =30.5m/s in AWT. Flow is from left to right 72

6.6 Sound Pressure Levels in empty AWT test section at $U_\infty = 30.5 m/s$ for an integration bin width of 19.53Hz 73

6.7 Optimal values of n for velocity scaling of tunnel noise with an empty test section. 74

7.1 Beamforming (a-d) and DAMAS (e-h) maps for pressure side phased array at $Re_c = 1.9x10^6$. Flow is from left to right. 84

7.2 Beamforming (a-d) and DAMAS (e-h) maps for suction side phased array at $Re_c = 1.9x10^6$. Flow is from left to right. 84

7.3 Example of combined beamforming method spectra compared to that of a single microphone for trailing edge data at Re = $1.3x10^6$ 87

7.4 Example of combined beamforming method spectra compared to that of a single microphone for trailing edge data at Re = $1.9x10^6$. 87

7.5 Comparison between trailing edge spectra obtained from the pressure and suction side arrays at Re = $1.9x10^6$. 88

7.6 Trailing edge spectral density vs. scaled frequency for both arrays at Reynolds numbers ranging from $1.3x10^6$ to $1.9x10^6$ 89

7.7 Optimal value of n for Un scaling of trailing edge noise for both arrays. 91

7.8 Trailing edge spectral density scaled as U_∞^5 for pressure side array at Reynolds numbers ranging from $1.3x10^6$ to $1.9x10^6$ 92

7.9 Trailing edge spectral density scaled as U_∞^5 for suction side array at Reynolds numbers ranging from $1.3x10^6$ to $1.9x10^6$. 93

7.10 Optimal value of *n* for U^n scaling of trailing edge noise only for Reynolds numbers below $1.7x10^6$. 94

7.11 Comparison of experimental acoustic spectra to LES the prediction of trailing edge noise at Re = $1.9x10^6$.. 94

7.12 Coherence between beamformed acoustic signal and two unsteady surface pressure sensors located on pressure and suction side of sharp trailing edge 96

7.13 Broadband sound as a function of vortex shedding phase. Referenced to the broadband root mean square pressure 98

8.1 Sketch of optimized trailing edge geometry. 99

8.2 Beamforming (a-d) and DAMAS (e-h) maps for optimized trailing edge on pressure side phased array at $Re_c = 1.9x10^6$. Flow is from left to right 101

8.3 Beamforming (a-d) and DAMAS (e-h) maps for optimized trailing edge on suction side phased array at $Re_c = 1.9x10^6$. Flow is from left to right 101

8.4 Optimized trailing edge spectra compared to that of a single microphone for trailing edge data at Re = $1.3x10^6$. 102

8.5 Optimized trailing edge spectra compared to that of a single microphone for trailing edge data at Re = $1.9x10^6$. 103

8.6 Comparison between the optimized trailing edge spectra obtained from the pressure and suction side arrays at Re = $1.9x10^6$. 104

8.7 Optimized trailing edge spectral density vs. scaled frequency for both arrays at Reynolds numbers ranging from $1.3x10^6$ to $1.9x10^6$. 105

8.8 Best value of n for Un scaling of optimized trailing edge noise for both arrays. . . . 105

8.9 Optimized trailing edge spectral density scaled as U_∞^5 for pressure side array at Reynolds numbers ranging from 1.3×10^6 to 1.9×10^6. 106

8.10 Optimized trailing edge spectral density scaled as U_∞^5 for suction side array at Reynolds numbers ranging from 1.3×10^6 to 1.9×10^6. 107

SYMBOLS

English symbols

A	Cross-Spectral Matrix (CSM)
A_{corr}	Corrected CSM
$a_i(x)\|_{t_o}$	Projection of eigenmode $\Phi_i(y)$ onto instantaneous velocity field
B	Total enthalpy
BW	Array beamwidth
$b(\grave{x})$	Beamforming expression
C_f	Skin friction coefficient
C_p	Coefficient of pressure
$\grave{C}(\grave{x})$	Propagation vector
c	Model chord
c_o	Speed of sound
D_{cal}	Diagonal correction matrix
f	Frequency
f_{shed}, ω_{shed}	Shedding frequency
$G(\grave{x}, \grave{y}, f)$	Acoustic Green's function (wave equation)
$G_p(\grave{x}, \grave{y}, f)$	Green's function associated with Poisson's equation
G_{xx}	Power Spectral Density
H	Boundary layer shape factor

h	Average microphone self-noise
$K(\omega)$	Array calibration factor
k_o	Acoustic wavenumber
M_∞	Freestream Mach number
n	Power velocity scaling
n_i	Normal vector to surface
$\vec{n}_a$	Normal vector to array plane
p	Pressure
p_a	Acoustic Pressure
$psf(\vec{x}_b, \vec{x}_s)$	Point Spread Function (PSF)
p_{tonal}	Tonal contribution of pressure
p_{hp}	Broadband contribution of pressure
$\tilde{p}_{hp}$	Phase average of p_{hp}
$q(\vec{x}_s)$	Acoustic source at $\vec{x}_s$
q_∞	Dynamic pressure
Re	Reynolds number based on model chord
Re_θ	Reynolds number based on boundary layer momentum thickness
SPL	Sound Pressure Level (based on both 1/3 octaves or 19.52Hz bin widths)
St	Strouhal number
T	Period of vortex shedding frequency
t_o	Instant in time
U	Average streamwise velocity
U_∞	Freestream velocity
$U_i(\phi)$	Phase average velocity
U_{ref}	Reference velocity (30.5 m/s)

$\grave{u}$	Fluctuating velocity
$u_i(\phi, t)$	Phase fluctuating velocity
u_{rms}	Root mean square of streamwise velocity
u^+, y^+	Inner boundary layer wall coordinates
u_τ	Friction velocity
$\overline{uv}$	Reynolds stress (streamwise/normal component)
v_{rms}	Root mean square of normal velocity
$\grave{v}_{cal}$	Measured eigenvector of CSM
$\grave{v}_{theory}$	Theoretical eigenvector of CSM
$\grave{w}$	Weighting vector
X_b, Y_b	Beamforming grid points
x	Streamwise direction
$\grave{x}$	Far field observation point
$\grave{x}_b$	Beamforming "look" location
$\grave{x}_s$	Source location
$\grave{\boldsymbol{Y}}$	Values of $b(\grave{x}_b)$ in vector form
y	normal direction (perpendicular to both the chord and span of the model)
$\grave{y}$	Source location
y_f	Wake thickness parameter

Greek symbols

γ	Coherence function
∇_y	Del operator with respect to $\grave{y}$
δ	99% boundary layer thickness

δ^*	Boundary layer displacement thickness
θ	Boundary layer momentum thickness
κ, B	Constants for log law fit of boundary layer
Λ_z	Spanwise correlation length scale
λ_a	Acoustic wavelength
λ_{max}	Maximum eigenvalues of CSM
ρ_o	Density
ρ_a	Acoustic Density Fluctuations
$\rho_{u_i u_j}$	Two-point velocity correlation
$\sigma(\grave{x}_i, \grave{x}_j)$	Acoustic travel time from $\grave{x}_i$ to $\grave{x}_j$
τ_n	Time delay
$\Phi_i(y)$	i^{th} eigenmode of Karhunen-Loeve decomposition
Φ_p	Power spectral density of unsteady surface pressure
ϕ	Vortex shedding phase
$\vec{\omega}$	Vorticity
ω_z	Streamwise component of vorticity
ω	Circular frequency

CHAPTER 1

INTRODUCTION AND MOTIVATION

The flow of turbulence over the trailing edge of an airfoil can result in an unwanted source of radiated sound. This type of sound generation is often referred to as “self noise” since the source of the turbulence is most typically the turbulent boundary layers of the airfoil. A fundamental understanding of how the energy contained in turbulent motions is converted to sound is important to the design of quiet control surfaces with applications to marine vehicles, turbomachinery components, cooling fans, and propellers.

The present work was an experimental effort with three main objectives. The first objective was to create a well defined boundary value problem for the simultaneous experimental and numerical study of trailing edge noise. Specifically, experiments were conducted which documented the flow field boundary conditions in the vicinity of the trailing edge of a model airfoil placed in the test section of an Anechoic Wind Tunnel (AWT). These data were provided to the research group at Stanford University in order to help specify the numerical boundary conditions used in their study.

The second objective for this work was to investigate the turbulent flow physics in the near wake region. The flow field measurements provided the basic statistical features of the velocity field and unsteady surface pressure for use in validating the numerical

solutions conducted by Stanford University. In addition, spatially resolved velocity measurements were acquired in a separate aerodynamic wind tunnel. These measurements were acquired in order to study the dynamics of the near wake flow structure in detail.

The third and final objective of this research was to measure the radiated sound generated by the trailing edge. This required the use of two microphone arrays in order to obtain spatial maps of the radiated sound. The rejection of unwanted wind tunnel noise was of primary concern in generating a spectral representation of the sound radiated from the trailing edge. The resulting spectra are valid over a considerably larger frequency range than was obtained previously. In addition, a careful analysis of background noise and beamforming algorithms has provided a significant improvement in the measurement uncertainty.

The model used in this research was a thin flat strut with a 50.8mm thickness and a 0.91m chord. The leading edge was a 5:1 ellipse. Boundary layer trips were place 1/4 chord length downstream of the leading edge on both sides of the model. The Reynolds number ranged from 1.3×10^6 to 1.9×10^6 with a corresponding Mach number range of 0.06 to 0.09. At a streamwise location immediately upstream of the trailing edge region the boundary layers were fully turbulent with Re_θ=2900.

The trailing edge was an asymmetric blunt edge used previously by Blake (1986), Gershfeld et al. (1998), and Blake and Gershfeld (1989). Large Eddy Simulation (LES) results have been obtained for this geometry by Wang et. al (2006). A schematic representation of the geometry is shown in Figure 1. The edge is characterized by a rounded upper surface which intersects a flat bottom surface at a 45 degree angle. The

asymmetry results in a net camber and, hence, the upper and lower surfaces will be referred to as the suction and pressure sides, respectively.

Two separation points exist at the Reynolds number range used as shown in Figure 1. The boundary layer from upper surface separates prior to the trailing edge on the curved surface. The lower boundary layer separates at the sharp edge. The resulting flow field exhibits a number of phenomena that make it an interesting candidate for trailing edge noise research. Specifically, large scale vortex shedding will be shown to exist and linked to a notable tone in the radiated sound. Also, the boundary layer from the lower surface "scrapes" next to the sharp edge resulting in significant broadband sound level. The vortical fluid from the both the upper and lower surfaces recirculates in the near wake region which further contributes to the radiated sound.

The relationship between the near field turbulence and the radiated sound for non-compact lifting surfaces at low Mach number can be derived from a number of approaches. In general terms, the edge acts to "scatter" the near field pressure such that sound is produced efficiently even at relatively low Mach number. The result is a dipole-like sound field that is very sensitive to the nature of the turbulent motions in regions where the model surface curvature is large. Specifically, the magnitude and frequency of the radiated sound will be determined by both the intensity and the spatial correlation of

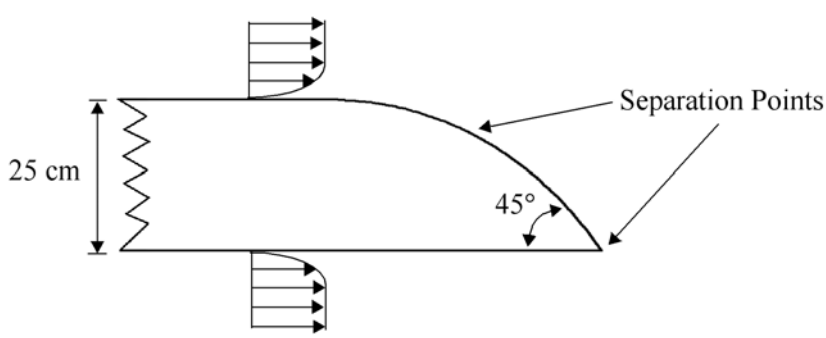

Figure 1.1: Schematic of trailing edge geometry.

the convected turbulence. For example, the amplitude of the tonal noise due to vortex shedding is typically quite large due to the large magnitude of the fluctuations, as well as the relatively long spanwise correlation length scale created by the vortex motions. In contrast, the smaller scale turbulent motions related to the boundary layer flow are both smaller in magnitude, and have a corresponding smaller spatial length scale. This results in a high frequency broadband acoustic signature that is typically more than 10dB less in magnitude than the vortex shedding noise.

The following chapters will outline basic aeroacoustic theory and detail the experimental results acquired for this trailing edge geometry.

CHAPTER 2

AEROACOUSTIC THEORY

This chapter will outline some of the analytical relationships between the flow of turbulence over a trailing edge and the far field sound this process generates. The turbulence $\underset{\sim}{u}$, unsteady surface pressure p'_s, and far field pressure p'_a produced by the flow over a trailing edge can be related to on another utilizing the continuity and Navier-Stokes equations. Figure 2.1 shows a sketch of these relationships. The generation of sound is directly related to the local turbulent velocity field through Lighthill's equation (see Section 2.1). The hydrodynamic surface pressures generated by these turbulent motions can be related through Poisson's equation (see Section 2.6). Similarly, the unsteady surface pressures can be directly related to the far field sound through Curle's

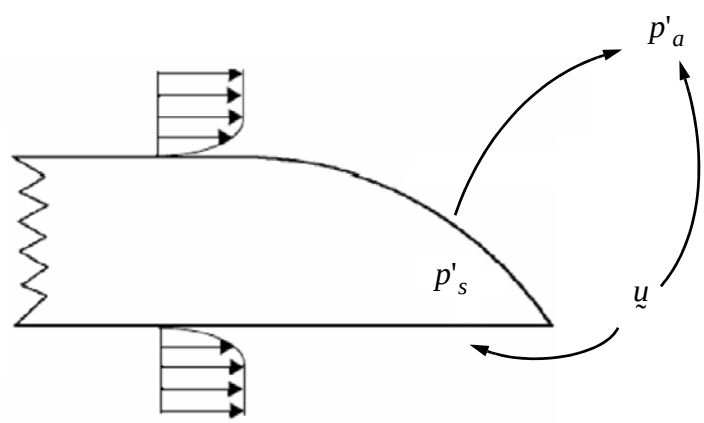

Figure 2.1: Illustration of relationships between unsteady surface pressure, turbulence and far field acoustics in trailing edge flows.

equation (see Section 2.2). This chapter will further describe aeroacoustic theory in further detail and discuss some previously used methods of predicting trailing edge noise from experimental results.

2.1 Lighthill's Equation

Lighthill (1952) derived the original theory for the generation of acoustics based on turbulence in subsonic flows. This theory was based on an analogy between nonlinear subsonic flow theory and linear acoustic theory. The conservation equations were combined to form Lighthill's equation

$$\left(\frac{1}{c_o^2}\frac{\partial}{\partial t^2}-\nabla^2\right)(p-p_o) = \frac{\partial T_{ij}}{\partial x_i \partial x_j} \quad , \tag{2.1}$$

where $p_a = p - p_o$ is the fluctuating pressure, c_o is the speed of sound, and the source term is Lighthill's stress tensor

$$T_{ij} = \rho u_i u_j + (p-c_o^2\rho)\delta_{ij} + \tau'_{ij} \ . \tag{2.2}$$

The term τ'_{ij} is the viscous part of the Stokes stress tensor and δ_{ij} is the Kronecker delta function. In regions of turbulence both hydrodynamic and acoustic pressure fluctuations are present. Outside of these regions (i.e. far field) only acoustic pressure fluctuations exist. For relatively high Reynolds numbers the viscous terms are considered to be small such that T_{ij} simplifies to the Reynolds stress $\rho u_i u_j$. It should be noted that for flows without turbulence this equation reduces to the homogeneous wave equation.

The Kirchhoff representation of (2.1) for high Reynolds number flows in the absence of solid surfaces can be achieved by integration and application of the free space Green's function such that

$$p_a(\grave{x}, t) = \frac{1}{4\pi}\iiint_V \frac{1}{r}\left[\frac{\partial^2(\rho u_i u_j)}{\partial y_i \partial y_j}\right]_\tau dV(\grave{y}), \tag{2.3}$$

where the expression inside the bracket is evaluated at the retarded time $\tau = t - r/c_o$. This solution is indicative of quadropole noise generated by turbulent flows. This result, however, is not valid for trailing edge flow fields as the presence of the airfoil will modify not only the source terms in the flow field, but also affect how the acoustic pressures propagate to the far field.

2.2 Curle's Equation

If one assumes a free space Green's function in the presence of an arbitrary body the direct integration of Lighthill's equation leads to Curle's formula

$$4\pi c_o^2 \rho_a(\grave{x}, t) = \frac{\partial^2}{\partial x_i \partial x_j}\iiint_V \frac{[T_{ij}]_\tau}{r} dV(\grave{y}) - \iint_S \frac{n_i}{r}\left[\frac{\partial(\rho u_i)}{\partial t}\right]_\tau dS(\grave{y})$$

$$+\frac{\partial}{\partial x_i}\iint_S \frac{n_i}{r}[\rho u_i u_j + \tau'_{ij} + p\delta_{ij}]_\tau dS(\grave{y}), \tag{2.4}$$

where n_i is the unite normal vector pointing outwards from the surface of the body (Curle, 1955). Thus, the sound generated by flow over a body is the sum of sources from quadropole sound generated to the local turbulence, monopole sources produced by an acceleration of the model surface, and a distribution of forces along the surface caused by a contribution of Reynolds stresses, viscous stresses, and surface pressures, which radiate as surface dipoles. For a rigid body at high Reynolds numbers the far field pressure can be represented by

$$p_a(\grave{x}, t) = \frac{\partial^2}{\partial x_i \partial x_j} \iiint_V \frac{[\rho u_i u_j]_\tau}{4\pi r} dV(\grave{y}) + \frac{\partial}{\partial x_i} \iint_S \frac{n_i}{4\pi r} [p]_\tau dS(\grave{y}) . \tag{2.5}$$

The volume integral of the turbulence in the source volume can be ignored for low Mach number flows leaving only the integral of the surface pressure. It should be noted that both the hydrodynamic and acoustic pressure will be included in this integral. Thus, it is important to include compressibility effects for acoustically non-compact geometries as the body surface extends into the far field (Howe, 1999).

2.3 Ffowcs Williams and Hawkings Equation

Ffowcs Williams and Hawkings (1969) derived a general formula from Lighthill's analogy for the far field pressure generated by the flow over an arbitrary surface. The surface is defined by $f = 0$, where $f > 0$ is outside of the surface and $\nabla f = n_i$ is the unit normal vector from the surface. The Ffowcs Williams-Hawkings (FW-H) equation

$$\frac{1}{c_o^2}\frac{\partial p}{\partial t} - \nabla^2 p = \frac{\partial^2}{\partial x_i \partial x_j}[T_{ij} H(f)] - \frac{\partial}{\partial x_i}[P_{ij} n_j \delta(f)] + \frac{\partial}{\partial t}[(\rho_o U_n)\delta(f)] \tag{2.6}$$

has source terms multiplied times the Heaviside function *H(f)*, which is zero inside the surface and unity outside the surface, and the Dirac delta function $\delta(f)$. The source terms include quadropole terms described by Lighthill's stress tensor T_{ij} in addition to both surface dipoles sources described by the compressive stress tensor P_{ij} and monopole sources from the motion of the surface described by U_n. For high Reynolds number flow over a rigid surface, terms including the surface normal velocity component and viscous stress terms can be ignored. Taking the Fourier transform of this equation results in the simplified equation

$$\nabla^2 p + k_o^2 p = \rho_o \frac{\partial^2}{\partial x_i x_j}[u_i u_j H(f)] . \tag{2.7}$$

The source term in this equation is unique in that it is often described as a quadropole source term. However, this term can cause dipole sound in the presence of a body through a scattering mechanism. Integrating equation (2.7) and applying Gauss's theorem results in an integral solution (Ffowcs Williams and Hall, 1970)

$$p(\grave{x}, \omega) = \frac{\rho_o}{4\pi}\iiint_V [u_i u_j] H(f) \frac{\partial^2}{\partial y_i \partial y_j} G(\grave{x}, \grave{y}, \omega) dV(\grave{y}) . \tag{2.8}$$

Thus, the far field acoustics can be regarded as the volume integral of the Reynolds stress convolved with the spatial derivatives of the Green's function. The Ffowcs Williams-Hawkings equation is commonly applied for trailing edge noise predictions based on numerical results where complete solutions to the source terms exists (Wang and Moin, 2000 and Oberai *et al.*, 2002).

The Green's function in (2.8) is the solution to the inhomogeneous wave equation such that

$$\nabla_y^2 G(\grave{x}, \grave{y}, \omega) + k_o^2 G(\grave{x}, \grave{y}, \omega) = -\delta(\grave{x}-\grave{y}) , \tag{2.9}$$

$$\frac{\partial G}{\partial n_i} = 0 \tag{2.10}$$

where $k_o = 2\pi f/c_o = 2\pi/\lambda$ is the acoustic wave number. This is a hard-wall Green's function whose normal derivative is forced to zero on the surface. The solution to (2.9) and (2.10) can be solved for analytically for relatively simple geometries. For more complex geometries the solution can be either measured directly or numerically

computed. It is also common to approximate the Green's function for trailing edge flows as that of a semi-infinite plane (see Section Section 2.5).

2.4 Vortex Sound

Powell (1964) derived a formulation of the acoustic pressure generated by a turbulent flow based on the sound produced by vorticity-velocity interactions. Howe (1975) presented an alternative form of this formula by linearizing the equation and combining acoustic pressure, density, and velocity fluctuations into a single acoustic variable, the total enthalpy:

$$B = p/\rho + \frac{1}{2}u^2 . \tag{2.11}$$

This resulted in Howe's formulation of the inhomogeneous wave equation

$$\nabla^2 B + k_o^2 B = -\nabla \cdot (\vec{\omega} \times \vec{u}) , \tag{2.12}$$

where k_o is the acoustic wavenumber. The source term for the turbulent generation of noise is the divergence of the vorticity-velocity cross product. This term describes the generation sound as vortex filaments are stretched. A solution to (2.12) for flow over a rigid body can be written as

$$B(\vec{x}, f) = -\iiint (\vec{\omega} \times \vec{u})\big|_{y,f} \cdot \nabla_y G(\vec{x}, \vec{y}, f) dV(\vec{y}) , \tag{2.13}$$

where $\vec{x}$ is the far field observation point, $\vec{y}$ is the source location, f is the frequency, ∇_y is the del operator with respect to $\vec{y}$, and $G(\vec{x}, \vec{y}, f)$ is the acoustic Green's function found by solving (2.9) and (2.10). Sound is generated by unsteady, spatially coherent values of

$\vec{\omega} \times \vec{u}$ in the locations where the magnitude of $\nabla_y G(\grave{x}, \grave{y}, f)$ is significant. Measurements of the vorticity and velocity field in the near wake of the trailing edge will be presented in chapter 3.

2.5 Half-Plane Green's Function

Perhaps the most ideal trailing edge problem is that of turbulent flow over a half-plane. The Green's function for this simplified geometry has an analytical solution as derived by MacDonald (1915). The nonzero components of the $\nabla_y G(\grave{x}, \grave{y}, f)$ vector for a half-plane geometry are shown in Figure 2.2 for an observation location of $\grave{x}k_o = \{0, 10, 0\}$ with respect to the edge of the plane. The magnitude of $\nabla_y G(\grave{x}, \grave{y}, f)$ is relatively large in the vicinity of the edge implying that the source terms in 2.7 and 2.12 (see Section 2.4) in this region will tend to radiate sound to the far field. In general, the components of $\nabla_y G((\grave{x}, \grave{y}, f))$ will be more significant in regions where the surface curvature of the model is relatively large (i.e. a sharp edge) because these features tend to

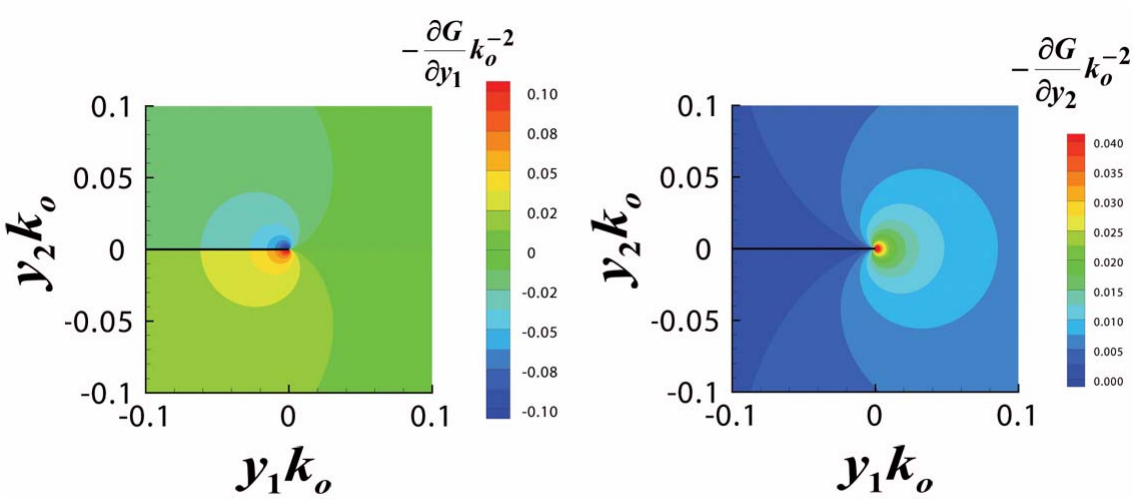

Figure 2.2: Nonzero components of $\nabla_y G(\vec{x}, \vec{y}, f)$ for an infinite half-plane. The observation location was $\vec{x}k_o = \{0, 10, 0\}$ with respect to the origin.

support the existence of uncancelled surface pressures, which will radiate to the far field as sound.

2.6 Prediction of Trailing Edge Noise

The following section will explore several methods used in the past that have attempted to predict trailing edge noise based on experimental measurements of turbulence and unsteady surface pressures.

2.6.1 Predicting Unsteady Surface Pressures from Flow Measurements

In general, the hydrodynamic surface pressure on a body can be represented as a function of the turbulent velocity field at any moment in time through the Poisson equation

$$\nabla^2 p = -\rho_o \frac{\partial u_i \partial u_j}{\partial x_j \partial x_i} = -\rho_o (S_{ij} S_{ij} - \Omega_{ij} \Omega_{ij}), \tag{2.14}$$

where the source term is the tensor product of the strain rate tensor with itself minus the tensor product of the rotation rate tensor with itself. The solution this equation is

$$p(\grave{x}, t) = \rho_o \iiint_V \left[\frac{\partial u_i \partial u_j}{\partial x_j \partial x_i} \right]_t G_p(\grave{x}, \grave{y}) dV(\grave{y}), \tag{2.15}$$

where the subscript t denotes the source terms at time t and $G_p(\grave{x}, \grave{y})$ is the Green's function of the Poisson equation. Turbulence correlated over a relatively large volume will tend to create a net pressure on the model surface. Small scale random turbulence fluctuations will average out over the volume integral.

While numerical methods have been able to compute the pressure on an airfoil, the literature currently lacks studies which predict the unsteady surface pressure spectra in trailing edge flows. Methods have, however, been developed for applications to turbulent boundary layer and backwards facing step flows (Lee *et al.*, 2005). In Lee *et al.* work, a time averaged formulation of equation (2.14) was utilized to relate the unsteady surface pressure to the turbulent source terms. A κ-ε turbulence model with the Reynold Averaged Navier Stokes (RANS) equations were used for the numerical solution to mean flow statistics. The unsteady nature of the flow was modeled as a wavenumber spectrum of the velocity in the wall normal direction. Anisotropy in the flow was accounted for by applying an anisotropic factor to the normal velocity fluctuations. The predictions made by Lee *et. al.* (2005) demonstrated good agreement with measured surface pressure spectra for both a turbulent boundary layer and a backward facing step. The results, however, were well outside the separated regions of the flow where anisotropic effects would be more significant.

2.6.2 Predicting Sound from Measured Surface Pressures

Known surface pressures can be related analytically to the radiated sound (2.5). This method has the advantage of only having to determine statistics of the surface pressure field in two dimensions rather than statistics of the flow field in three dimensions. The far field pressure was analytically derived by Howe (1978) as a function of the unsteady pressure near the trailing edge. Brooks and Hodsgson (1981) completed the first experimental study utilizing Howe's derivation for non-separating edge flows. This was followed by Gershfeld *et al.* (1988) who predicted the far field sound from measured surface pressure spectra. One of the geometries used in this study is identical the geometry

under investigation for this project (Figure 1.1). Spanwise correlation length scales $\Lambda_3(\omega)$ were utilized to model the spatial coherence of the surface pressures in this direction. The far field pressure was then estimated from the convolution of the measured surface pressure spectra near the apex of the trailing edge and an appropriate Green's function. Results from this study suggest that the sound produced in the tonal frequency band can be accurately predicted from pressure spectra on the attached pressure side of the model, while the sound in broadband frequency range was more closely predicted from the surface pressure spectra on the separated suction side of the airfoil.

The methods utilized in Gershfeld *et al.* (1988) and Brooks and Hodgson (1981) were later shown by Howe (1999) to be only valid at frequencies where the model was acoustically compact for this method to be valid. This is because the airfoil extends into the acoustic far field.

A more appropriate relationship can be formulated between the unsteady lift and the far field acoustics. Howe (1999) derived a formula relating the vorticity-velocity cross product to the force exerted on a fluid by the model (i.e. the unsteady lift)

$$F(\omega) \approx 2\rho_o \sqrt{\frac{i}{\pi k_o}} \left\{ \iiint_V \frac{\partial}{\partial y} \Phi^*(\grave{y}) \cdot (\vec{\omega} \times \grave{u}) dV(\grave{y}) \right\}, \tag{2.16}$$

where $\Phi^*(\grave{y})$ describes the incompressible potential flow around the edge of the airfoil. This unsteady lift term can be utilized to predict the far field acoustic spectra through an appropriate Green's function.

2.6.3 Predicting Sound from Flow Measurements

The prediction of trailing edge noise utilizing hot-wire anemometry has been attempted utilizing several methods. Roger *et. al.* (2006) predicted the tonal noise generated by a thick plate using a two-component hot-wire to measure the "upwash" velocity in the near wake. These turbulent statistics were used in a reversed Sears' problem model to predict the tonal noise generated by the plate. The results showed good agreement with the measure tonal noise. In addition, Devenport et al. (2001) measured two-point correlations functions in the near wake of a trailing edge using hot-wire anemometry and related these functions to the sound produced by the edge. Although these data provide valuable information regarding the spatial and temporal scales of a flow, they do not facilitate a detailed understanding of the mechanisms of sound production. Moreover, hot-wires are not well suited for blunt trailing edge flows where the near wake flow is separated and recirculating.

Similar work has been done using time resolve Particle Image Velocimetry (PIV) by Schroder et. al. (2004). The spatial/temporal two-point correlation functions were computed and related to the measured trailing edge noise. Though this data showed resolution of the larger scale turbulent motions inherent to vortex shedding, the spatial and temporal resolution of the data was insufficient to capture the smaller scale turbulent motions responsible for broadband noise.

CHAPTER 3

PARTICLE IMAGE VELOCIMETRY MEASURMENTS

This section describes the results of an experiment that was conducted using Particle Image Velocimetry (PIV). The purpose was to obtain detailed measurements in the near wake of the trailing edge. The experiment was conducted in a low-speed aerodynamic wind tunnel using the same model as the acoustic study. The motivation for this experiment was to provide a more complete understanding of the turbulent flow field than could be obtained by using single point statistics. Specifically, the PIV allows spatially resolved measurements of the in-plane velocity components. These data allowed the two point velocity correlation function to be obtained, as well as a decomposition of the flow field based on its vortex shedding phase. A sub-set of the information found in this Section can also be found in Shannon et. al (2006) and Shannon and Morris (2006).

A schematic of the airfoil model and test section is shown in Figure 3.1. The test section dimensions were 0.61m by 0.61m by 1.83m. The measurements were acquired using a two camera LaVision PIV system. The field of view from each of the cameras is outlined in Figure 3.1. Note the cameras were positioned with adjacent measurement areas and configured for measurement of two in-plane components of velocity. A dual 120mJ Nd: YAG pulse laser (wavelength: 523nm) and a cylindrical lens was used to produce a nominally 1mm thick light sheet. The laser head was positioned above the test section

such that the laser sheet illuminated particles at the mid-span of the airfoil. The surface of the model was coated with a florescent paint containing Rhodamine6G to reduce laser reflections from the surface. Images of the particles were acquired using a pair of CCD cameras with 1370 by 1040 pixel resolution. The timing of the laser pulses and the camera exposures was controlled by a computer containing a Programmable Timing Unit.

The application of PIV requires a homogeneous particle distribution in the measurement region. Particles were generated by a Topas ATM 230 aerosol generator, which produced droplets of olive oil ranging in diameter from 0.2 to 1.0μm. A particle diffuser was used to mix the particles before they were released into the tunnel inlet (see Figure 3.2). This diffuser consisted of a bank of five small fans that mixed the particles with the surrounding fluid. The turbulence induced by the mixing process was conditioned through a honeycomb section before the particle mixture was introduced at the tunnel inlet. The volume flow through the particle diffuser was adjusted such that the outlet

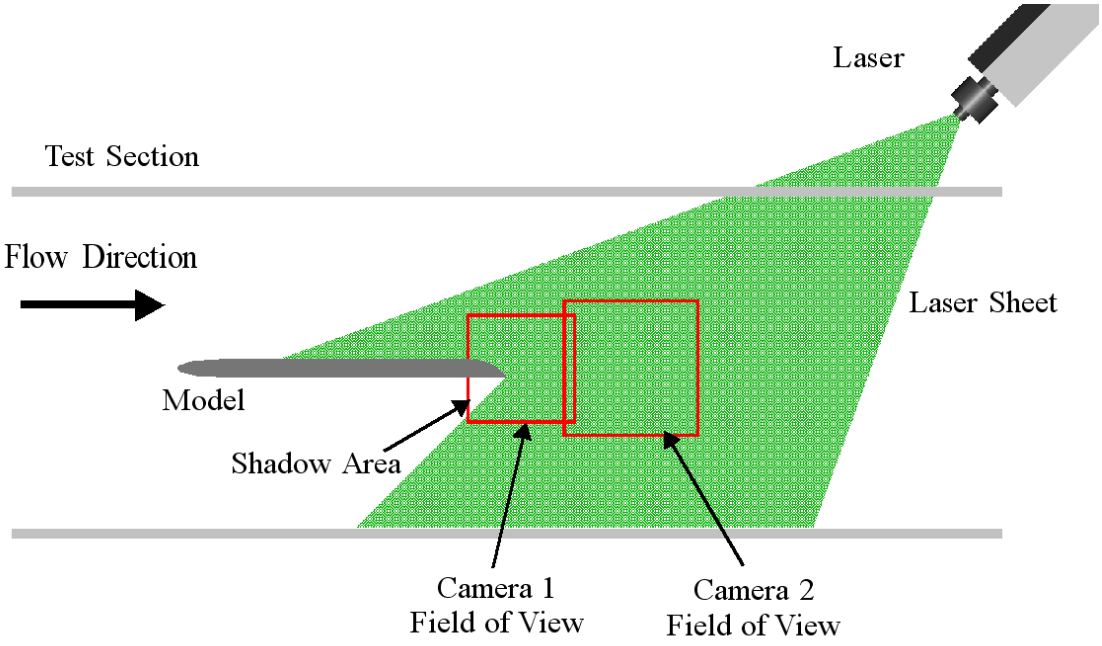

Figure 3.1: Schematic of PIV experimental setup.

velocity of the mixer was equal to the inlet velocity of the tunnel. This process created a homogeneous particle distribution in the measurement region. The particle diffuser also reduced the number of particles located between the measurement plane and the cameras minimizing the optical diffusion effects caused by particles outside of the camera focus plane.

Velocity vectors were computed from the particle images using DaVis software by LaVision, which utilizes an iterative correlation technique to compute the velocity from the particle movement observed between camera exposures. An adaptive multipass algorithm was employed with a final interrogation window size of 16 by 16 pixels with an overlap of 50%. The velocity data from each camera were combined to produce a vector resolution of 0.83mm over an area of approximately 270mm by 107mm. A total of 1000 statistically independent samples were acquired at approximately 3 Hz.

Uncertainty in PIV measurements is dependent on the uniformity of seeding particles, the camera focus, and the illumination of the particles in each interrogation

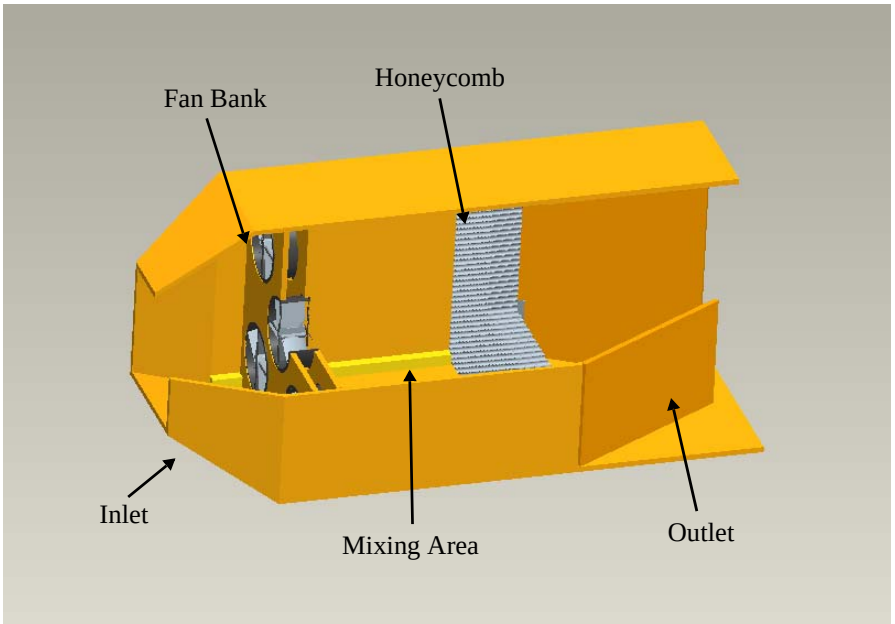

Figure 3.2: Schematic of particle diffuser.

window. As such, the uncertainty can vary over the measurement region and between PIV realizations. An estimate of the uncertainty for this study can be made assuming a subpixel accuracy of 0.1 pixels. This corresponds to a particle displacement accuracy of 0.0104mm, implying that the velocity measurements have an accuracy of approximately 1.4% when compared to the free stream velocity. This estimate agrees with the measured root mean square of the velocity in regions where the flow was nominally steady.

The vector maps obtained from each PIV realization contained regions of missing data where the absence of seeding particles in an interrogation window made computing the flow velocity impossible. This was more common in regions of the flow where velocity fluctuations and gradients were relatively high. These occurrences, often referred to as gappy data, were limited to an average of 2.4% of the vectors in each realization. Velocity statistics were computed by evaluating the appropriate integrals using only valid vectors.

3.1 Flow Visualization

Figure 3.3 shows examples of streakline flow visualization with the flow direction from left to right. The outline of the trailing edge can be observed by the reflection of the laser sheet. A mirror was used to illuminate the shadow region beneath the model. The regions of sharp contrast below the model are a result of the optical setup and not a result of the fluid behavior.

The diffused smoke attached to the upper and lower surfaces of the model is indicative of the turbulent boundary layers. The upper boundary layer separates gradually in the adverse pressure gradient created by the beveled edge, while the lower boundary layer separates at the sharp edge. The separated region directly behind the trailing edge is

seen as an area of diffuse smoke. The shedding of boundary layer vorticity into the near wake creates a von Karman vortex street. This flow pattern is common to blunt trailing edge wake instabilities.

3.2 Instantaneous Results

It is instructive to examine the instantaneous flow field before viewing statistical results. An example of a single PIV realization is shown in Figure 3.4. Contours of streamwise velocity with streamlines are included as is a contour map of the spanwise vorticity (ω_z). The trailing edge shape is outlined on the left of the figure with the flow direction from left to right. A shadow region, where data were unavailable, is located just

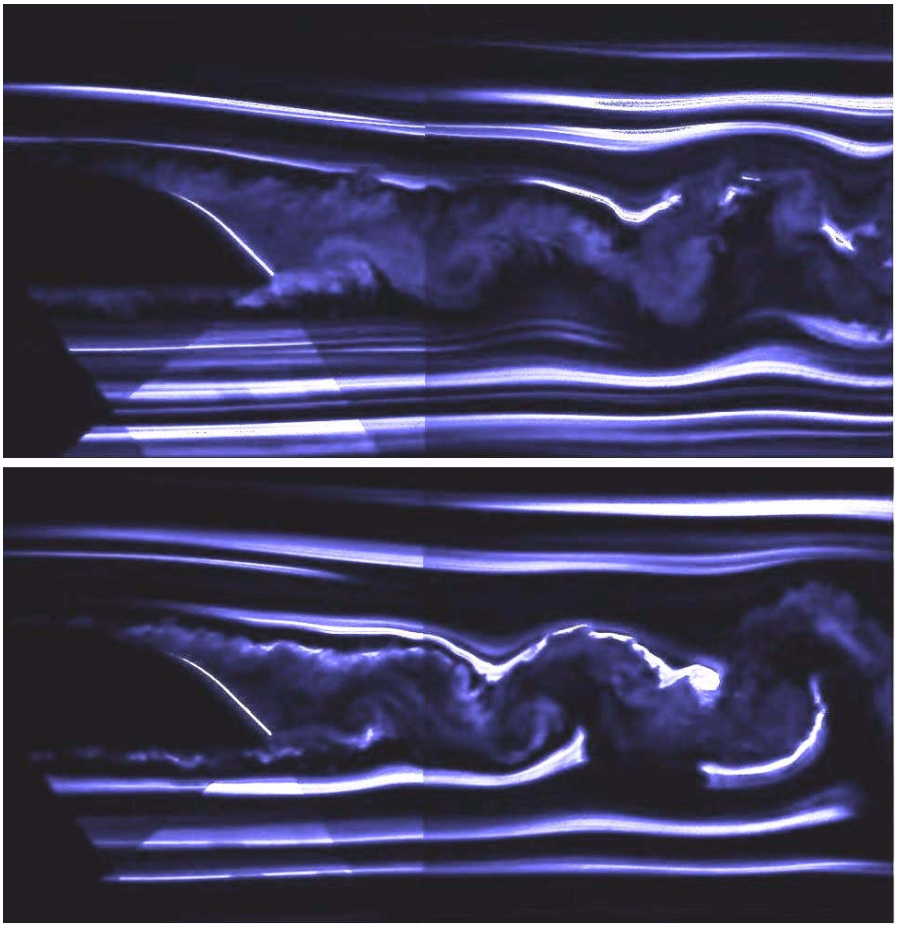

Figure 3.3: Two realizations of streakline flow visualization

below the trailing edge. The spanwise vorticity was computed utilizing a fourth order spatial discretization scheme. The data were normalized using the free stream velocity and a wake thickness parameter $y_f \cong 2.54$ cm, determined by the minimum distance between the upper and lower regions of shear in the near wake. This parameter was found by measuring the minimum normal distance between the local maxima of root mean square (rms) of the streamwise velocity (see section 3.3 below).

The low momentum fluid contained in the separated region was bound by high momentum fluid on either side, generating two regions of shear in the near wake. The interaction of the separated vorticity in these shear layers resulted in a large scale wake instability. This is evident in the von Karman vortex street observed downstream of the

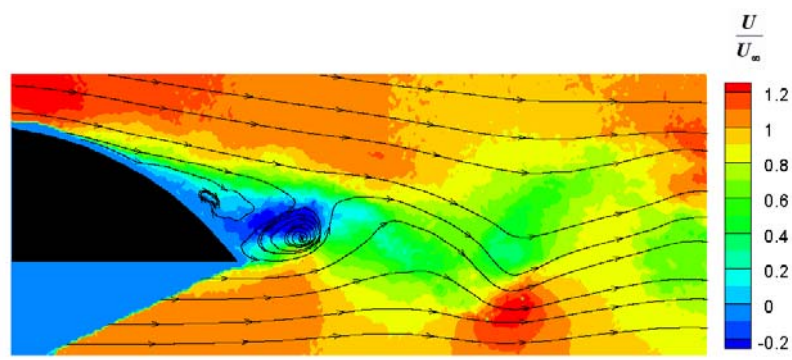

a) Streamwise velocity contours with streamlines

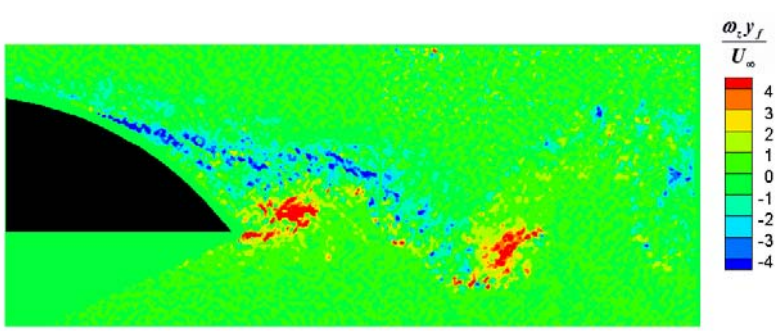

b) Spanwise vorticity contours

Figure 3.4: Instantaneous PIV realization.

model in Figure 3.4. The unsteady lift that results from this wake instability is responsible for the tonal noise generated by the trailing edge.

An interesting aspect of the vortex shedding for this trailing edge is that the asymmetry in the model caused a noticeable irregularity in the von Karman vortex street. The lower boundary layer remained relatively undisturbed before separating suddenly at the sharp edge. The vorticity shed into the wake from the lower edge formed relatively large concentrations of positive circulation which “rolled up” near the lower, sharp edge of the model and accelerated into the wake at periodic intervals. The realization shown in Figure 3.4 shows two relatively compact structures at approximately 1/3 and 2 model thickness downstream of the edge. Note that the magnitude of the vorticity and the spatial extent of these two motions are similar, suggesting that these motions remain relatively unchanged as they convect downstream into the wake.

In contrast to the motions created from the lower edge, the upper boundary layer is subjected to an adverse pressure gradient which causes the (negative) vorticity to diffuse prior to separation. Subsequently, vorticity convected from the upper surface did not roll up into compact motions, but formed a more diffuse region of shear that included groupings of smaller scale motions.

3.3 Time Averaged Results

Contours of the time averaged streamwise velocity and spanwise vorticity are shown in Figure 3.5. The flow over the upper side of the model had a larger velocity magnitude due to a small amount of lift generated by the asymmetry of the trailing edge. There are two separation streamlines originating from the upper and lower separation points shown in Figure 1.1. The time averaged streamlines show two recirculation regions

with closed streamlines located just downstream of the sharp edge and over the separated region. A stagnation streamline was located between these two regions of recirculation.

The time averaged vorticity field shows the convection of separated vorticity from the upper and lower boundary layers into the near wake region. Concentrations of time averaged positive vorticity were located inside the lower recirculation region near the sharp edge. Conversely, concentrations of time averaged negative vorticity were located over the upper recirculation region along the stagnation streamline originating from the upper separation point.

It is of particular interest to observe the fluctuating parts of the velocity field as these are the components that are responsible for the generation of sound by the trailing edge. Figure 3.6 shows the root mean square (rms) quantities of the streamwise velocity and normal velocity components. The u_{rms} contours show the existence of two local regions of relatively high streamwise turbulence. The minimum distance between the local

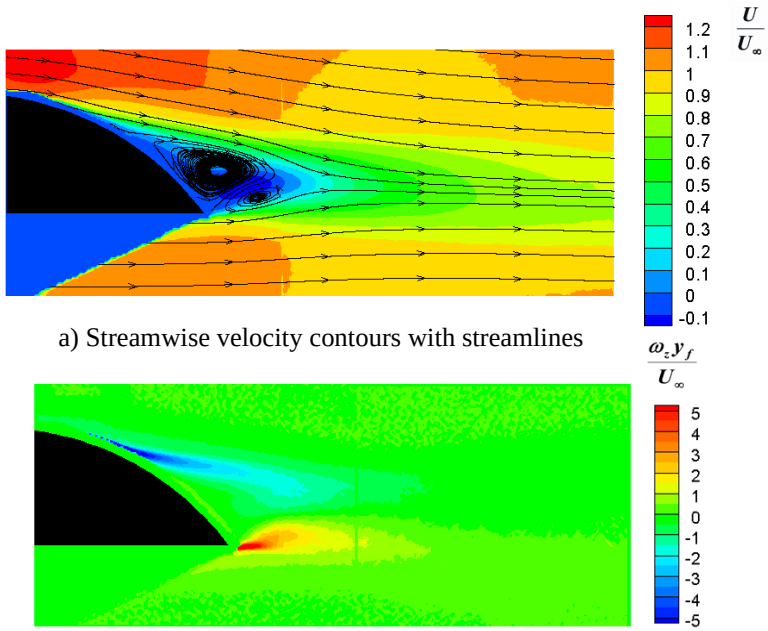

a) Streamwise velocity contours with streamlines

b) Spanwise vorticity contours

Figure 3.5: Time averaged PIV results.

maxima in these regions defines the wake thickness parameter y_f discussed in section 4.2.3.

The majority of the normal velocity fluctuations (v_{rms}) were observed to be concentrated toward the sharp lower edge of the model. The compact vortical structures created at this edge generated relatively large fluctuations in the vertical velocity (up to 30% of the freestream) as the high momentum fluid from the lower edge mixed with the low momentum fluid in the separated region. The normal velocity fluctuations in the upper shear region were smaller in comparison.

The $\overline{uv}$ component of the Reynolds stress tensor is shown in Figure 3.7. Two regions of shear stress were observed in the near wake. A negative shear stress was observed in the upper shear layer, while a positive shear stress was present in the lower

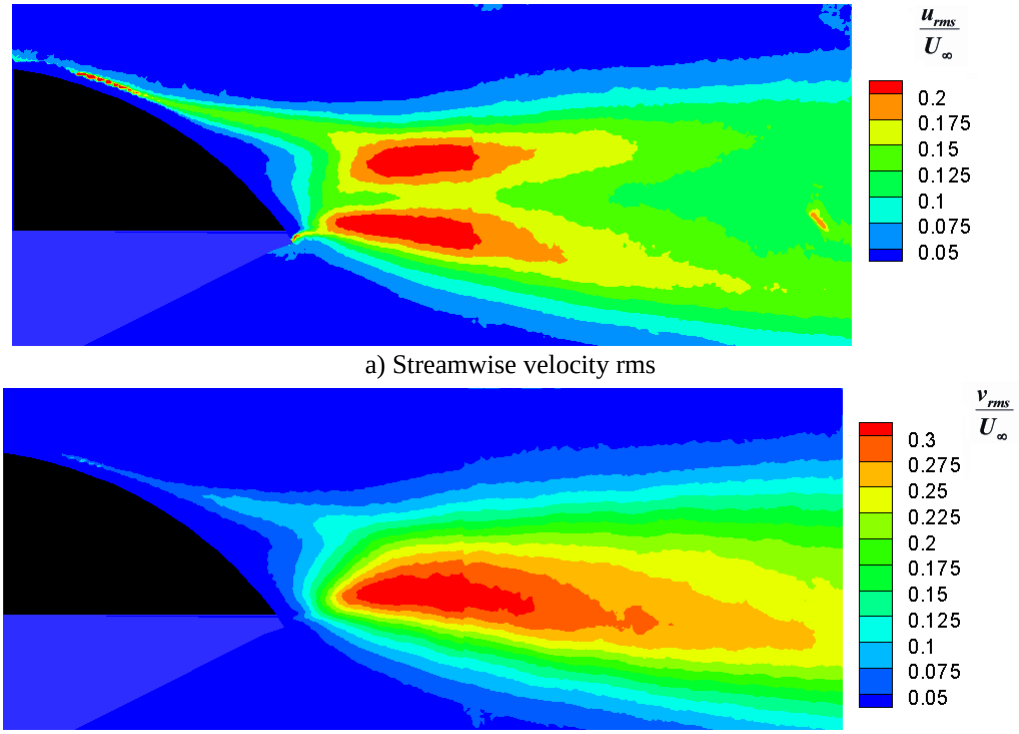

a) Streamwise velocity rms

b) Normal velocity rms

Figure 3.6: Root mean square velocities.

shear layer. The wake asymmetry was again apparent as the maximum magnitudes of positive Reynolds stress were approximately 50% greater than the negative values.

It is of interest to study the relative spatial coherence of the turbulent motions in the near wake because spatial coherence in the vicinity of the sharp edge will tend contribute to the integral in equations (2.8) and (2.13). It should be noted that following is presented to give an indication of the average turbulent length scales associated with the flow and not as a direct interpretation of the Fourier transformed variables in (2.8) and (2.13). The two-point velocity correlation coefficient, as defined by

$$\rho_{u_i u_j}(\vec{x}, \vec{y}) = \frac{\overline{u'_i(\grave{x})u'_j(\grave{y})}}{\sqrt{\overline{u'_i(\grave{x})^2}}\sqrt{\overline{u'_j(\grave{y})^2}}}, \tag{3.1}$$

can give an indication of the spatial coherence of the turbulence at the reverence location $\grave{x}$.The area enclosed by contour lines of constant $\rho_{u_i u_j}(\grave{x}, \grave{y})$ will give an indication of the coherence of the turbulent motions at $\grave{x}$. In addition, a turbulent integral length scale can be defined as

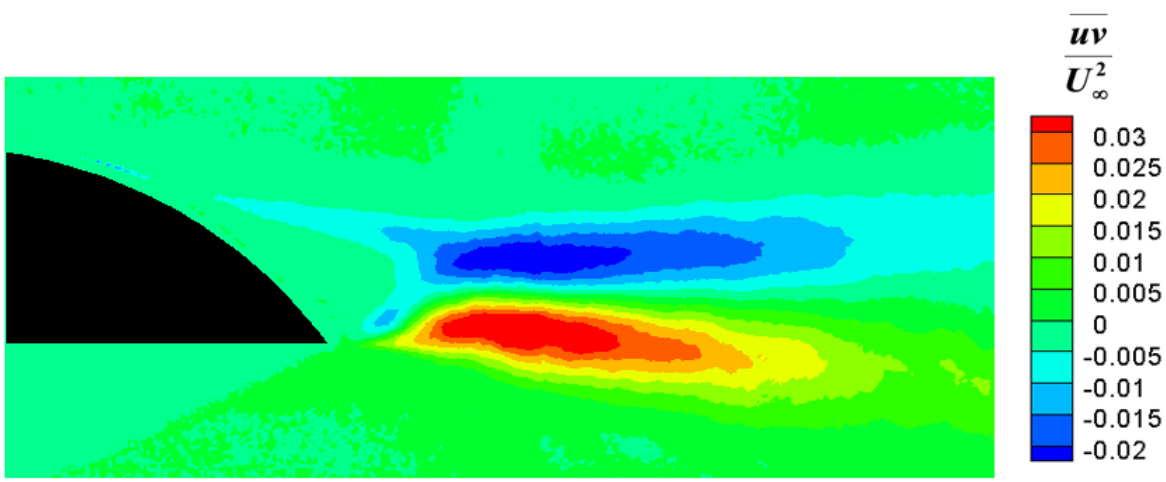

Figure 3.7: Time averaged Reynolds stress.

$$\Lambda_{u_i u_j}{}^2(\vec{x}) = \iint \rho_{u_i u_j}(\vec{x}, \vec{y}) d\vec{y}. \tag{3.2}$$

In order to examine these length scales, the reference location was chosen to be at a position $\grave{x}/y_f = \{0.5, 0\}$ with respect to the sharp edge. This location was chosen because it is close to the sharp edge where the $\nabla_y G(\grave{x}, \grave{y}, f)$ term will be relatively significant.

The time averaged two-point correlation coefficient for the streamwise and normal velocity components are shown is Figure 3.8. The location $\grave{x}$ is denoted by an open circle. There were significant correlation magnitudes between the turbulent fluctuations at $\grave{x}$ and in the downstream wake. These time averaged correlation values are observed to be mainly representative of the velocity fluctuations related to the large scale vortex

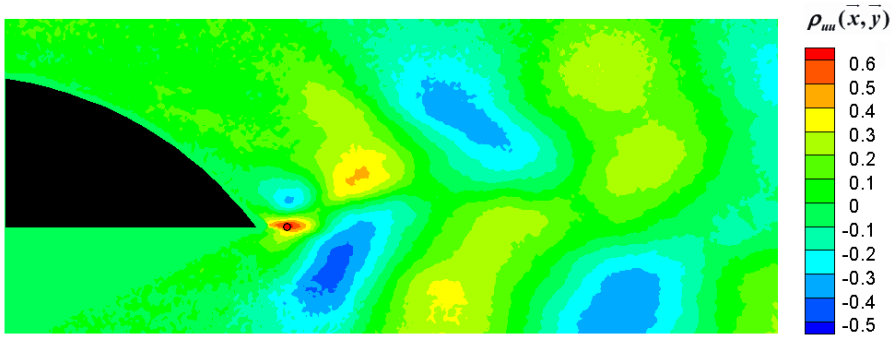

a) Streamwise velocity component correlation

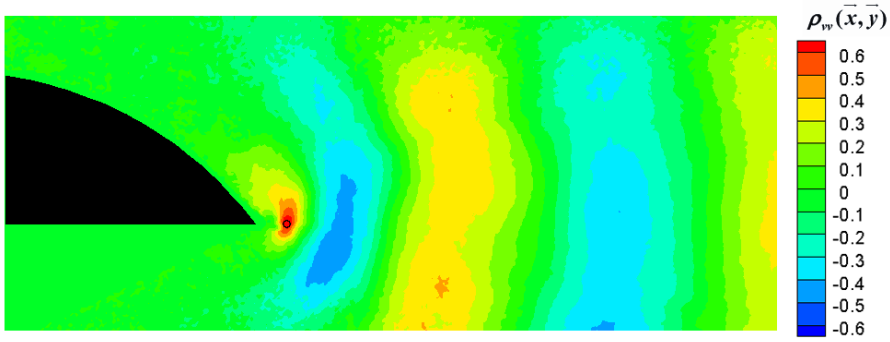

b) Normal velocity component correlation coefficient

Figure 3.8: Two-point correlation coefficients for $\vec{x}/y_f = \{0.5, 0\}$ with respect to the trailing edge.

shedding. Specifically, spatially alternating regions of positive and negative correlation magnitudes are indicative of the spatially (and temporally) periodic motions. As such, these correlations can be considered to be related to the motions which generate tonal sound. Note that because of the relative magnitudes of the velocity fluctuations related to shedding, it is not possible to make observations regarding the small scale motions related to broadband sound.

3.4 Phase Averaged Results

A phase averaged decomposition is now introduced in order to separate the velocity fluctuations related to the wake instability from those related to smaller scale velocity fluctuations. This will allow for the independent study of the turbulent motions occurring at the shedding frequency and those occurring at other frequencies.

A phase averaged decomposition can be formally written in terms of the vortex shedding phase ϕ,

$$u_i(t) = U_i(\phi) + u_i'(\phi, t), \tag{3.3}$$

where $U_i(\phi)$ represents a phase mean and $u_i'(\phi, t)$ represents the fluctuations about the phase mean. This decomposition explicitly assumes that a period T exists for the vortex shedding process and that each PIV realization is representative of a particular phase in that process. This is similar to a Reynolds decomposition except that the mean term is a function of the vortex shedding phase and the fluctuations are taken about that mean rather than a time average. The implication of this decomposition is that the phase mean represents the turbulent motions occurring at the vortex shedding frequency with all other

turbulent scales averaged out. The velocity fluctuations occurring at other frequencies are included in the phase fluctuating component $u_i'(\phi, t)$.

The motivation for phase averaging the velocity measurements and the interpretation of the results in terms of the acoustic production can be given as follows. The right hand side of (2.13) represents the temporal Fourier transform of $\nabla \cdot (\vec{\omega} \times \vec{u})$. Since the acoustic production is governed by a linear equation, the different frequencies contained in the flow field can be considered independently, regardless of the fact that the equations that lead to the unsteady flow (i.e., the Navier-Stokes equations) are distinctly nonlinear. Thus, the fluid motions which create broadband sound can be considered by high pass filtering the velocity and vorticity field above the vortex shedding frequency. Since the present PIV dataset in not temporally resolved, subtracting $U_i(\phi)$ from the instantaneous velocity provides an effective high pass filter to the data.

3.4.1 Algorithm

The application of equation (3.3) requires that ϕ be determined for each PIV vector map. A method for implementing this was developed using a unique application of the Karhunen-Loeve decomposition. The present application of this decomposition is distinct from Proper Orthogonal Decomposition (POD) Holmes et al, (1996), although the principal is essentially the same. The following method was developed for the sole purpose of determining the phase of each PIV realization and not as an analysis tool for low dimensional modeling. The streamwise component of velocity for a particular PIV realization acquired at time (t_o) can be represented as:

$$u(x,y)\big|_{t_o} = \sum_{i=1}^{N} a_i(x)\big|_{t_o} \cdot \Phi_i(y)\,. \tag{3.4}$$

The eigenmodes $\Phi_i(y)$ are the discrete eigenvectors determined from the cross-correlation matrix evaluated at each streamwise measurement location. There exists N eigenvectors and eigenvalues for each streamwise measurement location, where N is the number of measurement points in the y direction (N = 130). The coefficients $a_i(x)\big|_{t_o}$ represent the amplitude of each eigenmode for the PIV realization obtained at time t_o and were found by taking the projection of the eigenmodes onto the instantaneous velocity field.

The first four eigenmodes in the downstream wake are shown in Figure 3.9. The first eigenmode is a representation the time averaged streamwise velocity. With each increase in mode number the eigenvalues become smaller and the spatial fluctuations of the modes become smaller scale. The motivation for the Karhunen-Loeve decomposition

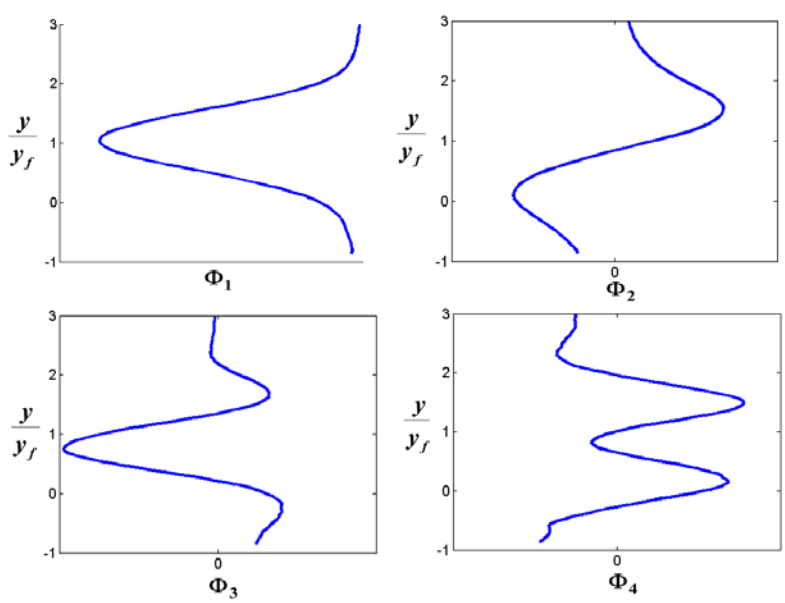

Figure 3.9: The streamwise average of the first four eigenmodes in the downstream wake.

was to find an eigenmode that was associated to the large scale wake instability. It was found for this trailing edge flow that the second eigenvector $\Phi_2(y)$ was related to the large scale vortical structures generated by the wake instability. Figure 3.10 shows this eigenmode profile along with the circumferential velocity of a Taylor vortex (Panton, 1996). The value of the second coefficient represents the magnitude of the second eigenmode a function of *x*. It was found that this profile produced a waveform whose phase value was dependent on the streamwise distribution of the large scale wake instability observed in each PIV realizations The second coefficient $a_2(x)|_{t_o}$ for the same instantaneous image illustrated in Figure 3.4 is shown in Figure 3.11.

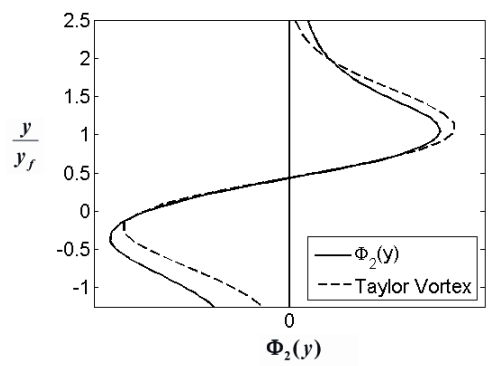

Figure 3.10: Second eigenmode of Karhunen-Loeve decomposition compared to a Taylor vortex profile.

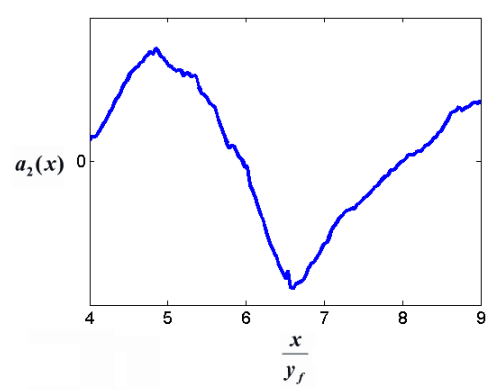

Figure 3.11: Second coefficient for KL decomposition for the vector map illustrated in Figure 3.4.

The shedding phase of each PIV realization was determined from an analysis of the phase of $a_2(x)|_{t_o}$. Specifically, the $a_2(x)|_{t_o}$ waveform was spatially filtered utilizing a low order Fourier fit to reduce the noise produced by the small scale turbulence in each vector map. The phase was determined from the streamwise position of the local maxima of the filtered profile. The $\phi = 0$ condition was chosen at an arbitrary location in the shedding process and the images were separated into 10 phase bins. A histogram of the distribution of the data set over the phase bins is shown in Figure 3.12. The phase distribution of PIV images appears to be relatively uniform over the shedding cycle, as would be expected for data acquired randomly with respect to the vortex shedding process.

3.4.2 Results

Figure 3.13 shows contours of the phase averaged streamwise velocity field with streamlines. The phase averaged velocity fields are similar to the instantaneous measurements shown in Figure 3.4 with the smaller scale velocity fluctuations removed.

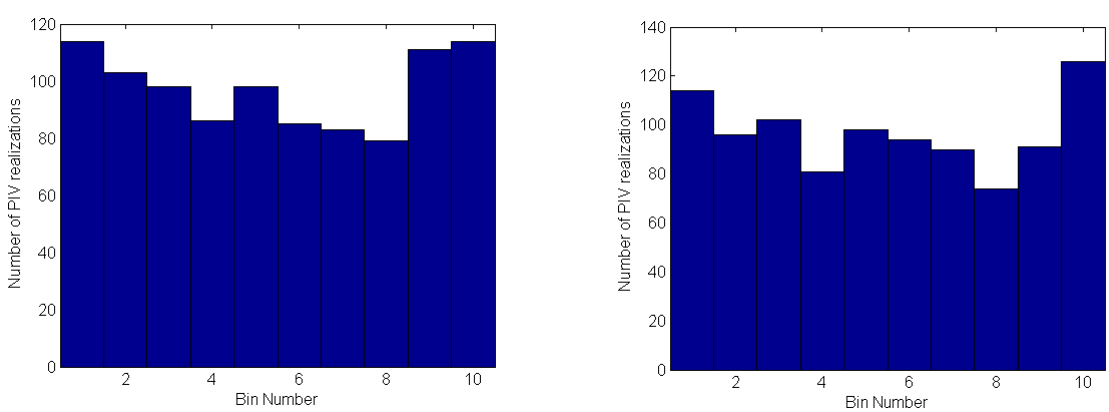

a) $Re_c = 1.2x10^6$ b) $Re_c = 1.9x10^6$

Figure 3.12: Histogram of 1000 PIV realizations sorted into 10 phase bins.

Two regions with closed circular streamlines are observed to grow, separate, and convect downstream as the vortex shedding phase progresses.

The vorticity field as a function of the vortex shedding phase is shown in Figure 3.14. As the phase progresses the positive vorticity from the lower boundary layer separates from the model surface, “rolls up” into the low momentum region behind the trailing edge, and convects downstream. These large scale structures remained coherent as they accelerated into the downstream wake. The phase averaged negative vorticity originating from the upper boundary layer is more diffuse in nature and does not remain coherent further downstream of separation. The compact regions of positive vorticity appear to “impinge” on the negative vorticity as it convects into the near wake. Further downstream, the negative (phase averaged) vorticity is found to be distributed evenly between the vortical structures generated at the sharp edge.

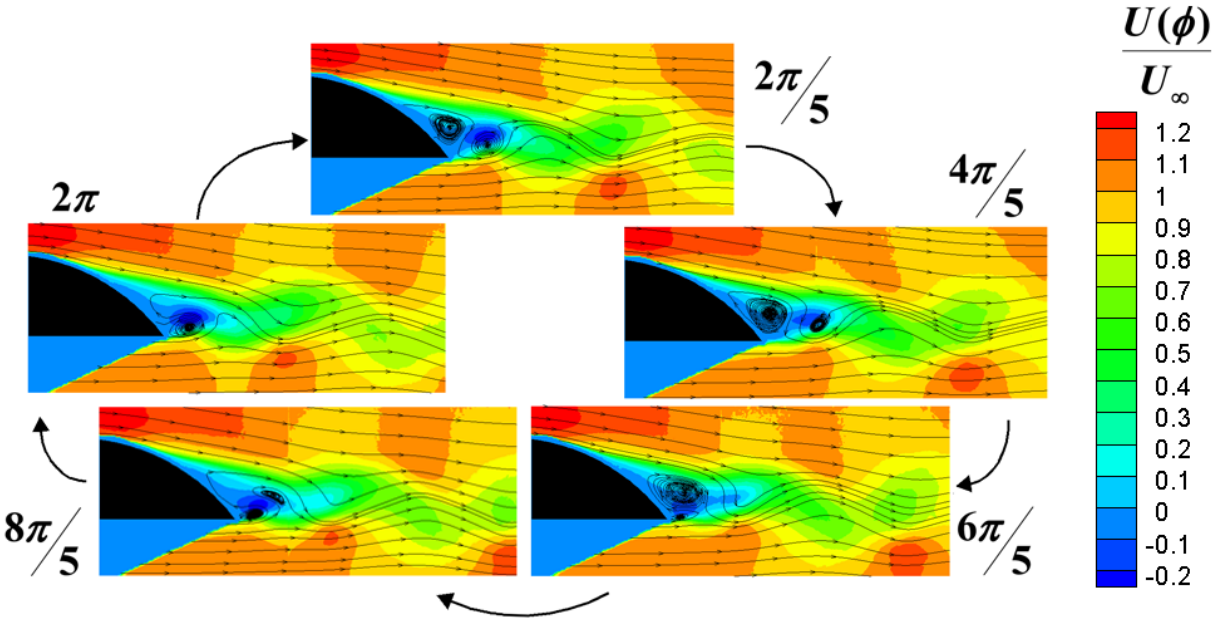

Figure 3.13: Contours of phase averaged streamwise velocity with streamlines.

Figures 3.15 and 3.16 show the root mean square of the phase fluctuating components of streamwise and vertical velocity components, respectively. These quantities can be considered to be related to the broadband noise produced by the trailing edge flow field because the components of the fluctuating velocity occurring at the tonal frequency have been removed. The largest values of the phase fluctuating component of the normal velocity component are located at the lower edge of the wake near the sharp edge. Note that even with the large scale motions removed, the $v_{rms}(\phi)$ values peak at approximately 30% of the freestream velocity near the sharp edge.

Figure 3.17 shows the phase averaged $\overline{uv}(\phi)$ component of the Reynolds stress tensor. This contour map shows the shear stress caused by the small scale turbulent motions in the near wake. Two regions of turbulent shear stress are observed to be concentrated about the location of the positive vorticity observed in Figure14. The magnitudes of shear stress generated by the phase fluctuating velocity were significant

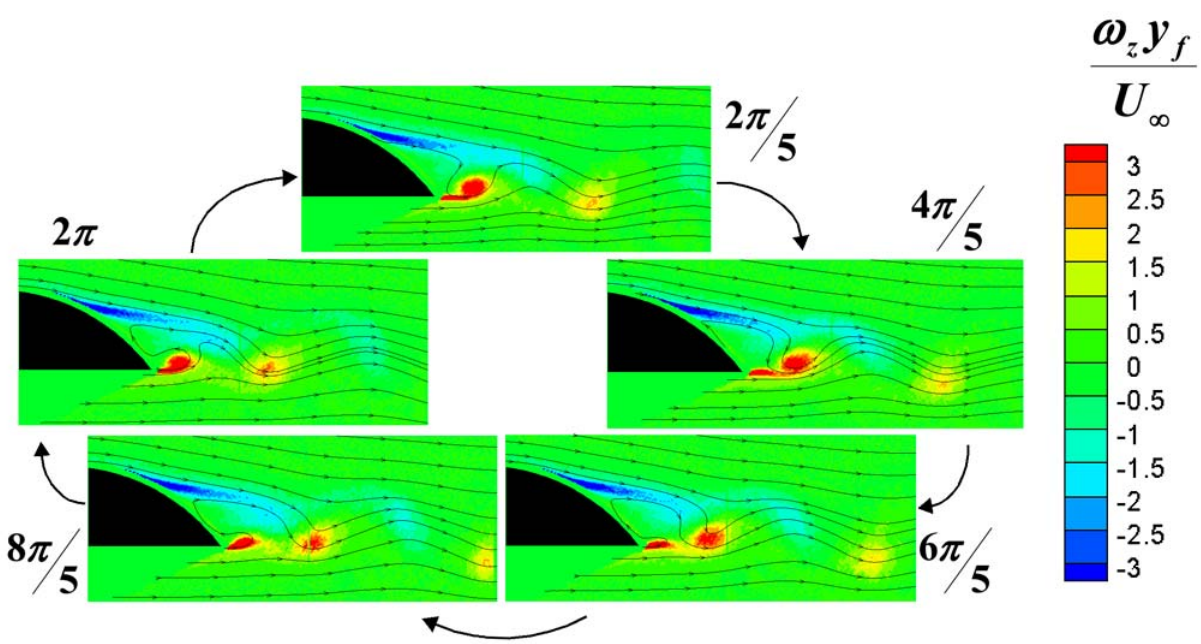

Figure 3.14: Contours phase averaged vorticity with streamlines.

with respect to the time averaged values, suggesting that the majority of the turbulent momentum transport was related to the small scale motions in the wake.

The turbulent motions represented in Figures 3.15, 3.16, and 3.17 are by definition distinct from the vortex shedding motions. It is clear, however, that the characteristics of

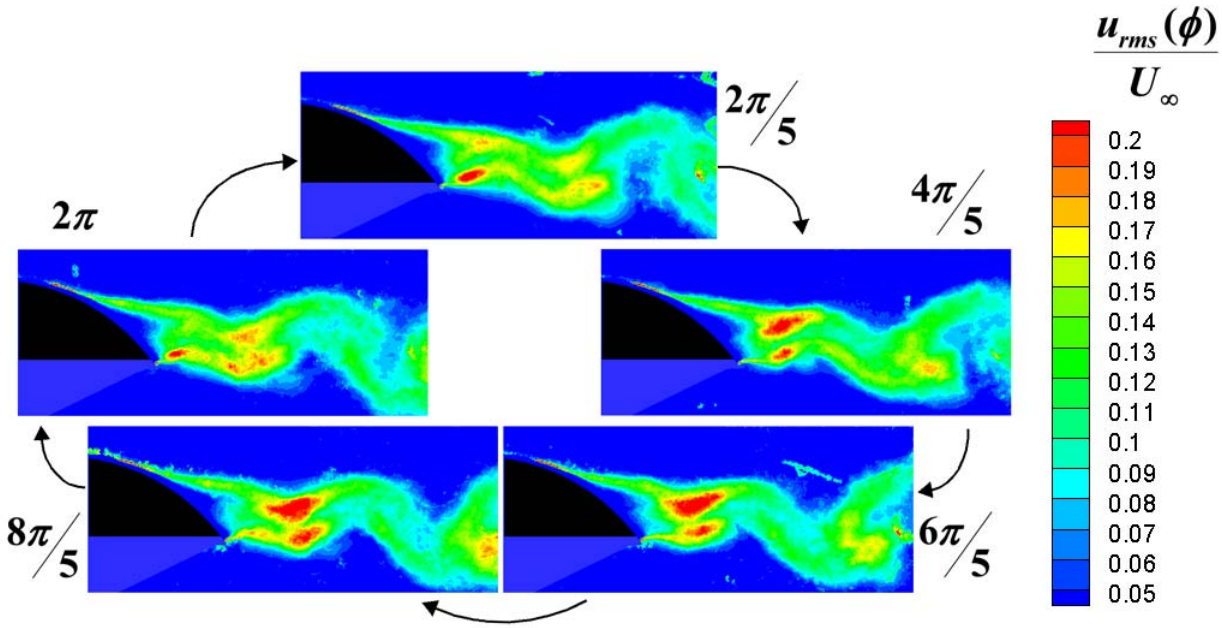

Figure 3.15: Root mean square of phase fluctuating streamwise velocity.

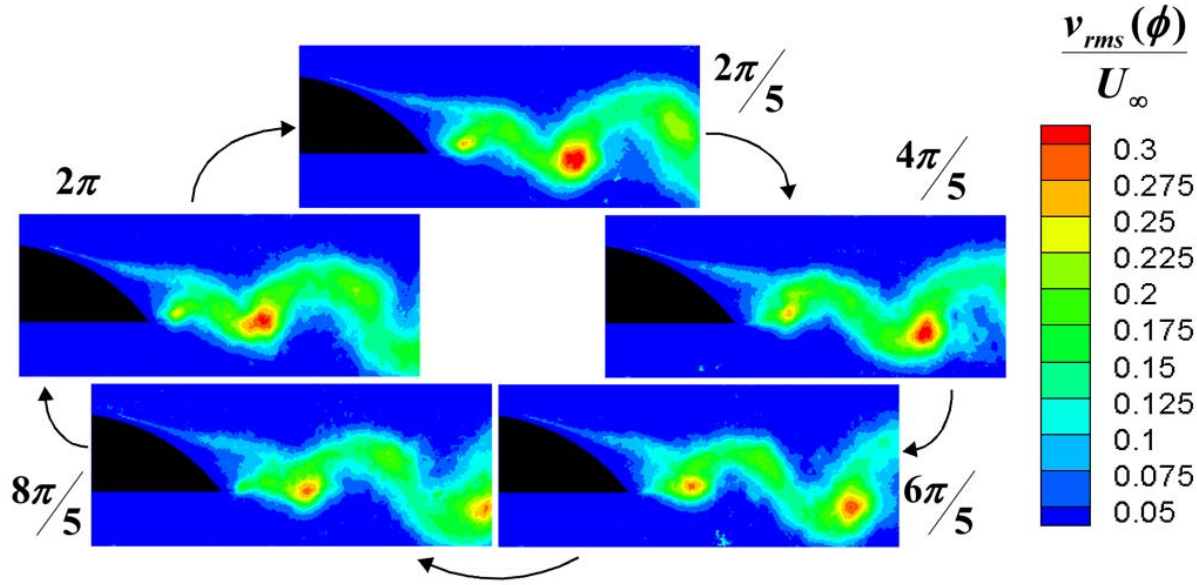

Figure 3.16: Root mean square of phase fluctuating normal velocity.

the small scale fluctuations are a relatively strong function of the shedding phase. Specifically, the magnitudes of $u_{rms}(\phi)$, $v_{rms}(\phi)$, and $\overline{uv}(\phi)$ were found to vary by a factor of two or more during the shedding cycle in the vicinity of the sharp edge. It was also observed that the values of $u_{rms}(\phi)$ and $v_{rms}(\phi)$ associated with the roll up of the lower boundary layer were up to four times larger than those associated with the turbulence originating from the upper boundary layer. In addition, the upper boundary layer turbulence was located farther from the sharp edge suggesting that the turbulence originating from the lower side boundary layer will be primarily responsible for the production of broadband sound.

A phase averaged two-point correlation can be defined by independently applying equation (3.1) to each phase bin. The correlation coefficient will give an indication of the turbulent length scales important to broadband noise production as a function of the shedding phase. Figures 3.18 and 3.19 show the phase averaged streamwise and normal

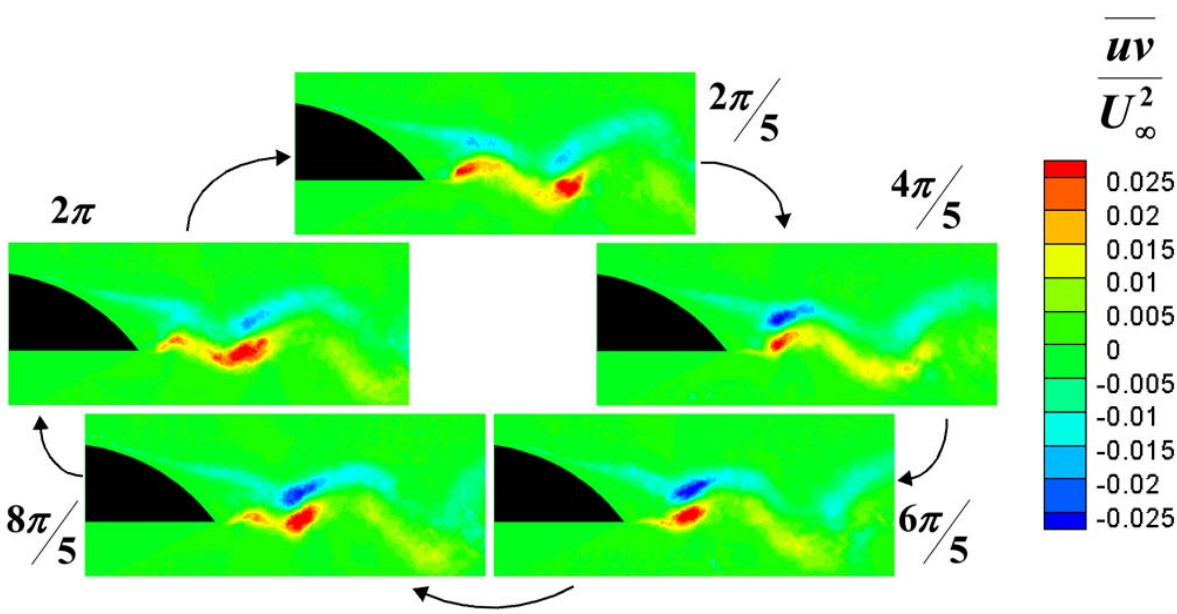

Figure 3.17: Contours of phase averaged Reynolds stress.

velocity component two-point correlation coefficients, respectively. Only data in the vicinity of the edge are shown because the length scales associated with the phase fluctuating turbulent motions are relatively small. The reference position was again defined as $\vec{x}/y_f = \{0.5, 0\}$ with respect to the sharp edge. The area enclosed by contours of constant $\rho_{u_i u_j}$ appear to grow and decay as the phase progresses. Specifically, the correlation areas are significantly larger for values of ϕ between 0 and $2\pi/5$, which suggests that the length scales associated with broadband sound production are dependent on the phase of the wake instability.

The two-point velocity correlation $\rho_{uu}(\phi)$ was integrated according to equation (3.2) to generate a length scale associated with the streamwise phase fluctuating velocity $\Lambda_{uu}(\phi)$. This quantity is shown in Figure 3.20 along with the values of $\omega_z(\phi)$ and

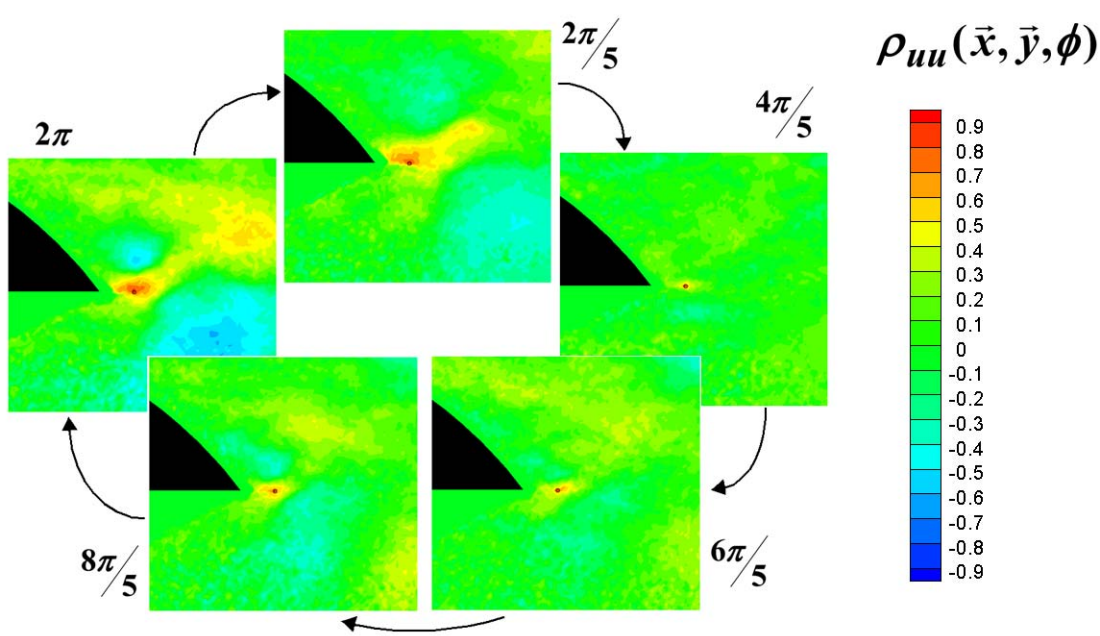

Figure 3.18: Two-point correlation coefficient for

$u_{rms}(\phi)$ to provide a reference for the shedding process at the reference point $\vec{x}/y_f = \{0.5, 0\}$. Two shedding cycles are plotted. The magnitudes of $\Lambda_{uu}(\phi)$, $\omega_z(\phi)$, and $u_{rms}(\phi)$ were all observed to fluctuate by approximately a factor two as the shedding phase progresses. The highest values of $\omega_z(\phi)$ and $u_{rms}(\phi)$ in Figure 3.20 occurred at approximately the same phase ($\phi \cong \pi$). Conversely, the highest values of $\Lambda_{uu}(\phi)$ were associated with the lowest values of $\omega_z(\phi)$ ($\phi \cong 0$).

A description of the near wake turbulence can now be given as the vortex shedding process convects boundary layer turbulence into and away from the reference point. At shedding phases where $\omega_z(\phi)$ was relatively high, the phase fluctuating velocity was also relatively high and the values of $\Lambda_{uu}(\phi)$ were relatively low indicating the presence of

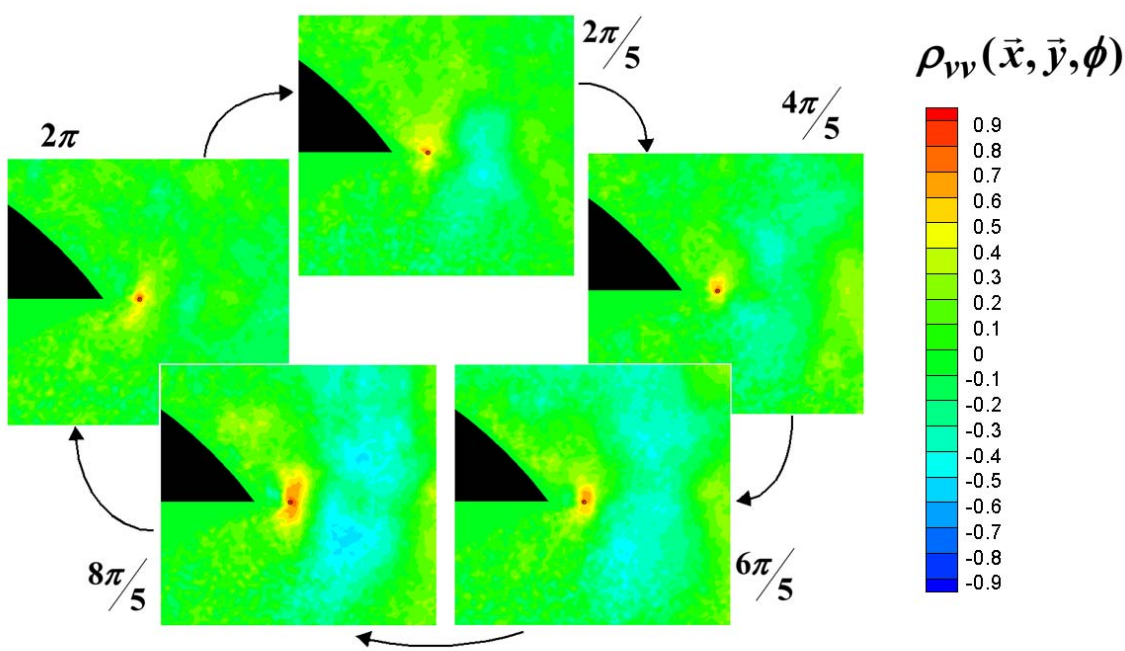

Figure 3.19: Two-point correlation coefficient for

highly vortical, small scale turbulence at the reference point. At shedding phases where the values of $\omega_z(\phi)$ were relatively low, the fluid at the reference point was relatively low disturbance with a corresponding larger length scale. This resulted in lower $u_{rms}(\phi)$ values, but higher turbulent length scales associated with these velocity fluctuations.

Observations made from Figure 3.20 imply that both the magnitude and spatial coherence of the phase fluctuating turbulent motions responsible for broadband sound production can be a strong function of the shedding phase. It was also found that instances of spatial coherence and high rms values for these motions occurred out of phase. As

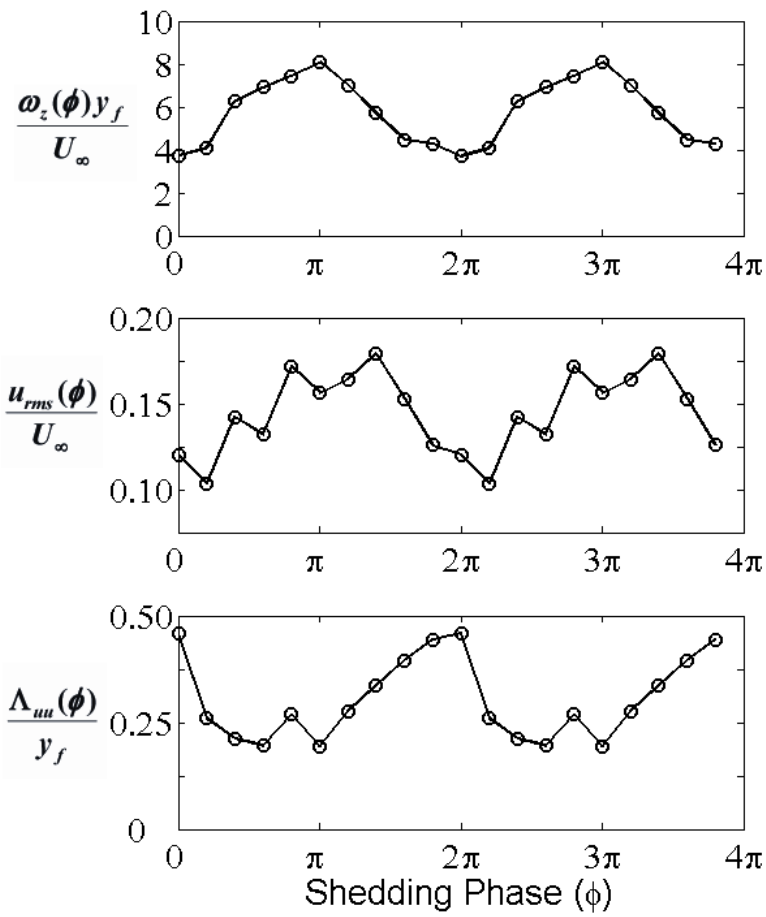

Figure 3.20: Turbulent length scale related to the phase fluctuating component of streamwise velocity plotted with the values of $\omega_z(\phi)$ and $v_{rms}(\phi)$ at $\vec{x}/y_f = \{0.5, 0\}$. Two cycles are shown.

previously discussed, sound is generated most efficiently by turbulent motions that have both relatively high velocity fluctuations and relatively high spatial coherence. Because these two conditions occurred π out of phase, the sound generated by the smaller scale motions related to the phase fluctuating velocity component would not be expected to be a strong function of the shedding phase despite the fact that both the turbulent length scale and relative magnitudes vary by relatively large amounts with ϕ. These observations are supported by acoustic results on this trailing edge geometry (see Section 7.5).

CHAPTER 4

EXPERIMENTAL SETUP & BOUNDARY CONDITION MEASUREMENTS

This section describes the Anechoic Wind Tunnel (AWT) facility and the measurements that were acquired for the boundary conditions and validation of the numerical work conducted by Stanford University.

4.1 Anechoic Wind Tunnel

The experiments conducted in the open test section of the AWT included velocity measurements using hot-wire anemometry, static wall pressure, unsteady wall pressure, and microphone array measurements of the radiated sound. The AWT consisted of a large anechoic chamber with an open jet style test section. The room treatment was rated to absorb 99% of incident sound waves above 100Hz. A schematic of the test section is shown in Figure 4.1. Laboratory air is drawn in through a turbulence management section and into a 8:1 contraction. The exit of the contraction is 0.62m by 0.62m in cross section, and defines the beginning of the test section.

The airfoil model was mounted vertically in the test section such that the forward 1/3 of the model was placed inside the inlet contraction. The flow in the test section was constrained on the upper and lower sides by a pair of end plates, which were treated with fiberglass board to reduce acoustic reflections. Two shear layers were formed by the flow exiting the inlet on the sides of the test section not constrained by the end plates. This

created a two dimensional open jet test section that allowed for the propagation of the trailing edge sound to the surrounding anechoic room. The exit of the test section is defined by the collector plate geometry as shown. The flow then moved through an acoustically treated diffuser section which leads to the primary fan. Information regarding the specifics of the design and construction of the AWT facility can be found in Mueller et. al (1992) and Scharpf (1993).

The collector section of the AWT was redesigned during the course of the project in order to reduce the amount of unwanted tunnel noise associated with the gathering of the open jet shear layers into the diffuser section. Initial sound measurements in the AWT showed that the parasitic sound generated by the original collector was prohibitive to the

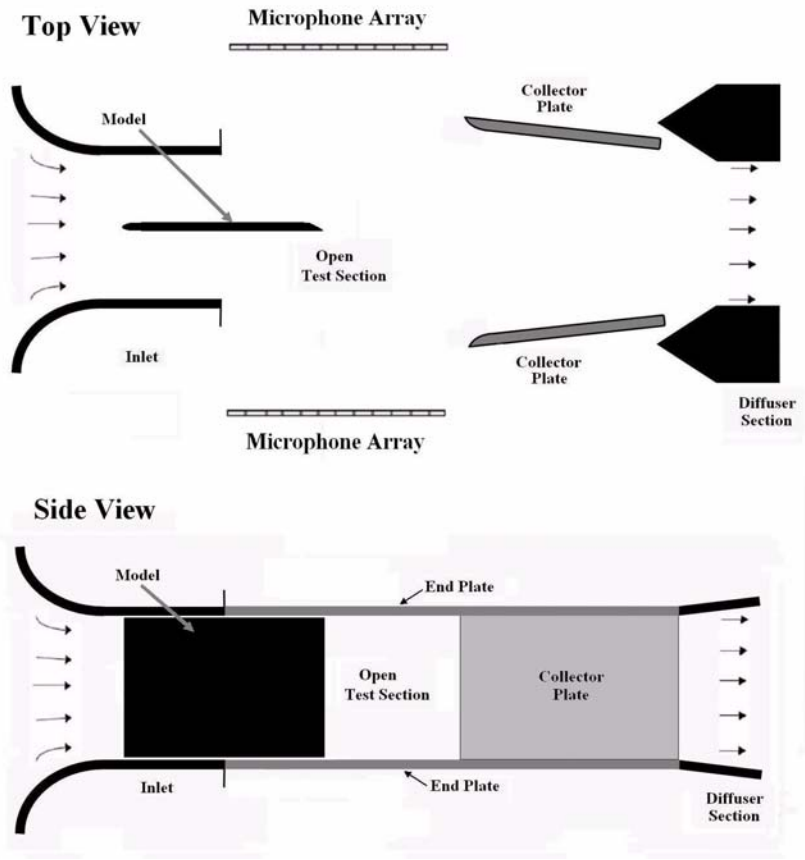

Figure 4.1: Sketch of the Anechoic Wind Tunnel at Notre Dame.
Flow is from left to right.

measurements of the trailing edge noise. The new design consisted of two collector plates, which gathered the shear layers before being ingested by the diffuser section. The collector plates were positioned such that the collector section generated as little parasitic noise as possible while keeping the length of the jet short enough to ensure jet stability. Small gaps were left between the end of collector plate and the diffuser section, which also helped to minimize the jet instability by allowing for a pressure release of the entrained flow upstream of the collector plates. Figure 4.2 shows the acoustic spectra for both the old and new collector designs obtained from a single microphone that was located 106.7cm from the centerline of the test section. The Sound Pressure Levels (SPL) are shown in 1/3rd octave bands. The new collector design was found to reduce the sound generated by the collector section by between 10 and 20dB.

Sound Pressure Levels in the AWT test section were measured utilizing a pair of microphone arrays positioned on either side of test section (shown in Figure 4.1). There

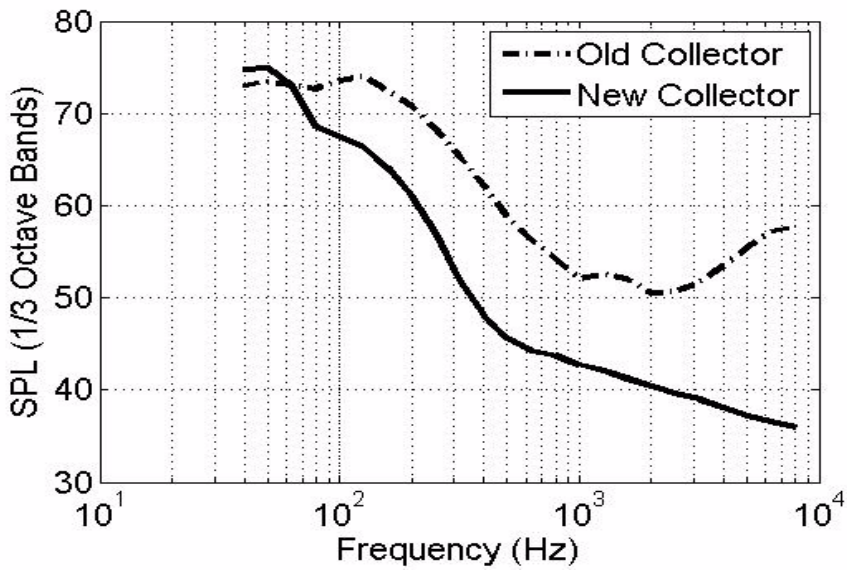

Figure 4.2: Comparison of acoustic spectra for both the old and new collector designs in 1/3rd octave bands.

are several advantages to using array measurements over single microphones measurements. The signal to noise ratio is increased by a factor equal to the number of microphones. It is also possible to use post-processing algorithms, called beamforming algorithms, to spatially localized sound sources in the test section. These algorithms have the ability to ignore noise caused by the operation of the AWT and included only sources of interest to this study. Each phased array contains 40 condenser microphones arranged in a stretched logarithmic spiral configuration (Underbrink, 1995) as seen in Figure 4.3. The logarithmic spiral design of the array was stretched in the horizontal direction allowing for better spatial resolution in the streamwise direction. The dimensions of the array are 59.8cm by 119.9cm. This microphone arrangement optimizes the array so as to reduce redundancy in the relative position vectors between microphones, thereby, minimizing any spatial aliasing that may results from inadequate spatial sampling. The locations of each microphone with respect to the array center are displayed in Table 4.1. Specifics on the design of the array can be found in Olson and Mueller (2004). The processing algorithms

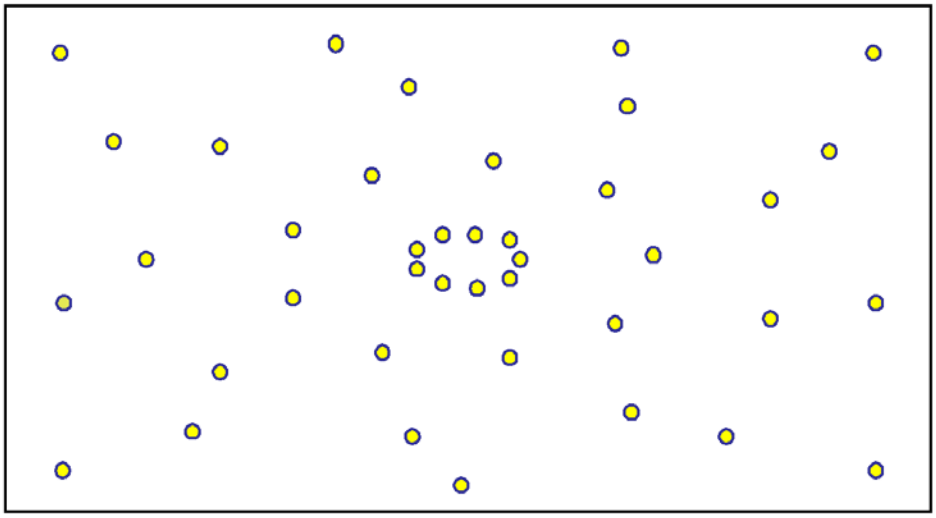

Figure 4.3: Stretched logarithmic microphone placement for phase acoustic array. The array size is 120cm by 60cm.

used for the phased array data are described in Chapter 6 and the results from these algorithms are described in Chapter 7.

4.2 Boundary Condition Measurements

Measurements of the boundary conditions in the AWT test section and trailing edge model were acquired and presented to Stanford for comparison to their computational work. These measurements included the static pressure distribution on the model, single component velocity measurements in the model boundary layers, and two component velocity measurements of the near wake turbulence using hot-wire anemometry. This section will present the results of these measurements.

The approach to providing the boundary conditions for the computations was to measure time-averaged velocity and time-averaged turbulence intensities in the x- and y-directions on the control surface at the model mid-span using hot-wire anemometry. Both multiple-wire, hot-wire probes and single wire, hot-wire probes were used to measure the flow field. Several data sets taken on different days were averaged to yield the final

TABLE 4.1

ARRAY MICROPHONE POSITIONS

Mic.	x (cm)	y (cm)	Mic.	x (cm)	y (cm)
0	-0.95	3.59	20	47.07	0.15
1	3.81	3.59	21	36.35	-15.66
2	7.38	1.53	22	8.18	-24.60
3	7.38	-1.22	23	-23.97	-21.16
4	3.81	-3.29	24	-44.21	-8.10
5	-1.35	-3.97	25	-44.21	8.40
6	-6.11	-2.60	26	-23.18	21.46
7	-7.70	0.15	27	19.29	30.40
8	-6.11	2.90	28	51.83	16.65
9	-3.73	13.90	29	60.17	-4.66
10	14.13	11.84	30	40.32	-23.91
11	25.64	4.28	31	1.03	-31.47
12	25.64	-5.35	32	-37.86	-24.60
13	12.54	-12.91	33	-59.69	-6.04
14	-6.11	-13.60	34	-52.94	15.27
15	-21.59	-8.79	35	-22.38	29.71
16	-27.15	0.84	36	59.77	29.02
17	-20.40	9.77	37	59.37	-29.41
18	8.57	24.21	38	-59.69	-29.41
19	36.35	15.96	39	-59.29	29.02

control surface database. Additional measurements, including the time-averaged flow field and second order turbulence statistics near the trailing edge were obtained to form a database for comparison with the computational results. The portion of the database presented herein includes U and V mean velocities, turbulence intensities and Reynolds stress profiles in the model boundary layers and wake.

Velocity measurements were acquired using a hot-wire probe consisting of two wires angled at 45-deg (x-wire probe). The x-wire probe was calibrated before and after each data set was acquired to verify the accuracy of the calibration. Angle corrections were applied to account for the difference in the probe angle with respect to the flow in-situ and in the calibration position. Commercially available constant temperature anemometers (a six-channel TSI IFA-300 and a two-channel IFA-100) were used for the hot-wire measurements.

4.2.1 Pressure Distribution

The static pressure was measured on the control surface and on the model surface. A Scanivalve electromechanical switching device was used to sequentially switch among pressure taps embedded in the model foil. A Scanivalve controller generated the signal to activate the electromechanical switch. The controller was user-controlled by the data acquisition PC, which was linked to the controlled through a serial cable. In addition, a pitot-static tube was utilized to measure the tunnel freestream velocity. A pressure transducer with a range of 2.5in-H2O was used as the transducer for both the Scanivalve pressure switch and the pitot-static tube.

All measurements presented in this section were acquired at Re = 1.9×10^6. Figure 4.4 shows the surface pressure distribution obtained along the suction and pressure sides

of the model. The results are compared with surface pressure measurements obtained by Blake (1975) using a geometrically similar model at a Reynolds number approximately 10% higher than measurements presented herein. To the precision of the spatial resolution of the measurements, the two sets of measurements show the same pressure peak location and the same separation location at x/c = 0.96. The measurements of Blake (1975) indicate a 9% lower magnitude pressure peak and a higher C_p in the separated region. The two sets of measurements demonstrate qualitative similarity.

The pressure side of the model maintains a zero pressure gradient from approximately 40% model chord to about 90% model chord. The pressure peak on the suction side of the model results from the camber concentrated near the trailing edge. Separated flow results from the adverse pressure gradient upstream of the trailing edge. The existence of a separated flow region was confirmed by the PIV measurements described in Section 2.

4.2.2 Boundary Layer Measurements

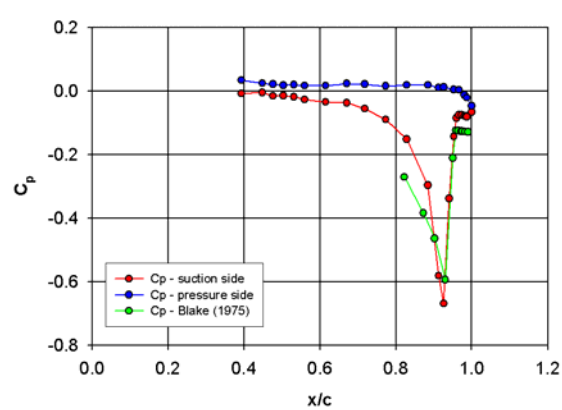

Figure 4.4: Model foil surface pressure distribution compared to the data of Blake (1975).

The results of flow measurements include a series of boundary layer profiles made along the suction side of the model foil and a coarse series of boundary layer profiles acquired along the pressure side of the model foil. Hot-wire measurements were not acquired in the separated flow region due to the ambiguity of measurement direction and erroneous magnitudes produced by a solitary hot-wire probe in reverse flow. In regions where hot-wire measurements would be rendered inaccurate but information was needed, PIV measurements were used to observe the flow (see Chapter 3).

Figure 4.5 show boundary layer profiles of the mean velocity and turbulence intensity within the boundary layer on the model suction side. The measurements were taken with a single wire hot-wire and show results for only the streamwise velocity component. Boundary layer measurements on the suction side were acquired in the zero, adverse and favorable pressure gradient regions. The denotation (Z), (F) or (A) next to the legend in each figure refers to the pressure gradient associated with each boundary layer profile (zero, favorable, and adverse). The denotation (Z/A), for instance, means that the pressure gradient changes from zero to adverse at that approximate x-location. It should be noted that the profiles are referenced to the suction side wall of the model. For the data acquired at x/c = 0.93 and 0.95 the absolute y-location of the wall has changed due to the beveled trailing edge; however for the sake of comparison among profiles, the wall location for all profiles is aligned at y = 0 in the plots. Flow separation occurs at x/c = 0.96.

Figure 4.6 present integral characteristics obtained from the suction side boundary layer profiles, including the 99% boundary layer thickness, δ, the displacement thickness, δ^*, the momentum thickness, θ, and the shape factor, H. The boundary layers were

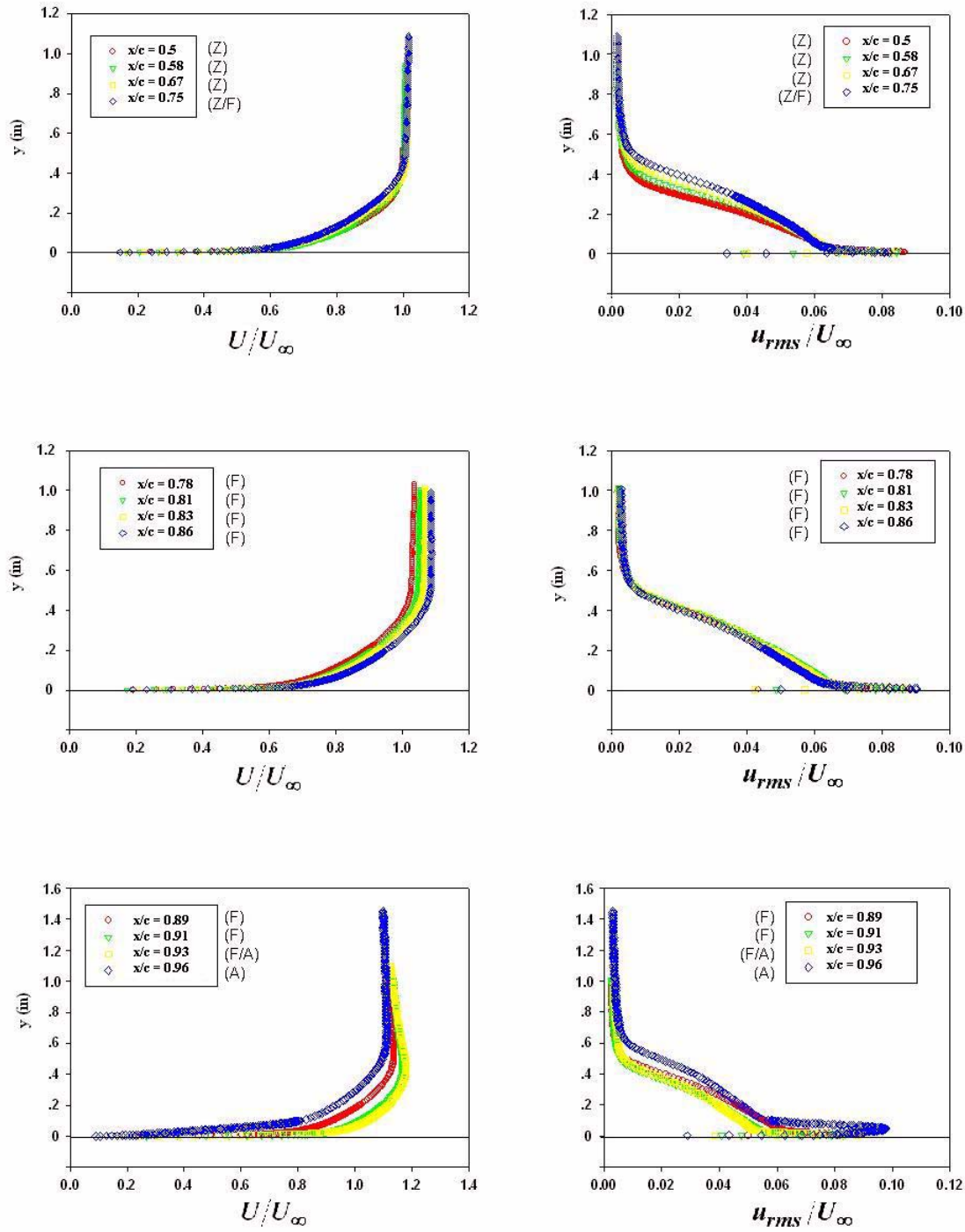

Figure 4.5: Boundary layer profiles for suction side of model. The images on the left show the mean components and the images on the right show the rms components.

scaled by the external velocity, U_∞. The boundary layer profiles were spline-fit and smoothed prior to integration. Figure 4.6 show that the external pressure gradient governs the evolution of the boundary layer characteristics up to separation. In the zero pressure gradient region *x/c* < 0.75, the boundary layer grows and maintains a constant shape factor (H = 1.4). In the favorable pressure gradient region (0.75 < *x/c* <0.93), the boundary layer thickness is first preserved in the weaker pressure gradient zone then decreases rapidly approaching the static pressure peak. The shape factor decreases in the favorable pressure gradient region. As the pressure gradient changes to adverse (*x/c* > 0.93), the boundary

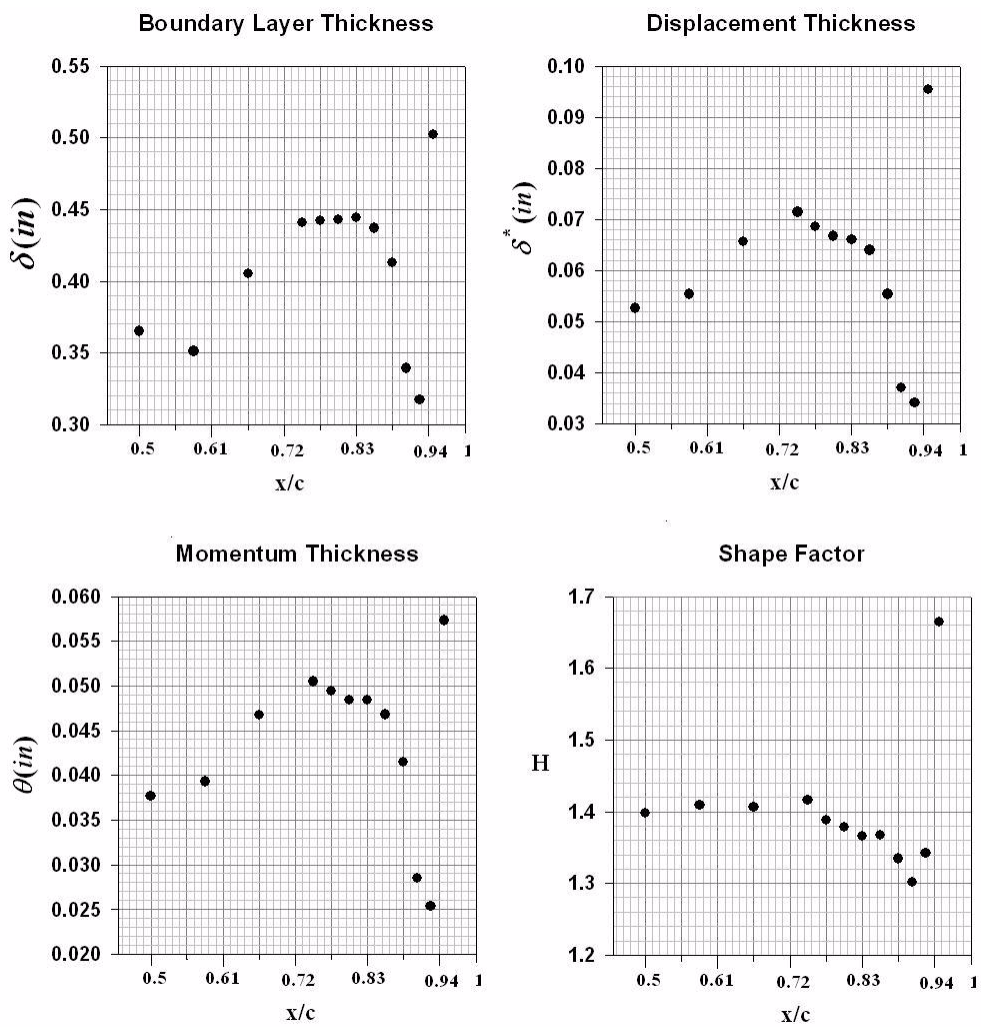

Figure 4.6: Evolution of boundary layer parameters over the suction side of model.

layer thickens and the shape factor increases to a value 19% higher than the zero pressure gradient value.

As a source of information for statistical turbulence noise generation models, the skin friction C_f was computed from the suction side boundary layers using the Clauser method. An example Clauser plot is shown in Figure 4.7 at $x/c = 0.78$ plotted in wall coordinates, $u+ = \mathrm{U}/\mathrm{u}_\tau(C_f U_\infty^2/2)^{1/2}$ and $y+ = \mathrm{y}\mathrm{u}_\tau/\upsilon$, where $u_\tau = (C_f U_\infty^2/2)^{1/2}$. The values $\kappa = 0.41$ and $B = 5.0$ were used for the logarithmic fit. Also shown in the plot is an interpolant used to estimate the velocity at $y^+ = 1$, the analytical form of the log law of the wall, and the curve $u+ = y^+$ below $y^+ = 10$. As shown in the plot, the hot-wire measurements reached into the viscous sub-layer. A clear logarithmic region was defined in each profile. Figure 4.8 shows the skin friction evolution over the suction side of the model. Because of the small extent of the log-layer in the profile acquired at $x/c = 0.95$, the Clauser method used may not accurately estimate C_f at that location.

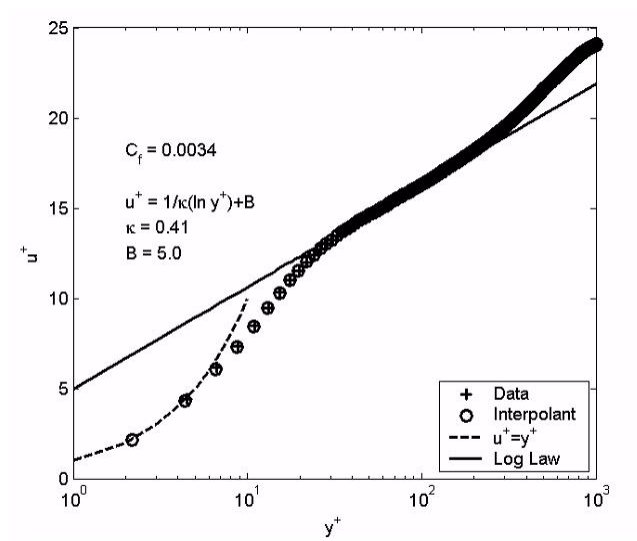

Figure 4.7: Example Clauser plot for suction side boundary layer at $x/c = 0.78$.

Boundary layer profiles taken along the model pressure side of the mean streamwise velocity, turbulence intensities and Reynolds stress are shown in Figure 4.9. Upstream of the trailing edge at $x/c = 0.94$ and $x/c = 0.97$, the streamwise normal turbulence intensity profile contains two peaks: a sharp peak near the wall and a broad peak farther away from the wall. The Reynolds stress peak also intensifies at the $x/c = 0.94$ and $x/c = 0.97$ locations. Figures 4.10 and 4.11 show the evolution of the boundary layer thickness parameters, shape factor, and skin friction for the pressure side boundary layer. These figures show the same discrepancies at the sharp edge as observed in Figure 4.9. The relatively large magnitude of the vortex shedding motions in the wake can explain these results as the large scale vortical motions observed in Figure 3.4 force the adjacent fluid in the boundary layer of the sharp edge back and forth. This hypothesis is also supported by unsteady pressure measurements on the pressure side of the model near the sharp edge which show large spectral magnitudes at the vortex shedding frequency (see Section 5.1).

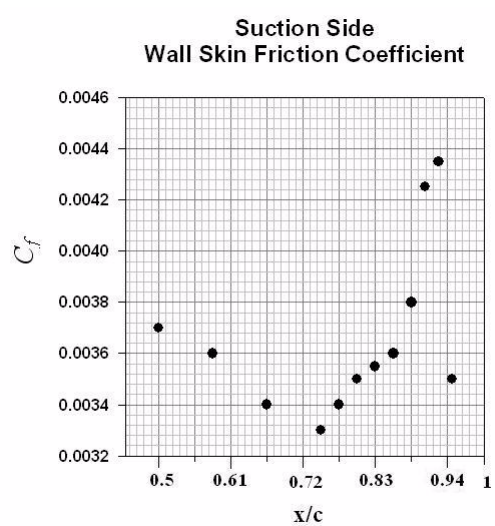

Figure 4.8: Evolution of wall skin friction for the suction side boundary layer.

4.2.3 Near Wake Turbulence

Wake profiles of U, u', V, v' and Reynolds stress are presented in Figs. 4.12-4.14 at a chord Reynolds number of 1.9×10^6. The x-location of these wake profiles begin at $x/y_f = 2$ downstream of the trailing edge to avoid entering the reverse flow region. The ordinate axis has been referenced to the centerline of the model such that the suction side of the model is at $y/y_f = 1$ and the pressure side of the model is at $y/y_f = -1$. As shown in Fig. 42, the wake drifts toward the pressure side of the model with increasing streamwise

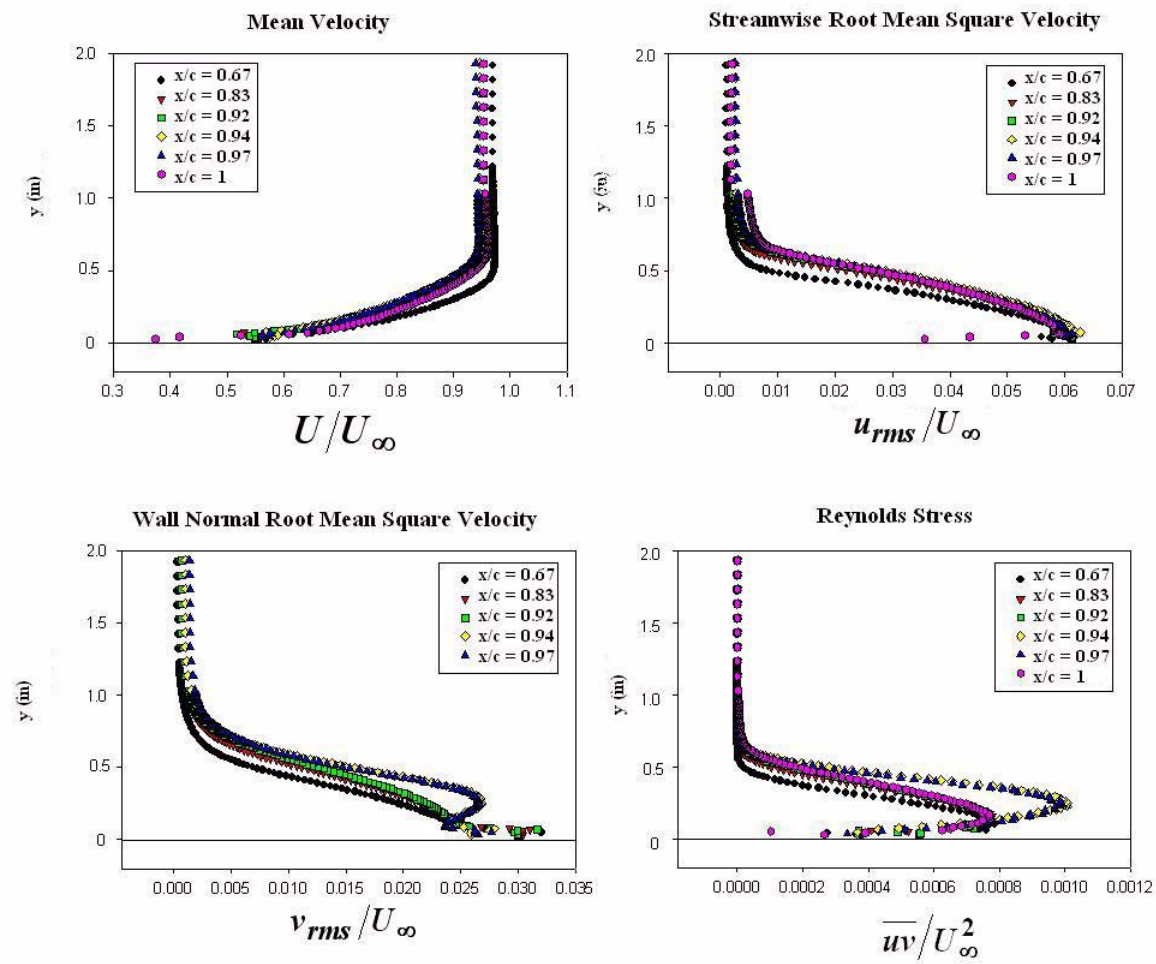

Figure 4.9: Boundary layer profiles for pressure side of model including mean velocity, turbulent velocity, and Reynolds stress.

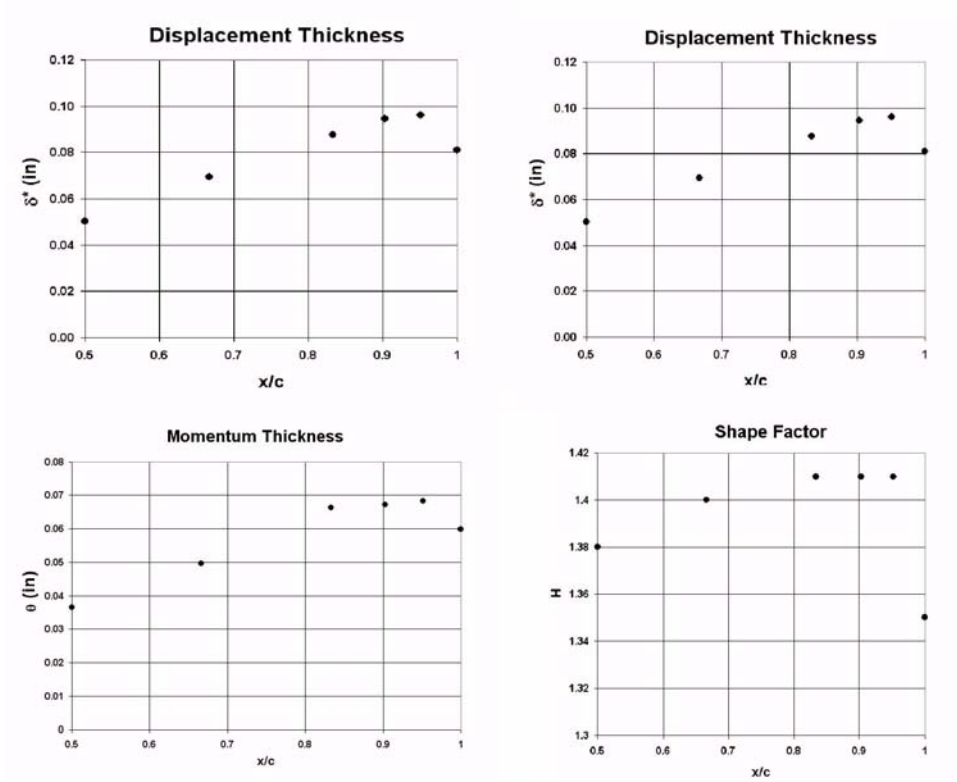

Figure 4.10: Evolution of boundary layer parameters over the pressure side of model.

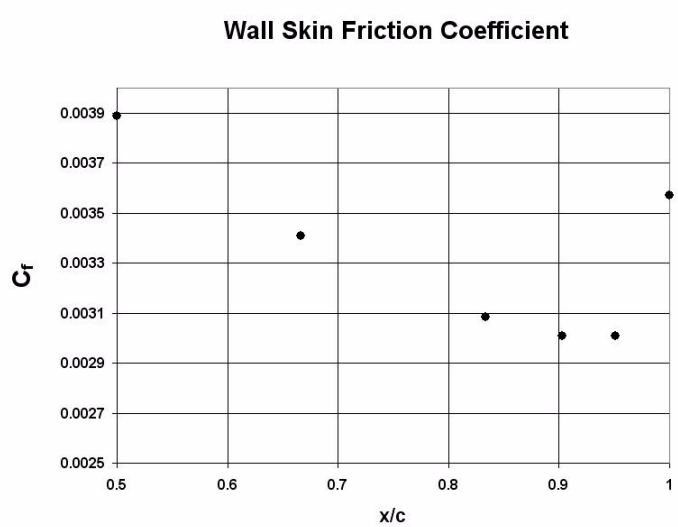

Figure 4.11: Evolution of wall skin friction for the pressure side boundary layer.

distance. The two causes of the drift are initial wake asymmetry due to the separated region on the suction side and the imposed mean v-component of velocity due to the circulation on the model foil (see Figure 4.12). As the boundary layers separate from model surface two regions of shear are created. These can be seen in Figure 4.14 at the locations of approximately y/y_f = -1 and y/y_f = 0in. These values can be compared to the values in the time averaged PIV measurements (see Figures 3.5-3.7).

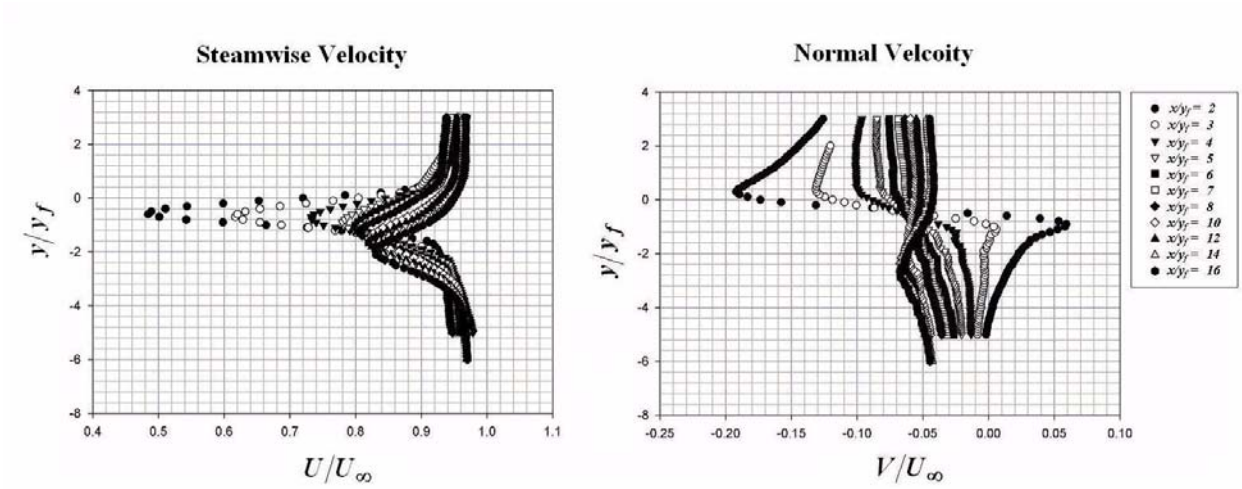

Figure 4.12: Mean streamwise and normal velocity components for Re = 1.9×10^6 in the near wake of the trailing edge.

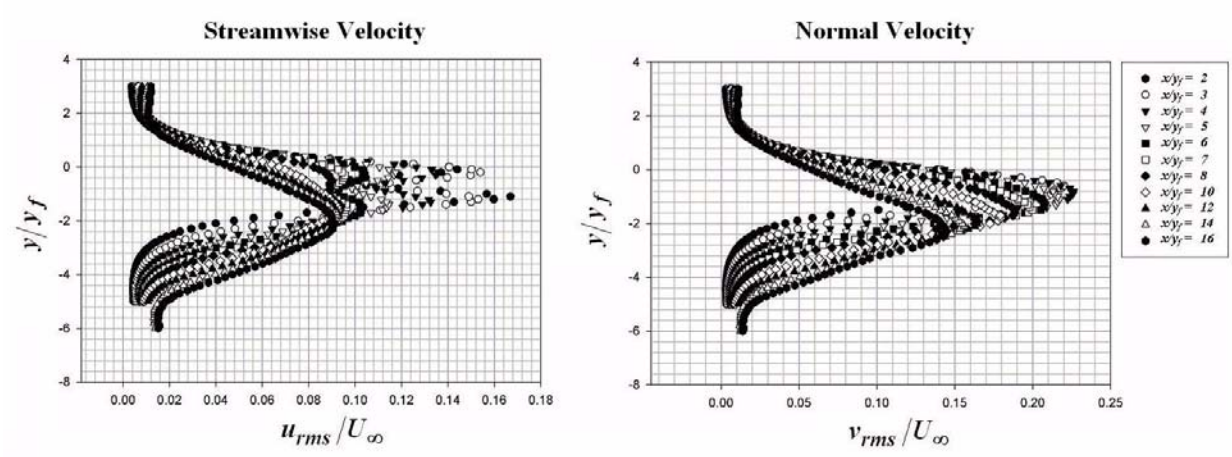

Figure 4.13: Root mean square streamwise and normal velocity components for Re = 1.9×10^6 in the near wake of the trailing edge.

The non-dimensionalization parameter y_f has been defined previously as the minimum distance between the dual peaks observed in the u_{rms} profiles (see Figure 4.13). This distance has been plotted between $x/y_f = 2$ and $x/y_f = 6$ track the locations of the centers of the upper and lower vortex streets. Figure 4.15 shows the wake thickness y_f computed as the distance between the streamwise turbulence intensity maxima profiles. Further downstream the two regions of shear merge into a single region of streamwise turbulence as the profile changes from wake-like to jet-like between $x/y_f = 8$ and $x/y_f = 10$, the quantity y_f becomes zero. The wake thickness is constant, $y_f = 1.0$in., at the profiles nearest the trailing edge, and this value is used for wake vortex frequency non-dimensionalization. This length scale was utilized because it describes the size of the separation region independent of the model thickness, which is important for appropriate scaling of separated wake flows with varied trailing edge geometries

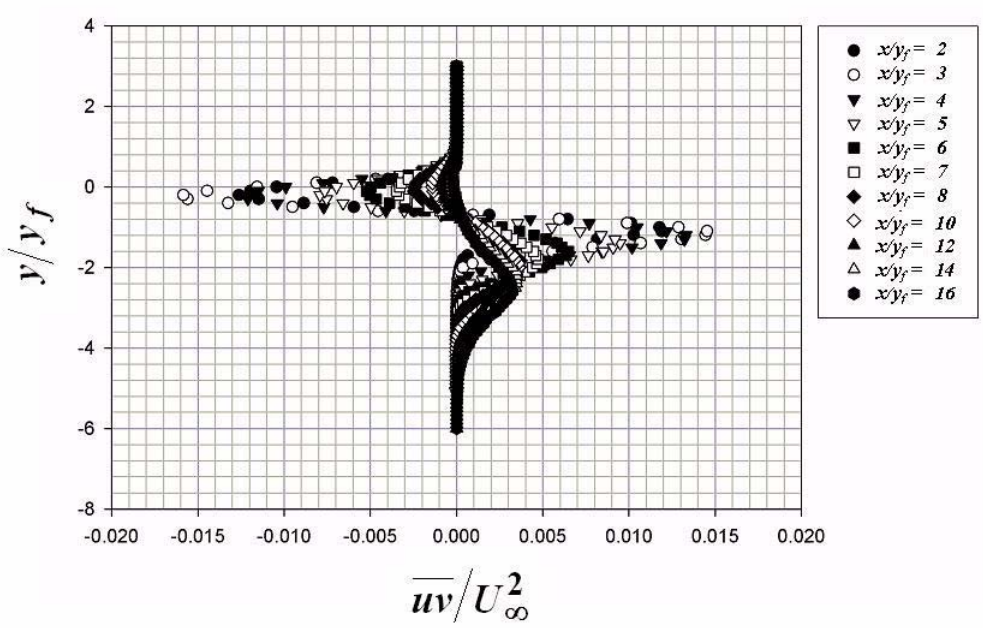

Figure 4.14: Reynolds stress profiles for Re = 1.9×10^6 in the near wake of the trailing edge.

4.2.4 Vortex Shedding Frequency

An uncalibrated single component hot-wire was placed into the wake of the trailing edge at approximately $x/y_f = 2.5$ downstream of the sharp edge in order to record the vortex shedding frequency. From these time series data in the wake, auto-spectral density spectra showed a narrow peak indicative of vortex shedding. The spectral values from the raw voltage signal were analyzed and the frequency with the large spectral magnitude relating to vortex shedding was recorded for Reynolds numbers ranging from $1.3\text{x}10^6$ to $1.9\text{x}10^6$. Defining a Strouhal number to be $St = 2\pi f y_f / U_\infty$, it was found that the average non-dimensional shedding frequency occurred at $St = 1.15 \pm 0.025$. This is in relative agreement with previous studies on a large variety of trailing edge geometries that have been summarized by Blake (1986) in which the Strouhal numbers were typically

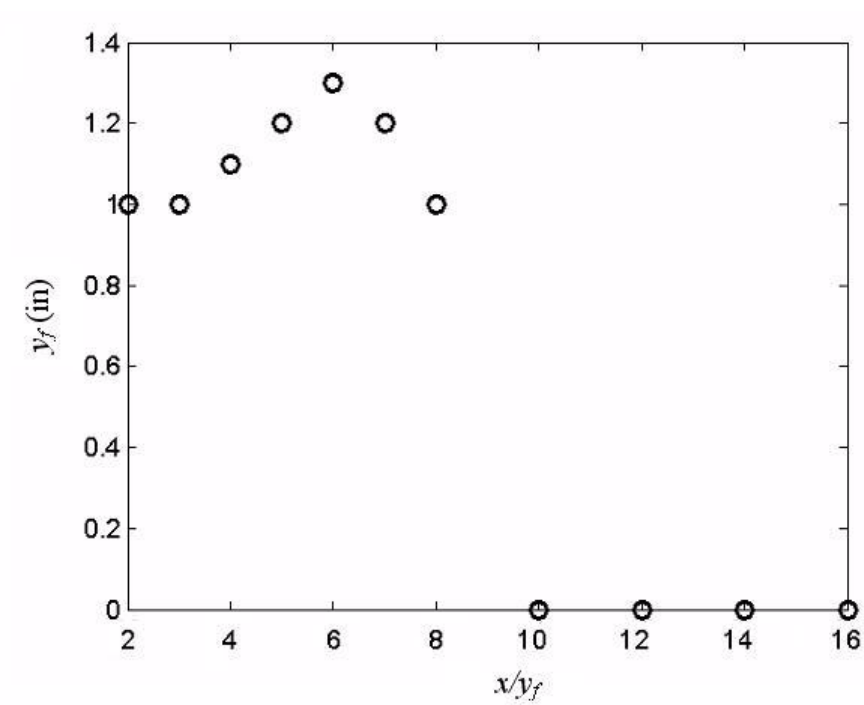

Figure 4.15: Non-Dimensionalization parameter y_f in the near wake

found to be approximately equal to unity. Table 4.2 shows the results from these measurements.

To measure any locking between the oscillations in the AWT open jet shear layer and the vortex shedding in the wake of the model foil, simultaneous hot-wire measurements were acquired in the vortex shedding path and the shear layer. These measurements (not presented) indicated no statistically significant linear coherence between the vortex shedding and the shear layer oscillations.

TABLE 4.2

VORTEX SHEDDING FREQUENCY IN NEAR WAKE

U_∞ (m/s)	Re (x10^6)	ω_{shed}	$y_f\omega_{shed}/U_\infty$
21.3	1.29	967.6	1.15
22.9	1.39	1036.7	1.15
24.4	1.48	1105.8	1.15
25.9	1.57	1175.0	1.15
27.4	1.66	1250.4	1.16
29.0	1.75	1319.5	1.16
30.5	1.85	1401.2	1.17
		Average	1.15

CHAPTER 5

UNSTEADY SURFACE PRESSURE MEASUREMENTS

Unsteady surface pressure sensors were flush mounted to the model surface. These sensors were arranged into both a spanwise and a streamwise array. The streamwise array consisted of condenser microphones positioned at the midspan and at the chordwise positions described in Figure 5.1. Sensors E and F are of particular interest as they are close to the sharp edge where the majority of the noise is generated. The spanwise array of condenser microphones was placed on the suction side of the trailing edge in the recirculating region 2.54cm upstream of the sharp edge at the same streamwise location as sensor D at locations z = -11.41cm, -3.81cm, -1.27cm, 5.08cm, and 13.97cm relative to the midspan of the model. These sensors are labeled H, I, J, K, D, and L, respectively. The microphones in the spanwise array were used to compute the spanwise correlation length scales

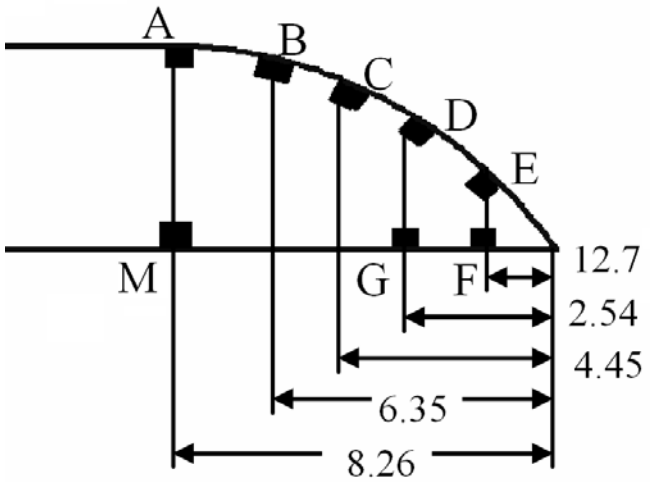

Figure 5.1: Spanwise surface pressure array. Dimensions are in centimeters.

associated with the vortex shedding process. Also presented below is a phase average of the surface pressure fluctuations with respect to the vortex shedding.

5.1 Unsteady Surface Pressure Spectra

Sensor H was used as a benchmark for the surface pressure sensors. Data measured by this sensor should agree with previously documented unsteady surface pressure measurements in a zero pressure gradient boundary layer. The auto-correlation of the pressure measured at sensor H is shown in Figure 5.2 non-dimensionalized by the dynamic pressure, q_∞, and the boundary layer displacement thickness, δ^*. The data agrees well with the published data for a boundary layer (Blake, 1986), except for the tonal "spike" observed at $\omega\delta^*/U_\infty \sim 10^{-1}$. This was possibly caused by the proximity of sensor H to the large scale vortex shedding in the near wake.

The spectra for each sensor in streamwise array is displayed in Figure 5.3 for $Re_c = 1.9\text{x}10^6$. Sensors A, B, F, and G are in attached regions (a) of the flow while sensors C, D, and E are in the separated region (b) of the flow.

5.2 Spanwise Correlation Length Scales

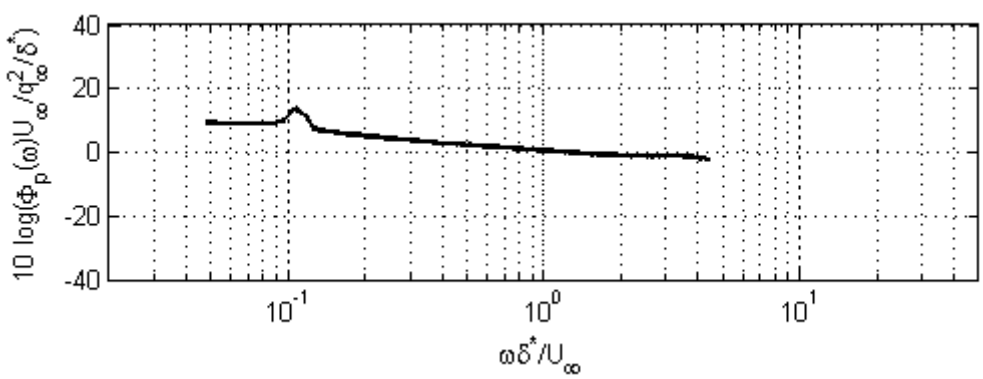

Figure 5.2: Unsteady surface pressure spectra in boundary layer at sensor location M.

The spanwise surface pressure length scale (Λ_3) was computed from the coherence function between the unsteady surface pressure sensors arranged in a spanwise array. The coherence function between two signals is defined as

$$\gamma(\omega)^2 = \frac{\left|G_{xy}(\omega)\right|^2}{\sqrt{G_{xx}(\omega)}\sqrt{G_{xy}(\omega)}}, \tag{5.1}$$

where G_{xx} and G_{yy} are the respective auto-correlation functions and G_{xy} is the cross-correlation function between the two signals. Integrating the coherence function at the shedding frequency over the spanwise direction (z),

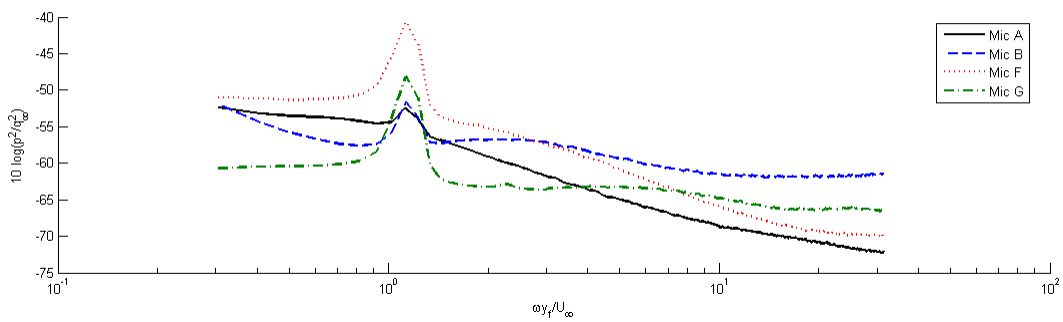

a) Pressure spectra for attached flow.

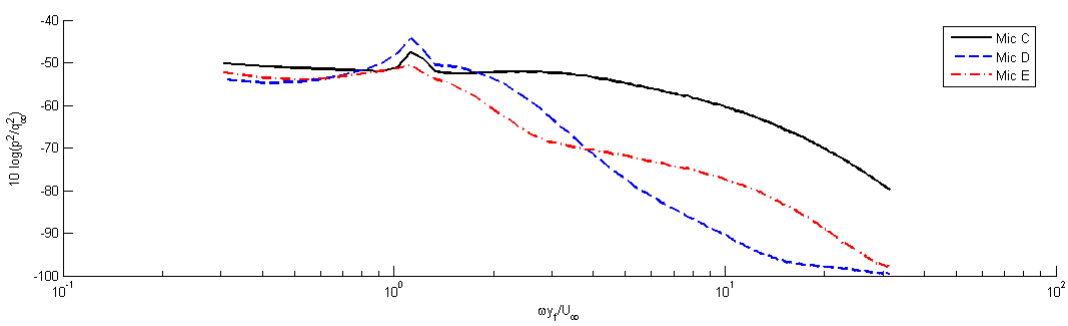

b) Pressure spectra for separated flow.

Figure 5.3: Spectra of the unsteady surface pressure for the spanwise sensor array for $Re = 1.9\text{x}10^6$.

$$\Lambda_3(\omega_{shed}) = \int_0^{\infty} \gamma(\omega_{shed}, z)dz, \tag{5.2}$$

yields Λ_3. This length scale has been used in the predictions of far field acoustics from measured unsteady surface pressures (Gershfeld, el al., 1988). Figure 5.4 shows this length scale at the shedding frequency as a function of Reynolds number. The spanwise length scales increase with free stream velocity, which suggests an increase in the tonal noise signature.

5.3 Phase Averaged Surface Pressure

The PIV results in Section 3.4 suggest that the small scale turbulence responsible for broadband noise production is dependent on the vortex shedding process. Therefore, the broadband surface pressure created by this small scale turbulence, would also be expected to exhibit this dependence on the vortex shedding phase. A further investigation of this possibility was completed by phase averaging the broadband component of the surface pressure signal.

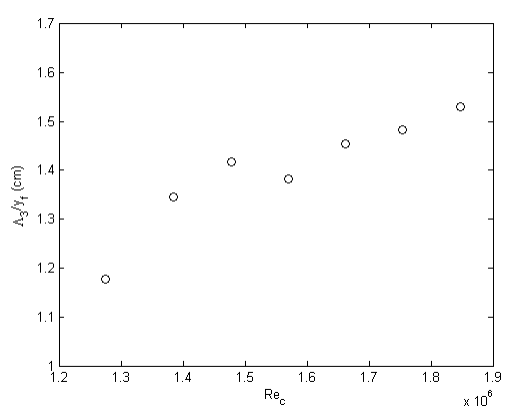

Figure 5.4: Spanwise coherence length scale at vortex shedding.

The tonal and broadband frequency contributions to a signal can be investigated independently. These two “parts” of the time series were separated utilizing a digital Butterworth filter over different frequency ranges. The tonal contributions of a pressure signal $p_{tonal}(t)$ were identified by band pass filtering the data about the vortex shedding frequency. The result being that only the frequency range related to the large scale wake instability was retained. The broadband contribution of a pressure signal $p_{hp}(t)$ can be investigated by high pass filtering above the vortex shedding frequency. This retained only the frequencies that are related to the smaller scale turbulent motions.

Phase averaging the high pass filtered pressure signal required a time series of the vortex shedding phase for the data acquired. This was accomplished by computing $p_{tonal}(t)$ for surface pressure sensor J, which was located in the separated region. The result was a nearly sinusoidal signal whose phase was easily determined. The phase at each instant of time was obtained by finding local extrema of $p_{tonal}(t)$ and separating the points between local maxima into 15 phase bins. Each measurement point was then assigned to a phase bin such that the broadband pressure fluctuations became a function of both time and phase $p_{hp}(\phi,t)$. The unsteady statistics of $p_{hp}(\phi,t)$ as a function of phase were found by “sorting” the data points into the appropriate phase bins and computing the root mean square value of each bin

$$\tilde{p}_{hp}(\phi) = \sqrt{\overline{p_{hp}(\phi, t)^2}}, \tag{5.3}$$

where the overbar represents a time average of data points that have the same ϕ value.

Figure 5.5 shows the modulation of the root mean square pressure in the broadband frequency range with shedding phase. The data are plotted on a decibel scale referenced to the total root mean square value of the high pass filtered pressure fluctuations $\sqrt{\overline{p_{hp}^2}}$. Two vortex shedding cycles are displayed to show the periodicity of the data. Both surface pressure sensors show an oscillation with the shedding phase. These data demonstrate that the magnitude of the high frequency surface pressure fluctuations is modulated by the vortex shedding process. The modulations observed for the suction side sensor are observed to be larger that those on the pressure side. The higher momentum fluid attached over the pressure side sensor may not be as easily distorted by the vortex shedding motions as the fluid in the stagnant separated region.

The broadband surface pressure modulation appears to be a function of the Reynolds number. This dependence is curious because the phase modulations observed in Figure 5.5 have been normalized by the total broadband surface pressure fluctuations. This suggests that for flow regimes where vortex shedding is present the amplitude modulation of broadband sound may be more prevalent at larger Reynolds numbers.

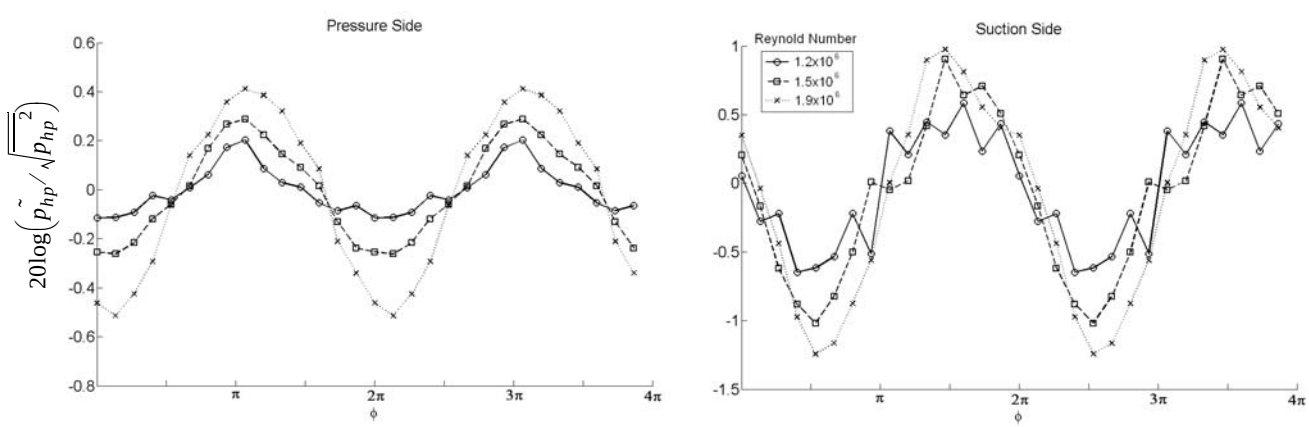

Figure 5.5: Phase fluctuating part of broadband unsteady surface pressure signal. Referenced to the broadband root mean square pressure.

CHAPTER 6

BEAMFORMING METHODS

The accurate measurement of sound generated by flow over a body is essential to experimental work in aeroacoustics. However, the sound field in most aeroacoustic experiments is complicated by the presence of unwanted or parasitic noise. The ability of an experimental system to separate this parasitic noise from the desired sound source is important for high fidelity measurements. Though this facility has been specifically design to produce low sound levels, some parasitic noise is generated by its operation. As such, it is necessary to quantify these unwanted sound sources and determine the limits associated with the measurement of sources in the AWT test section. The following sections will outline the specifics of the array design, the beamforming methods utilized, and results obtained from measured microphone array data.

6.1 Processing Techniques

The use of a phased microphone array for sound source interrogation is widely used for measuring aeroacoustic noise. Among other advantages the signal to noise ratio is increased by a factor of the number microphones in the array. Sources are spatially located by “steering” the array in post-processing to specific “look” locations. These methods are typically called beamforming techniques and are closely related to acoustic holography. By calculating the source field from an array of measured pressure signals, these

beamforming techniques solve the inverse acoustic problem. Three methods were utilized in this study: delay-sum (time domain) beamforming, weighted Cross Spectral Matrix (CSM) or frequency domain beamforming, and DAMAS. These three methods have limitations that will depend on the frequency content, relative positions, and the relative strengths of parasitic noise sources.

6.1.1 Delay-Sum Beamforming

Delay-sum beamforming is described by adding appropriate time delays to the individual microphone signals such that the acoustic signal from a source at the "look" location $\vec{x}_b$ would occur in phase. The time delay τ_n for the nth microphone located at $\vec{x}_n$ is equal to the acoustic travel time $\sigma(\vec{x}_n, \vec{x}_b)$ from $\vec{x}_b$ to the microphone, such that

$$\sigma(\vec{x}_n, \vec{x}_b) = \frac{\left\|\vec{x}_n - \vec{x}_b\right\|^2}{c_o}. \tag{6.1}$$

The individual phase and amplitude response unique to each microphone was determined from the array calibration (see section 6.2). The acoustic source strength at $\vec{x}_b$ is determined by shifting the individual microphone time series by time τ_n. This aligns the signals from each microphone such that contributions from a source located $\vec{x}_b$ at are in phase. The signals from all of the microphones are then averaged, cancelling signal components that are not in phase. It should be noted that some noise will be introduced to the signals as a result of the resampling of the data.

The microphone arrays have the obvious advantage of increasing the signal to uncorrelated microphone noise ratio by a factor of the number of microphones. By introducing phase delay beamforming techniques the arrays are able to distinguish

between spatially separated noise sources. The ability of the beamforming algorithms to distinguish between sound sources is limited in that the difference in phase delays between sources that are relatively close together may not be significant at frequencies with relatively large wavelengths causing contributions from sources not located at $\vec{x}_b$ to be included in the beamforming time signal. The resolution of beamforming techniques is further limited by spatial aliasing introduced by inadequate sampling of the sound field. This is similar to temporal aliasing and is responsible for the introduction of additional "noise" into the beamforming signal from sources not located at $\vec{x}_b$. The spatial resolution of the arrays used in this study is further investigated in the following section.

6.1.2 Weighted CSM Beamforming

The weighted Cross-Spectral Matrix (CSM) beamforming algorithms used in this study were given by Dougherty (2002). The output of these algorithms is a beamforming expression

$$b(\vec{x}_b) = \vec{w}^*(\vec{x}_b) \cdot A \cdot \vec{w}(\vec{x}_b), \tag{6.2}$$

which consists of the CSM (A) operated on by weighting vectors $\vec{w}(\vec{x}_b)$, where $\vec{v}^*$ denotes the complex conjugate of the vector $\vec{v}$. The CSM is composed of the cross-spectral values between the microphone signals at a desired frequency. The weighting functions $\vec{w}(\boldsymbol{x}_b) = \vec{C}(\vec{x}_b) / \left\| \vec{C}(\vec{x}_b) \right\|$ are determined from the propagation vector

$$C_n(\vec{x}_s) = \frac{e^{i\omega\sigma(\vec{x}_n, \vec{x}_s)}}{4\pi \left| \vec{x}_n - \vec{x}_s \right|}, \tag{6.3}$$

where ω is the circular frequency, $|\vec{x}_n - \vec{x}_s|$ is the distance from the "look" location to microphone *n*, and $\sigma(\vec{x}_n, \vec{x}_s)$ is the acoustic travel time. This method has the advantage of being able to "steer" the array signal to any point in space once the CSM is computed by simply applying the appropriate weighting vectors to A. For results shown in this investigation, the diagonals of the CSM have been eliminated because these auto-spectral terms do not provide any additional phase information about the sound field and because they can contain undesirable microphone self-noise components.

The spatial resolution can be further investigated by looking at the response of the array to a point source. This response is determined by the array Point Spread Function (PSF)

$$psf(\vec{x}_b, \vec{x}_s) = \left\| \vec{w}^*(\vec{x}_b)\vec{w}(\vec{x}_s) \right\|^2 . \tag{6.4}$$

Ideally this function would be unity when $\vec{x}_b = \vec{x}_s$ and zero everywhere else. However, the relative size of the array and the limited number of microphones creates regions where $\vec{x}_b \neq \vec{x}_s$ and $psf(\vec{x}_b, \vec{x}_s)$ values are significant. This is especially true for frequencies where the acoustic wavelength is of the same order of the array size. The PSF for several frequencies is shown in Figure 6.1 on a -10dB scale. Note that as the acoustic wavelengths (λ_a) get smaller the relative size of the mainlobe decreased as the spatial resolution of the array increases. The accuracy of the arrays is also limited by sidelobes in the $psf(\vec{x}_b, \vec{x}_s)$, which are caused by inadequate spatial sampling. These sidelobes are evident in Figure 6.1 as regions of statistically significant $psf(\vec{x}_b, \vec{x}_s)$ values located outside of the main lobe.

The array spatial resolution is often quantified by defining the array beamwidth as point at -3dB contour line of the mainlobe of the PSF. The relationship between the array beamwidth (BW) and the acoustic wavelength is linear such that

$$BW = k \cdot \lambda_a . \tag{6.5}$$

Because the array used for this investigation is stretched in the horizontal direction, the array beamwidth can be defined separately for both the x and y directions. Figure 6.2 shows the array beamwidth as a function of the acoustic wavelength. At the lower frequencies $(f < 1000Hz)$ the acoustic wavelength is on the same order as the array size, causing the beamwidth to stray from the linear relationship described in (6.5). For these frequencies the contours of the PSF no longer converge as seen in Figure 6.1a.

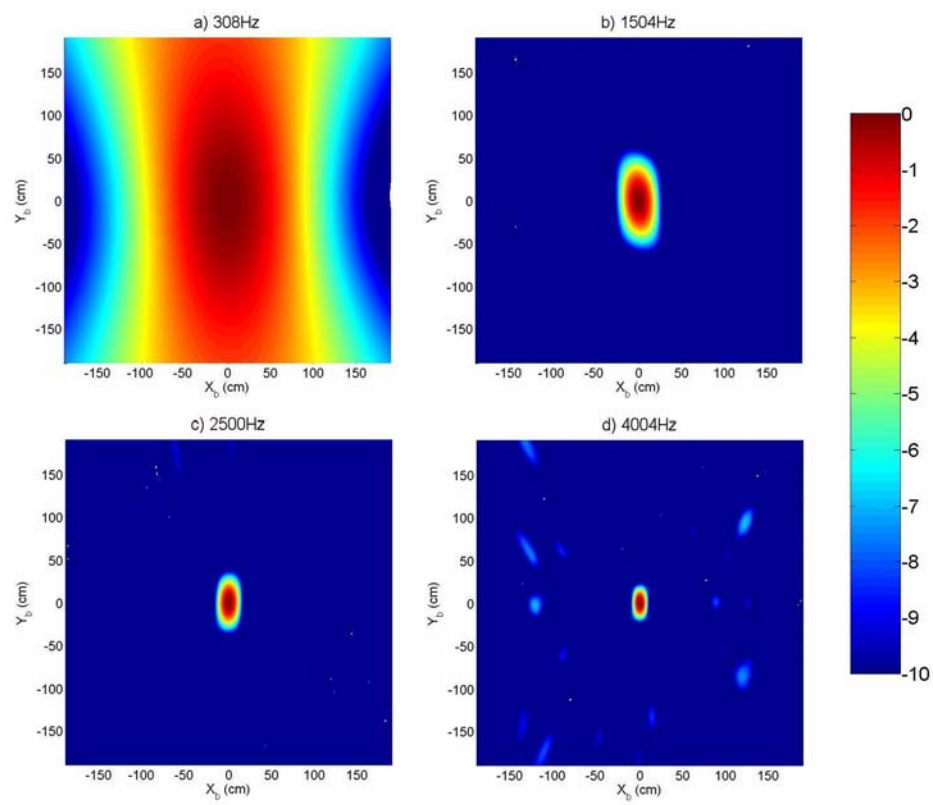

Figure 6.1: The point spread function or directivity pattern for the microphone array shown in Figure 2 at a distance of 170.5cm.

The acoustic spectra at $\vec{x}_b$ can be obtained by integrating $b(\vec{x}_b)$ over the desired source region and accounting for the PSF such that

$$G_{xx}(\omega) = \frac{\iiint b(\vec{x}_s)d\vec{x}_s}{\iiint psf(\vec{x}_{s_o}, \vec{x}_s)d\vec{x}_s}. \tag{6.6}$$

Spatial aliasing can induce inaccuracies in the measured sound field when multible sources are present as the mainlobe and sidelobes from one source interact with the mainlobe or sidelobes of another source. This is the main cause of error when attempting to evaluate equation (6.6) for a sound field with more than one source.

6.1.3 DAMAS

A Deconvolution Approach to the Mapping of Acoustic Sources (DAMAS) was presented by Brooks and Humphreys (2004). This method is based on the fact that the output of equation (6.2) is the convolution integral the point spread function with the true source field $q(\vec{x}_b)$,

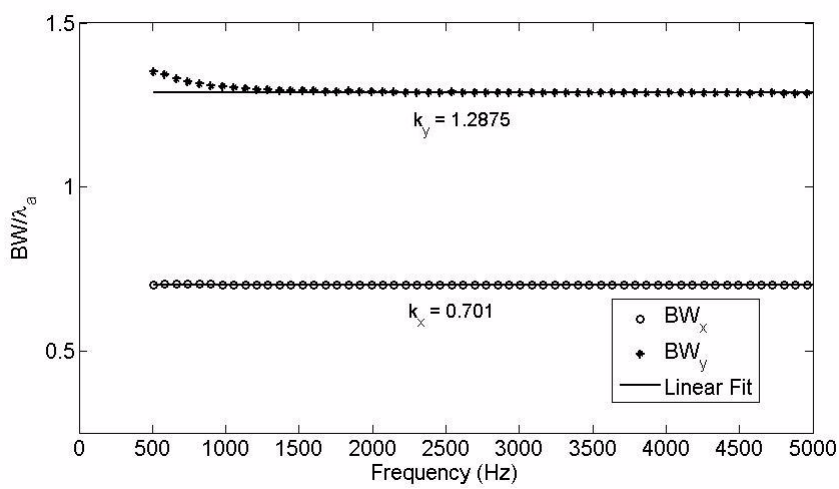

Figure 6.2: Array beamwidth as a function of acoustic wavelength

$$b(\vec{x}_b) = \iiint q(\vec{x}_s) \cdot psf(\vec{x}_b, \vec{x}_s) d\vec{x}_s . \tag{6.7}$$

Because both $b(\vec{x}_b)$ and $psf(\vec{x}_b, \vec{x}_s)$ are know it is possible to reduce (6.7) to a linear algebra problem

$$\vec{\boldsymbol{Y}} = B\vec{\boldsymbol{X}}, \tag{6.8}$$

where $\vec{\boldsymbol{X}}$ denotes the values of $b(\vec{x}_b)$ in vector form, the matrix B is composed of the values of $psf(\vec{x}_b, \vec{x}_s)$, and $\vec{\boldsymbol{Y}}$ is a vector of the unknown source terms $q(\vec{x}_b)$ in vector form. Brooks and Humphreys solved (6.8) utilizing a least squares method. This improved the beamforming results they obtained from both simulated and measured array data. DAMAS has the advantage of reducing the size of the source contribution areas and the eliminating sidelobes effects, which can cause erroneous results in the weighted CSM beamforming method. DAMAS is especially advantageous for problems with multiple sources of comparable magnitude. By deconvolving the PSF from the beamforming results the contributions from each source is effectively separated allowing for more accurate determination of source distribution.

Dougherty (2005) described an algorithm to solve (6.8) using iterative spectral techniques instead of a least squares method, which greatly reduced the processing time. Dougherty incorporated his algorithm into software plug-in called *Iterative Deconvolve 3D* for the program ImageJ[1]. This technique was utilized in conjunction with the methods described in section 6.1.2 to improve the weighted CSM beamforming results. All the

1. ImageJ is a public domain Java image processing program inspired by NIH Image. The author, Wayne Rasband (wayne@codon.nih.gov), is at the Research Services Branch, National Institute of Mental Health, Bethesda, Maryland, USA.

results presented used a maximum number of iterations of 100 with the spatial and Wiener filters turned off.

Spectra are obtained by integrating the DAMAS results over the desired source region

$$G_{xx}(\omega) = \iiint q(\vec{x}_s) d\vec{x}_s . \tag{6.9}$$

It should be noted that DAMAS results are not possible for frequencies where the acoustic wavelength is larger than the array size because the contours of the PSF do not converge. Thus, it was not possible to solve equation (6.9) for frequencies lower than 350Hz.

The advantages of DAMAS techniques is that the interaction of sidelobes from sources not located at $\vec{x}_b$ are removed. As such, the main source of error in integrating (6.6) is effectively eliminated allowing for a more accurate measurement of the acoustic sources at the "look" location. The mainlobes of the deconvolved beamforming maps have been reduced to one array beamwidth allowing the arrays to distinguish between sources that are up to two beamwidths apart.

The DAMAS techniques utilized in this investigation assume uncorrelated sources and as such the study is limited to appropriate sound fields. Though techniques have been developed that do not make this assumption (Brooks and Humphreys, 2006), the increased computation time for these algorithms is prohibitive. The algorithms developed by Dougherty also assume that $psf(\vec{x}_b, \vec{x}_s)$ is identical for all values of $\vec{x}_s$. This is a valid assumption for values of $\vec{x}_s$ that do not stray far from the normal vector $\vec{n}_a$ originating from the center of the array

$$(\vec{x}_s / \|\vec{x}_s\|^2) \cdot \vec{n}_a \sim 1 . \tag{6.10}$$

For look locations that do not meet this condition the contours $psf(\vec{x}_b, \vec{x}_s)$ will not be symmetric as observed in Figure 6.1, but will be skewed away from the array center-line. As such errors can be induced in DAMAS results if the PSF varies significantly over the source region. This will not be the case for the current study. It should be noted that some algorithms have been developed by (Ehrenfried and Koop, 2006) that account for a varying point spread function at the cost of additional processing time. It was not necessary to utilize these methods for this study because the values of $(\vec{x}_s / \|\vec{x}_s\|^2) \cdot \vec{n}_a$ were above 0.868.

6.2 Array Calibration

The actual array response is calculated through an eigenvalue analysis of an array calibration using a known monopole source (Dougherty, 2002). The array was calibrated with a B&K OmniSource type 4295 speaker. The speaker was aligned with the center of the array and placed 205cm away in the anechoic room. White noise from the speaker was recorded simultaneously by both the array and an ACO Pacific model 4016 microphone, which was used as the calibration standard. The eigenvectors of the CSM obtained from the calibration data were used to calculate a diagonal correction matrix that accounted for the phase mismatches between the individual array microphones

$$D_{cal} = diag\left(\frac{(\vec{v}_{cal})_1}{(\vec{v}_{theory})_1}, \ldots, \frac{(\vec{v}_{cal})_N}{(\vec{v}_{theory})_N} \right), \tag{6.11}$$

where $(\vec{v}_{cal})_n$ is the measured n^{th} eigenvector of the CSM and the theoretical eigenvectors is $(\vec{v}_{theory})_n = \vec{w}(\vec{x}_s)$. The CSM was corrected using

$$A_{corr} = D^*_{cal} \cdot A \cdot D_{cal}. \tag{6.12}$$

The magnitude of a single monopole source is related to the maximum eigenvalue of the CSM. Similarly, the microphone self-noise is related to the minimum eigenvalue of the CSM. An array calibration factor was found using

$$K(\omega) = \sqrt{\frac{p_{rms}(\omega)}{\lambda_{max} - h}}, \tag{6.13}$$

where $p_{rms}(\omega)$ is the measured root mean square pressure from the speaker, and both λ_{max} and h are the maximum and minimum eigenvalue of the CSM at ω, respectively. It was found that the relatively small acoustic reflections in the AWT caused some discrepancies in the results from (6.13). An average array calibration factor over all frequencies was utilized in order to eliminate these discrepancies. This was found to be appropriate given the relatively flat frequency response of the of array microphones.

6.3 Simulated Monopole Source

Array microphone data was simulated in order to test the effectiveness of the array in accurately producing spectra for known sources. The simulated array data was produced by first replicating a white noise source at a constant 50dB signal for an observer located 1m away. The individual microphone signals that would be generated by this source were computed by applying an appropriate phase delay and amplitude reduction according to the free space Green's function (6.3).

The ability of beamforming methods to reproduce the known spectra from a monopole source of 50dB was investigated using simulated array data. The source was positioned 107.7cm away and aligned with the center of the array. Figure 6.5 shows the

beamforming maps results for the simulated monopole source before and after deconvolution for 508Hz, 1992Hz, and 4004Hz. The abscissa and ordinate axis have been normalized by their respective array beamwidths. The SLP values have been normalized with respect to the original source strength (50dB) and have been shown on a -25dB scale to show more detail. Images (a) through (c) shown the beamforming maps and images (d) through (f) show the deconvolved maps. The DAMAS results show mainlobes that have been reduced in size to within a single beamwidth. In addition, the deconvolved maps have eliminated the sidelobes evident in the corners of the original beamforming maps. At 508Hz the acoustic wavelength is on the order of the array size and the beamforming map shows a relatively large mainlobe as a results. The DAMAS algorithm were able to reduce this mainlobe to within a single beamwidth.

6.4 Measured Array Data

Array data were acquired in the AWT to measure the accuracy of spectral results and the effects of parasitic sources on the results. The beamforming methods were evaluated utilizing two separate experiments. First, a Bruel and Kjaer OmniSource Speaker type 4295 was used to simulate a monopole source in the anechoic room. The accuracy of the beamforming methods was evaluated by comparing their spectral outputs to the known source strength. Secondly, the noise produced by the operation of the AWT and the ability of the beamforming methods to ignore this unwanted noise was evaluated by acquiring array data of the empty test section as a function of frequency and tunnel speed.

6.4.1 Array Data Acquisition Parameters

The analog to digital conversion system consists of 11, National Instruments model 4472 boards, each handling eight input channels with an additional dedicated channel for external triggering. A National Instruments PXI-1006 chassis houses the boards and synchronizes all boards mounted in the chassis. A National Instruments PCI card installed in the data acquisition PC connects to a PXI system control module mounted in the PXI chassis via a fiber-optic cable. The personal computer controls the acquisition system through the PCI to PXI connection. The sampling rate range for each channel is 1kHz to 102.4kHz, and each channel is anti-alias filtered at half the sampling rate. The digital resolution of each channel is 24 bits over an analog input range of 10V, translating to a voltage resolution of 1.19 V/bit. With synchronization, the maximum phase difference between signals acquired between channel 0 and channel 80 is less than 0.1-deg. at 1000Hz.

LabVIEW software provides the user interface to the analog to digital conversion hardware. Boards are synchronized so that all 80 channels are sampled simultaneously within the aforementioned phase error. LabVIEW virtual instruments developed at Hessert Aerospace Laboratory incorporate National Instruments data acquisition codes and use circular buffering to stream the data of the digitized array signals to the PC hard drive in the form of binary files.

For all the data presented 2^{21} samples were acquired at 20kHz. All fourier transforms have been completed utilizing an ensemble bin size of 1024 samples and appropriate Hanning windowing using Welch's averaged modified periodogram method of spectral estimation. This corresponds to a frequency bin width of 19.53Hz.

6.4.2 Monopole Source Test

The ability of the array to find spectral values in the absence of parasitic noise was tested in the anechoic chamber. A monopole source was aligned with the array center and placed 205cm away. White noise was produced by the speaker at an average SPL of 43.5dB at the array plane. The three beamforming techniques were performed on this data to compare to the known speaker output. For both the weighted CSM and DAMAS techniques, maps of the sound field were generated and spectra computed according to (6.6) and (6.9). The integration areas were set at five times the array beamwidth and the grid spacing was 1/20th of the beamwidth.

Figure 6.3 shows the random error produced by the three beamforming techniques. The delay-sum beamforming has the most significant error results with an average error of approximately 0.08dB. Both the weighted CSM and DAMAS techniques have much lower and nearly identical errors of about 0.005dB with the only exception being a range of lower frequencies 350Hz < f < 850Hz where the DAMAS results appear to have superior performance.

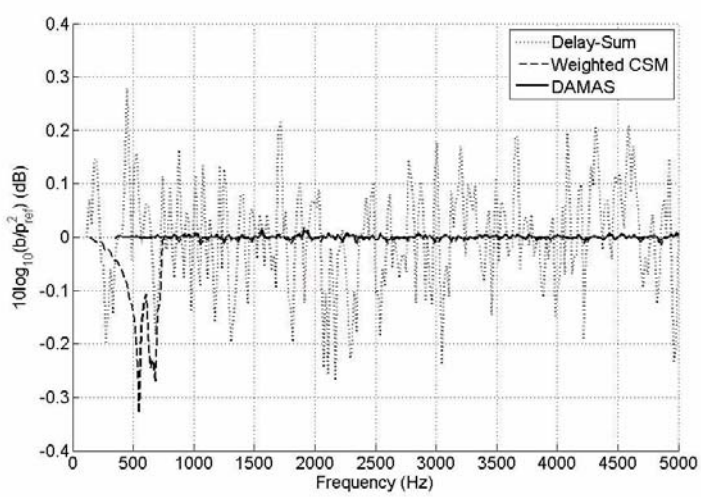

Figure 6.3: Error associated with each beamforming method for speaker data.

6.4.3 AWT Background Noise

The unwanted noise sources associated with the operation of the AWT can be separated into four separate categories. First, low frequency (100Hz < f < 500Hz) sound is generated by motor/fan noise which propagates upstream through the diffuser section. This is the loudest source of parasitic noise Secondly, inlet noise is produced in the intermediate to high frequency ranges (f > 350Hz) as the flow separates from the inlet into the open jet test section. Collector noise is also generated as the shear layers of the open jet test section are gathered and forced into the diffuser section causing noise in an intermediate frequency range (f > 500Hz) as the turbulent motions inherent to the shear layer impinge on the collector section. Finally, low magnitude high frequency (f > 2000Hz) noise was caused by the boundary layer flow over the upper and lower end plates of the test section.

Spectral values of the parasitic noise as measured by a single array were computed for the three beamforming methods. The beamforming location was positioned at the center of the empty test section. The integration region for equations (6.6) and (6.9) were centered along a line where the trailing edge would have been located. A beamwidth was added to either side this line to ensure that the entire trailing edge source region was included. A grid resolution of $1/20^{th}$ of the array beamwidth was utilized.

For reference the spectral values for an empty test section with no flow is shown in Figure 6.4 along with the spectra from a single array microphone. The integration bin width utilized for the SPLs presented in this section was 19.53Hz. Low frequency building noise is observed as the most prevalent source for the AWT at no flow. Even at relatively low SPLs the beamforming methods show reduced noise levels in comparison to single

microphone data. The weighted CSM and DAMAS methods are shown to have advantages over the delay-sum methods in rejecting the background noise for the no flow condition. The only significant difference between the weighted CSM and DAMAS methods was observed at the lower frequencies (f < 800Hz) where the sidelobes from the building noise has been successfully removed from the integration area. The noise limit of the array system appears to be approximately -20dB.

The parasitic noise in the test section was measured with the array at tunnel speeds ranging from 21.3m/s to 30.5m/s. The normal distance between the array plane and the beamforming plane was 170.5cm. Figure 6.5 shows several examples of the beamforming maps before and after deconvolution. Four frequencies are shown with images (a)-(d) displaying the weighted CSM results and images (e)-(h) displaying the DAMAS results. The beamforming plan is parallel to the array plan and intersects the center-line of the AWT test section. Flow is from left to right along the abscissa (x_b). The horizontal dashed

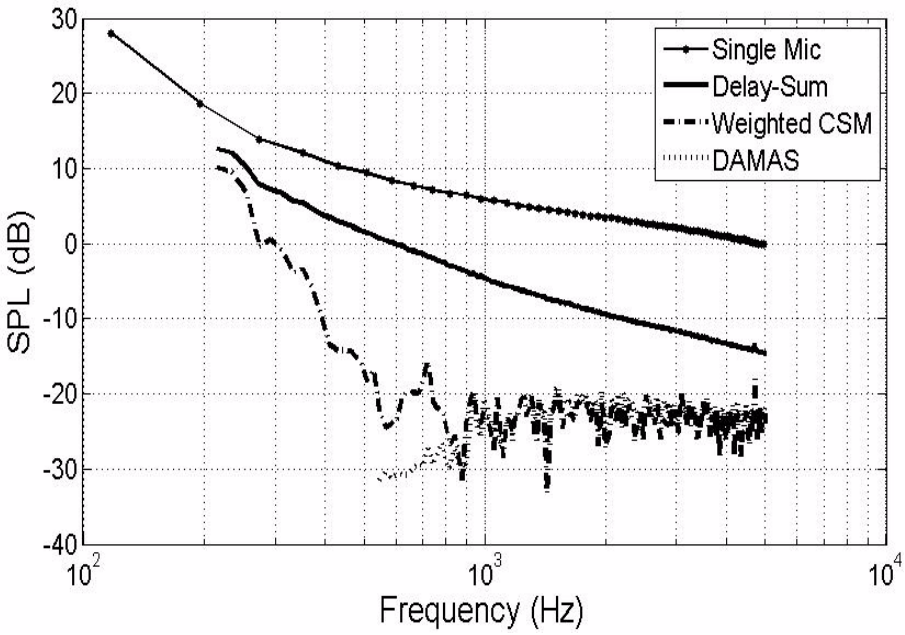

Figure 6.4: Background Sound Pressure Levels in empty AWT

lines at ±30.5cm show the locations of the upper and lower end plates of the test section, while the vertical dashed lines at the left and right edges of Figure 6.5 are the locations of the inlet and the leading edge of the collector. The contour levels of the DAMAS results show reduced SPL levels because the PSF has been deconvolved.

The advantage of the DAMAS algorithms can be observed in Figure 6.5 as the areas enclosed by the contour lines of constant pressure have been appreciably reduced, especially at the lower frequencies. The motor/fan noise is evident towards the diffuser section (right) in images (a) and (e). At 508Hz the inlet noise becomes the most significant source of tunnel noise. Some collector noise was also observed at this frequency. At the higher frequencies the inlet noise was mostly produced at the upper and lower boundaries of the test section. In addition boundary layer noise was generated by the flow over the upper and lower end plates of the test section.

Figure 6.6 shows the spectral values of the parasitic noise in the test section at 30.5m/s utilizing the weighted CSM and DAMAS beamforming methods. The

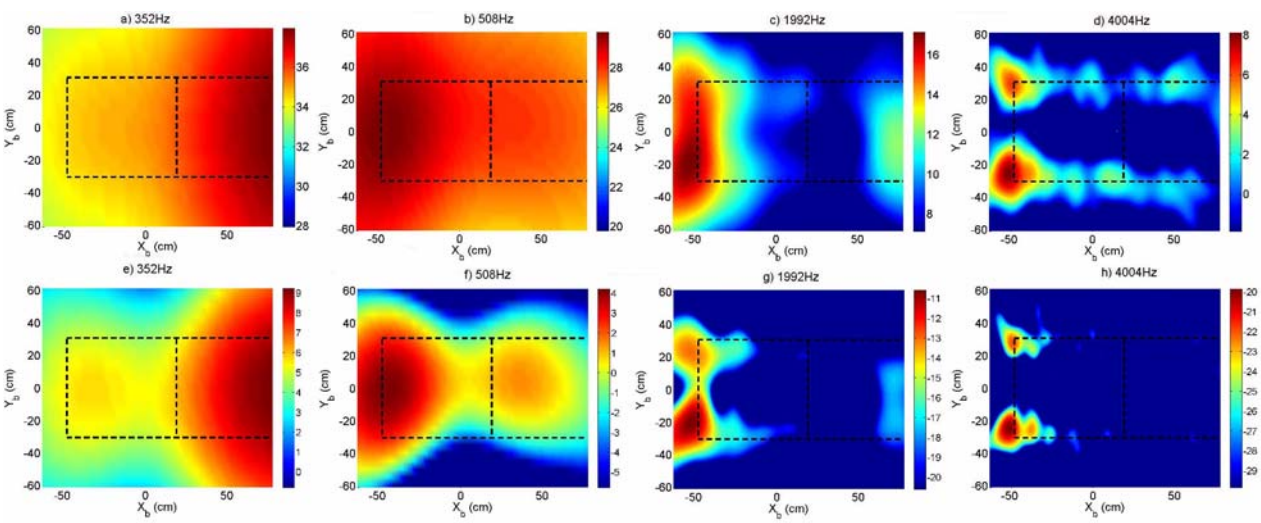

Figure 6.5: Beamforming (a-d) and DAMAS (e-h) maps of tunnel noise with an empty test section at U_∞[5] =30.5m/s in AWT. Flow is from left to right.

background levels for the DAMAS method with no flow is shown for reference. The low frequencies contain the highest magnitudes of parasitic noise and is indicative of fan/ motor noise that has propagated upstream through the diffuser section. The relatively large wavelengths at these frequencies make it difficult for the beamforming techniques to rejecting this noise. The advantage of DAMAS method is seen over the entire range of frequencies as the SPL in the test section were reduced by deconvolving the PSF from the parasitic noise sources in the tunnel.

The velocity dependence of the noise in the empty AWT test section was investigated for the data acquired from a single microphone. The amplitudes of the pressure fluctuations were scaled as U_∞^n using an adjusted SPL defined by

$$AdjustedSLP = SLP_o + \log\left(\frac{U_{ref}}{U_\infty}\right)^n, \tag{6.14}$$

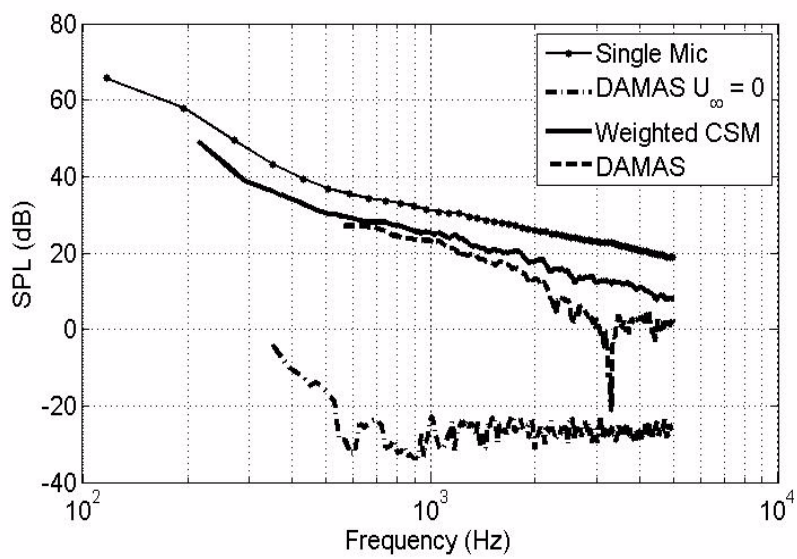

Figure 6.6: Sound Pressure Levels in empty AWT test section at $U_\infty = 30.5 m/s$ for an integration bin width of 19.53Hz.

where SPL_o is the unscaled SPL, U_∞ is the free stream velocity, and U_{ref} is a reference velocity. For this study $U_{ref} = 30.5$ m/s, which is the free stream velocity required to obtain a chord Reynolds number of 1.9×10^6. The value of n that produced the minimum variance in the adjusted SPL over four Reynolds numbers ranging from 1.3×10^6 to 1.9×10^6 was found as a function of frequency by comparing the integrated spectral density values in each 1/12 octave band. This optimum value of n is shown in Figure 6.7. The empty tunnel noise at the low frequencies $100\text{Hz} < f < 300\text{Hz}$ is composed mostly of motor/fan noise and appears to have the largest power velocity scaling ($n \sim 8$). The vortex shedding also occurs in this frequency range for the Reynolds numbers under investigation. Because the trailing edge noise will be expected to scale between U_∞^5 and U_∞^6 depending on the relative compactness of the source, the signal to noise ratio for these low frequencies will be smaller at the higher Reynolds numbers. It should be restated that

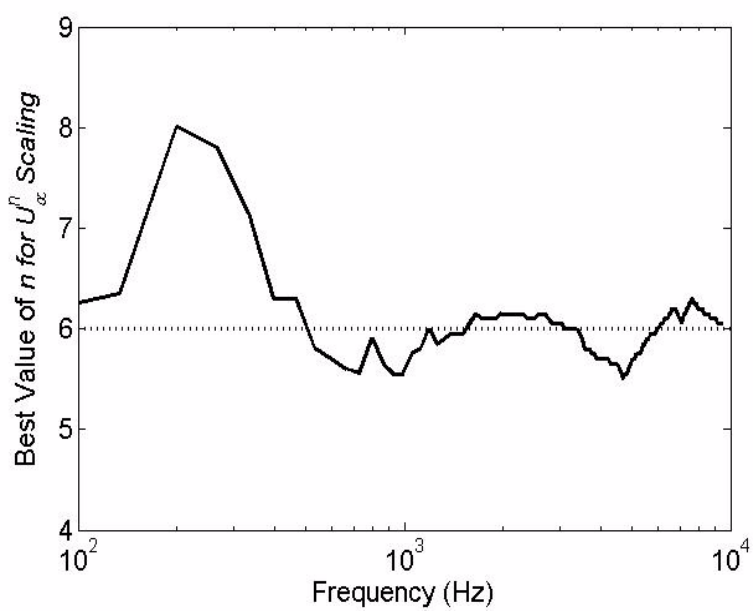

Figure 6.7: Optimal values of n for velocity scaling of tunnel noise with

this is also the frequency range where the beamforming methods are least effective because the acoustic wavelengths are on the same order as the array size. The velocity scaling of the empty tunnel noise in the intermediate and higher frequencies ($f > 300$Hz) was found to be approximately U_∞^6, which is what would be expected for compact dipole sources. In this same frequency range the trailing edge noise will be expected to scale between U_∞^5 and U_∞^6 depending on the relative compactness of the source meaning that the signal to noise ratio will most likely remain of the same order for all of the Reynolds numbers, unlike the low frequency range.

CHAPTER 7

TRAILING EDGE SOUND MEASUREMENTS

This section presents the results obtained from utilizing the beamforming methods discussed in the previous section to produce spectral values for the trailing edge noise. All SPL levels presented are the SPL levels computed at the array plane for integration bins of 19.53Hz. In all the results presented, the array plan is parallel with the model 106.7cm from the trailing edge. The center of the arrays were located 12.7cm upstream of trailing edge. It should be noted that an exact comparison of the parasitic tunnel noise presented in Section 6.4.3 to the results presented herein is not valid as the presence of the model has modified the boundary conditions in the test section. As such, a simple subtraction of the measured empty test section sound field from the measured trailing edge sound field based on the superposition of sources is not appropriate. However, the parasitic tunnel noise sources presented in Section 6.4.3 are relatively close (within approximately 5dB) to those observed in the trailing edge sound field, making a qualitative comparison between the empty test section case and the trailing edge test case possible, especially at the lower frequencies where the motor/fan noise would not be expected to be modified by the presence of the model.

7.1 Beamforming Maps

Figures 7.1 and 7.2 presents SPL maps generated by the pressure and suction side array, respectively, using beamforming algorithms on a grid of points located at a plane that was parallel with the lower surface of the model. The frequencies illustrated are 352, 508, 1992, and 4004Hz at a chord Reynolds number of $1.9\text{x}10^6$. Flow is from left to right along the abscissa (x_b), which is parallel to the streamwise direction. The ordinate (z_b) is

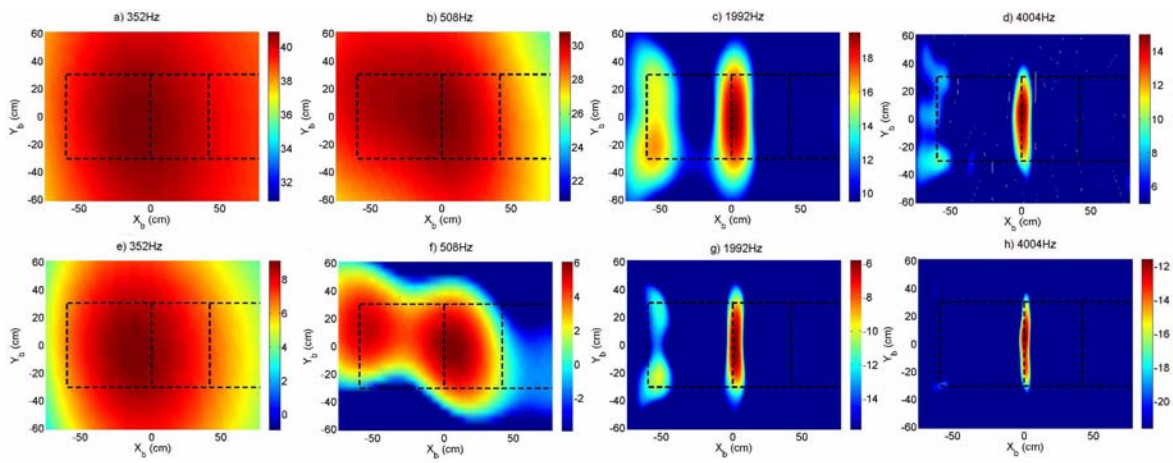

Figure 7.1: Beamforming (a-d) and DAMAS (e-h) maps for pressure side phased array at $Re_c = 1.9\text{x}10^6$. Flow is from left to right.

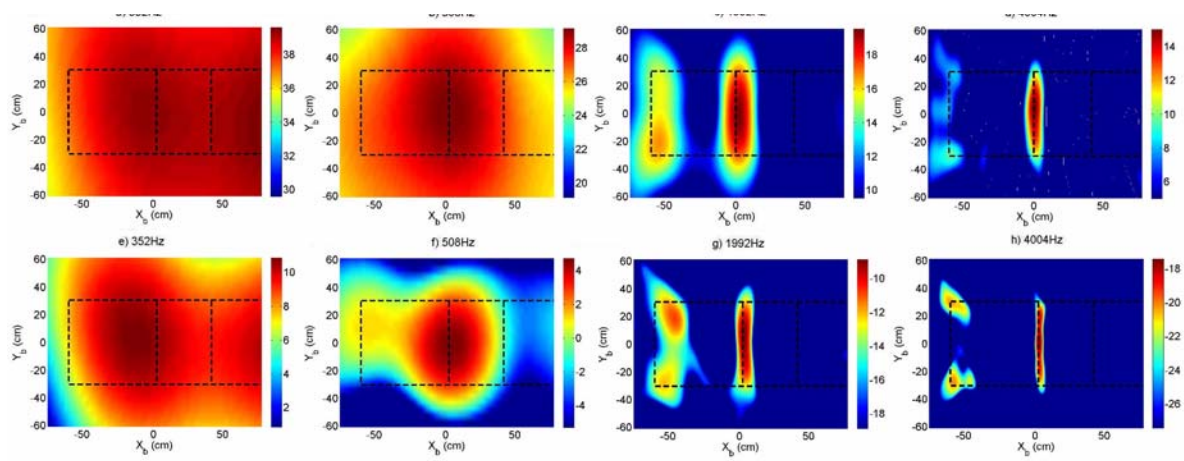

Figure 7.2: Beamforming (a-d) and DAMAS (e-h) maps for suction side phased array at $Re_c = 1.9\text{x}10^6$. Flow is from left to right.

parallel with the span of the model. The horizontal dashed lines at ±30.5cm show the locations of the upper and lower end plates of the test section, while the vertical dashed lines at the left and right sides of Figures 7.1 and 7.2 are the locations of the inlet and leading edge of the collector plate, respectively. An additional vertical dashed line at X_b = 0cm represents the location of the sharp trailing edge in the test section. The contour levels in each SPL map are scaled on a -10dB range. The upper limit of the scale is the map maximum at each frequency. Images (a)-(d) show the weighted CSM results and images (e)-(h) show the DAMAS results.

In addition to the tunnel noise, the trailing edge noise, is also observed at X_b = 0cm. The trailing edge noise is distinctly recognizable at the frequencies displayed despite the fact that the parasitic sources can be of the same order of magnitude. At the lower frequencies the ability of the beamforming algorithms to distinguish between trailing edge and parasitic noise decreases due to increased acoustic wavelengths. It is at these frequencies that the DAMAS techniques were most effective in separating tunnel noise from trailing edge noise. The trailing edge source shown in Figures 7.1 and 7.2 is observed to be non-compact at frequencies where the array beamwidth is smaller than the model span (f > 450Hz). It is also recognizable that the source strength decreases with increasing frequency.

7.2 Trailing Edge Spectra

The three previously discussed beamforming methods were utilized to obtain spectra for the trailing edge data. The integration regions for equations (6.6) and (6.9) were defined such that they enclosed the entire trailing edge source region as observed in the beamforming maps (see Figure 7.1 and 7.2). This source region varied with frequency

and the integration region was adjusted appropriately. Specifically, the integration region was set to be twice the beamwidth in either direction of the trailing edge line source. At lower frequencies (f< 750Hz) where parasitic source contributions from the inlet, motor/ fan, or collector noise merged with the trailing edge source contributions (see images a, b, e, and f in Figures 7.1 and 7.2), the integration regions were defined as the half distance point between the center points of the parasitic source and the trailing edge. This was necessary in order to ignore contributions from parasitic sources to the trailing edge spectral values. It should be noted that this may have increased the relative error associated with the measurement of the trailing edge noise at the lower frequencies where the array beamwidth was relatively large because a portion of the trailing edge source region was necessarily ignored and a portion of the parasitic source was necessarily included. The integration regions were defined in the aforementioned manner to minimize this effect.

A combination of the various beamforming methods were used over different frequency ranges to generated the best possible power spectral density values. The delay-sum beamforming was found to best resolve the vortex shedding noise produced by the flow over model (100Hz < f < 250Hz). Delay-sum beamforming to a point on the mid-span of the trailing edge was found to ignore some trailing edge noise at frequencies where the model span was larger than array beamwidth and was not utilized for frequencies higher than vortex shedding. The DAMAS methods were found to be most advantageous as the interactions between the mainlobe and sidelobes associated with the parasitic tunnel noise was deconvolved from the trailing edge source levels. DAMAS was not possible for frequencies below 550Hz because the PSF does not have converging

contour lines. The weighted CSM beamforming method was used for the intermediate frequency range between the delay-sum and DAMAS methods (250Hz < *f* < 550Hz*)*.

Examples of this combined spectra for both arrays at chord Reynolds numbers of 1.3×10^6 and 1.9×10^6 are shown if Figure 7.3 and 7.4 compared with the spectra for a single array microphone positioned in the center of each respective array. At the tonal frequency the beamforming methods do not reject sound because the shedding noise is at

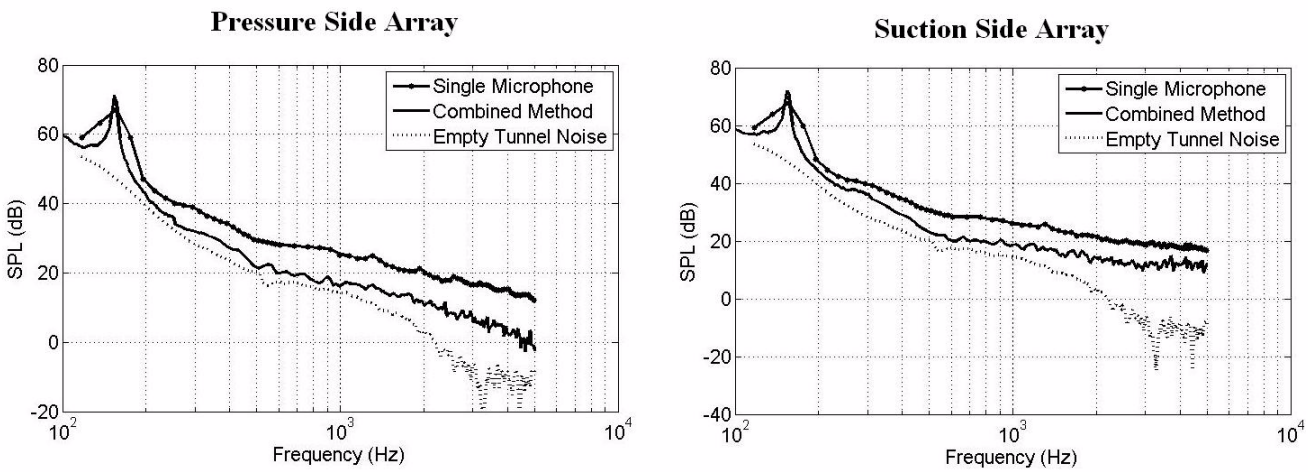

Figure 7.3: Example of combined beamforming method spectra compared to that of a single microphone for trailing edge data at Re = 1.3×10^6.

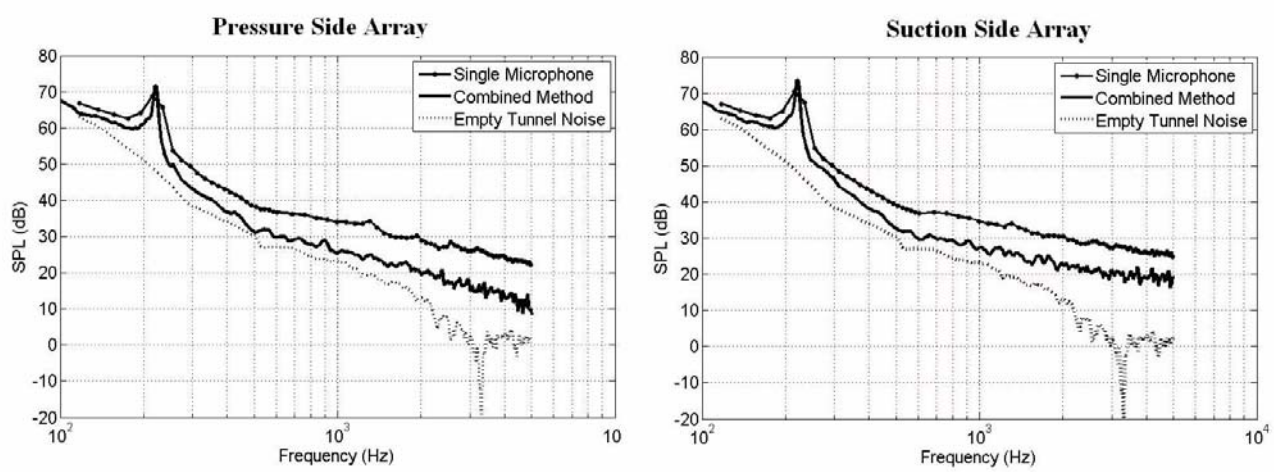

Figure 7.4: Example of combined beamforming method spectra compared to that of a single microphone for trailing edge data at Re = 1.9×10^6.

least 10dB louder than the tunnel noise at this frequency. The combined beamforming method spectra are observed to reject approximately 6dB of noise over the single microphone spectra at frequencies higher than the shedding frequency. The largest source of tunnel noise at these frequencies was observed in Figure 7.2 to be composed of inlet noise at approximately the same magnitude as the trailing edge noise. The summation of these equivalent sources results in an added 6dB of sound measured by the single microphone as compared to the true trailing edge spectral values.

There is a noticeable difference in the spectral values in Figure 7.3 as measured between the pressure side and suction side of the model. This difference is shown in Figure 7.5, which shows the SPL values for both arrays at Re = 1.9×10^6. The spectral values are typically 2-3 dB higher for the suction side array at the lower to intermediate frequency ranges and up to 8dB higher in the higher frequency range. In addition, the slope of the broadband noise $(\omega y_f / U_\infty > 10)$ appears to be greater for the pressure side

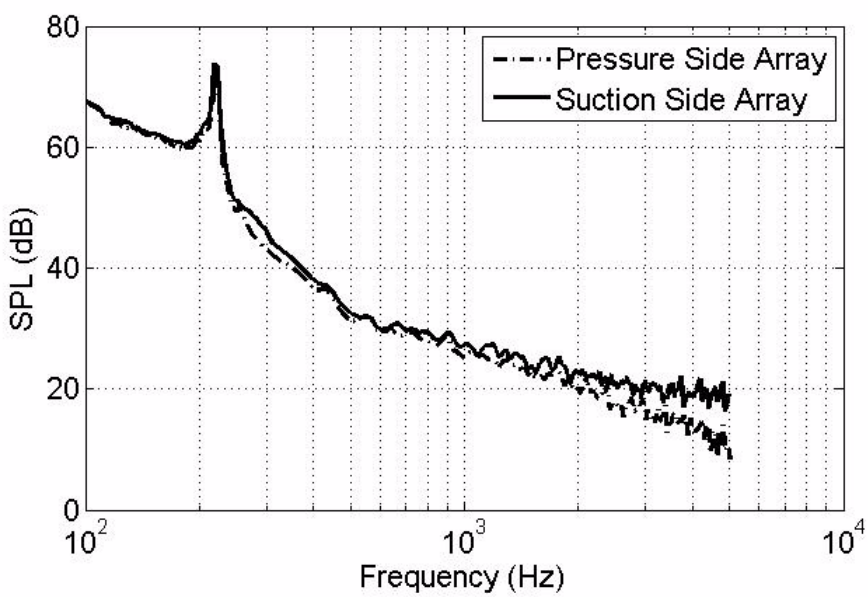

Figure 7.5: Comparison between trailing edge spectra obtained from the pressure and suction side array at Re = 1.9×10^6.

array. The cambered geometry likely influences the acoustic propagation of the trailing edge sound as reflections off of the bevelled side increase the acoustic pressure at the suction side array.

The auto spectral density as measured by both arrays are shown in Figure 7.6 for Reynolds numbers ranging from $1.3\text{x}10^6$ to $1.9\text{x}10^6$. The abscissa has been non-dimensionalized by the wake thickness parameter y_f and the free stream velocity. The shedding frequency is shown to occur at a Strouhal number of approximately $\omega y_f / U_\infty \cong 1.15$ as previously measured utilizing hot-wire spectra in Section 4.2.4. An insert of the tonal noise has been included to better show the dependence of the vortex shedding noise on freestream velocity. There appears to be a relatively constant increasing velocity dependence in the broadband frequency range $(\omega y_f / U_\infty > 2)$. At the shedding frequency, however, the velocity dependence shows an increasing trend except at the highest Reynolds number, which is observed to have a comparatively smaller peak spectral values. This may be due to the fact that the parasitic tunnel noise generated at

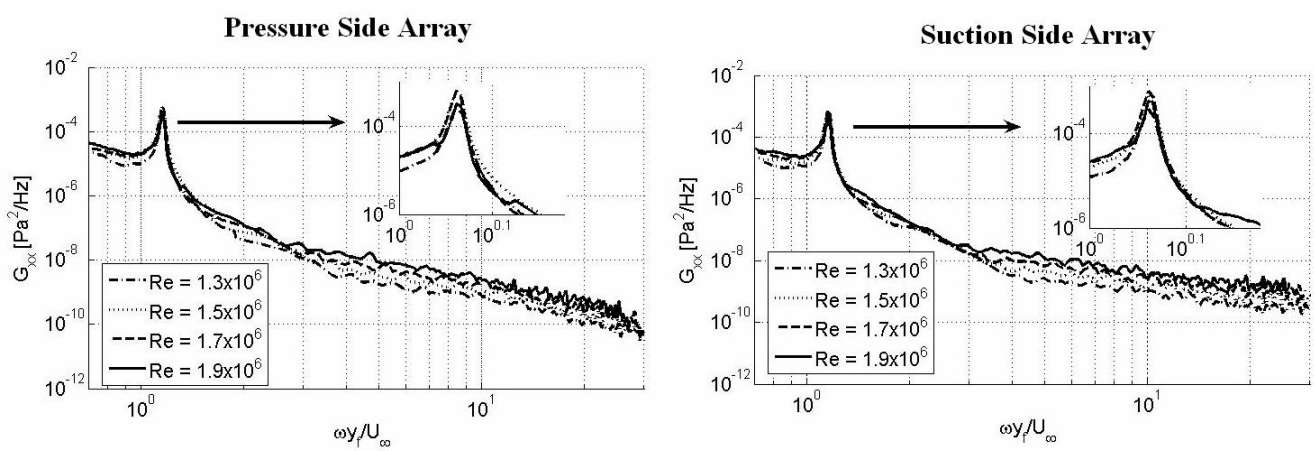

Figure 7.6: Trailing edge spectral density vs. scaled frequency for both arrays at Reynolds numbers ranging from $1.3\text{x}10^6$ to $1.9\text{x}10^6$.

TABLE 7.1

NON-DIMENSIONALIZED FREQUENCY BINS FOR

VELOCITY SCALING.

	Frequency Bin			
	$f < f_{shed}$	$f = f_{shed}$	$f = f_{intermediate}$	$f = f_{broadband}$
f_{center}	0.99	1.15	1.6	16.9
f_{range}	0.22	0.1	0.8	27.8

these frequencies scales as U_∞^8 decreasing the signal to noise ratio at the higher Reynolds numbers and interfering with the measurements of the peak tonal value.

The velocity scaling for the trailing edge noise was investigated over a range of seven Reynolds number ranging from $1.3\text{x}10^6$ to $1.9\text{x}10^6$. For this investigation the data were non-dimensionalized to scale the vortex shedding frequencies appropriately. Four specific frequency ranges were defined in order to separate the different flow mechanisms responsible for trailing edge noise production. The range and centering frequency for each of these frequency bins are shown in Table 7.1. First, the vortex shedding noise was confined to a single frequency bin such that $1.1 < \omega y_f / U_\infty < 1.2$. Frequencies lower than vortex shedding were also separated into a single frequency bin. A broadband frequency range was defined as $\omega y_f / U_\infty > 3$ and was separated into ten frequency bins. Finally, the range of frequencies between the tonal and broadband frequencies $1.1 < \omega y_f / U_\infty < 3$ was interpreted as an intermediate range. This intermediate frequency range was separated in order to separate the “drop-off” region between the tonal and broadband frequency ranges. Note that $\omega y_f / U_\infty < 3$ was were the signal to noise ratio was observed to be the smallest.

The velocity scaling was found by solving for the adjusted SPL (6.14). The optimal value of n was the value which produced the minimum variance in adjusted SPL over all the Reynolds number is shown in Figure 7.7 for both arrays. The ideal velocity dependence of radiated sound for a non-compact source distribution due to the flow of turbulence over an infinite half-plane (Ffowcs Williams and Hall, 1970) is shown for reference ($n = 5$). This U_∞^5 scaling appears to be appropriate at least for the higher frequencies where the relative beamwidth and spanwise turbulent length scales were much smaller than the model span. At the lower frequencies $(\omega y_f / U_\infty < 4)$ this scaling may be inappropriate as the source region becomes more compact in comparison to the acoustic wavelength.

Figures 7.8 and 7.9 shows the power spectral density for both arrays with an equivalent U_∞^5 scaling achieved by applying the dynamic pressure and free stream Mach number appropriately. As expected the broadband frequency range scales well for this range of Reynolds numbers. The frequency ranges on either side of the tonal noise does

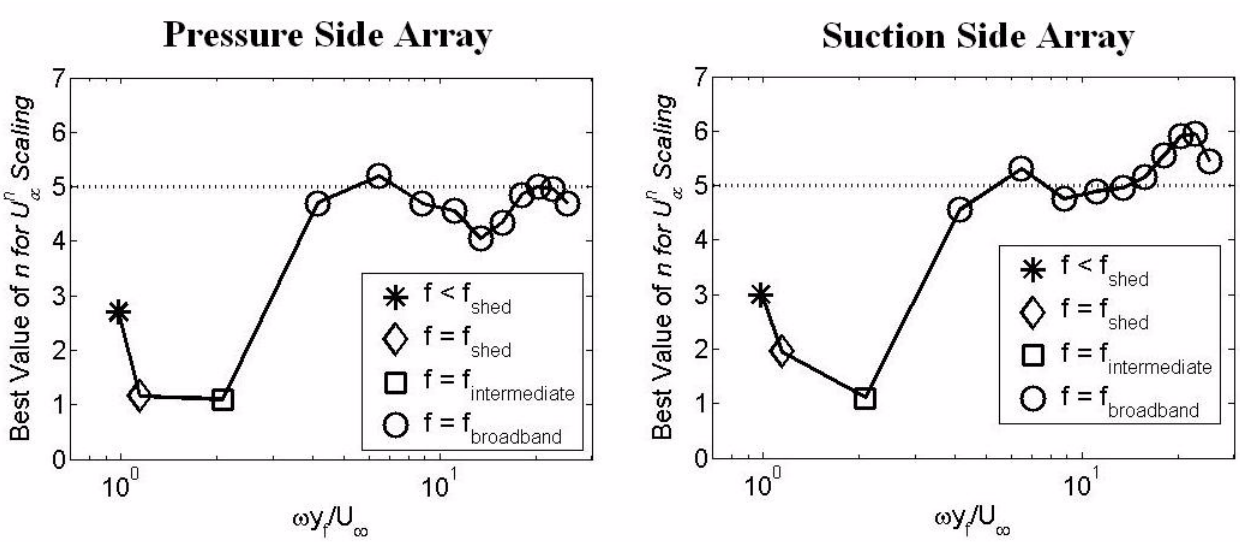

Figure 7.7: Optimal value of n for U^n scaling of trailing edge noise for both arrays.

not scale as U_∞^5 which may be due to increased of tunnel noise with respect to the trailing edge sound at frequencies where the beamforming methods are not as effective. Inserts show the detail of the tonal noise in Figures 7.8 and 7.9. For the lower Reynolds number the vortex shedding noise scales at U_∞^5, but this trend appears to be inappropriate for the Reynolds number above $1.7\text{x}10^6$.

The optimal velocity scaling for only the Reynolds numbers below $1.7\text{x}10^6$ is shown in Figure 7.10. The scaling at the tonal frequency for the pressure side array is much higher ($n \sim 6$) for this Reynolds number range. This U_∞^6 scaling may be appropriate as the acoustic wavelength is much larger than the model span at the shedding frequencies. The suction side shows a slightly lower scaling for the tonal noise in the lower Reynolds

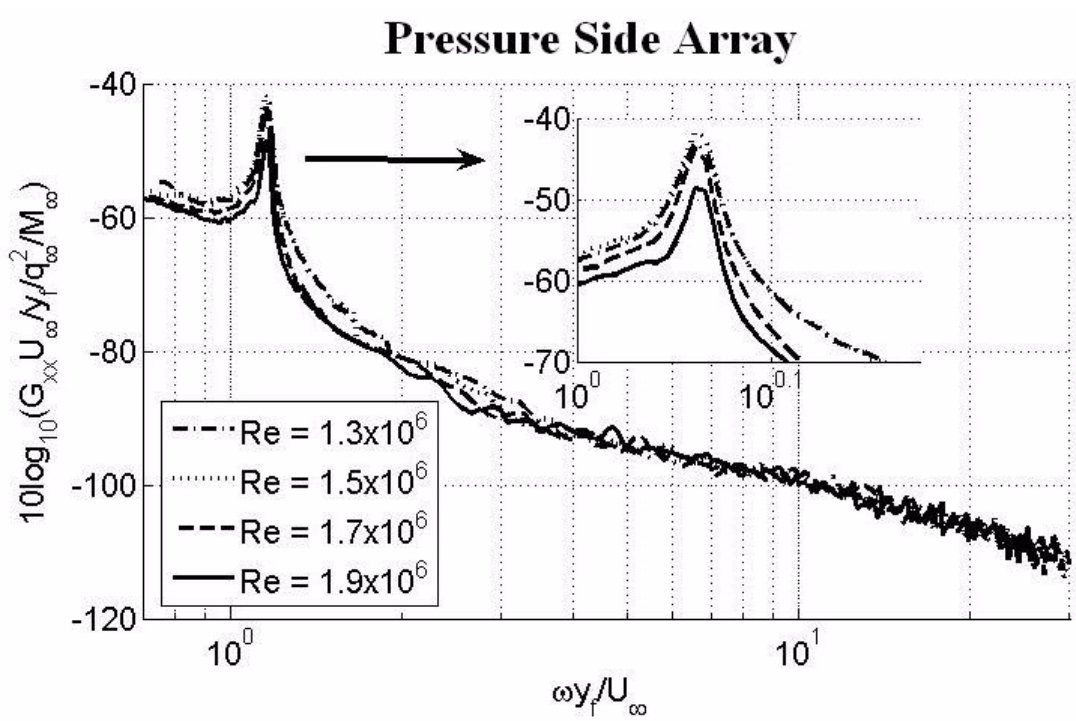

Figure 7.8: Trailing edge spectral density scaled as U_∞^5 for pressure side array at Reynolds numbers ranging from $1.3\text{x}10^6$ to $1.9\text{x}10^6$.

number range. The broadband sound showed very little scaling differences between Figures 7.7 and 7.10.

7.3 Comparison with Numerical Results

Wang et. al. (2006) computed the flow field for the bevelled trailing edge geometry using LES. The aeroacoustic noise was predicted using an integral-form Lighthill equation and the half-plane Green's function. A comparison of the experimental results presented this in report and the LES computations is shown in Figure 7.11. The computational domain was $2y_f$ (1/12th of the span of the experimental model), thus, the tonal noise was not accurately predicted due to spanwise correlation length scales on the same order as the computational domain size (see Figure 5.4). For an intermediate range of frequencies

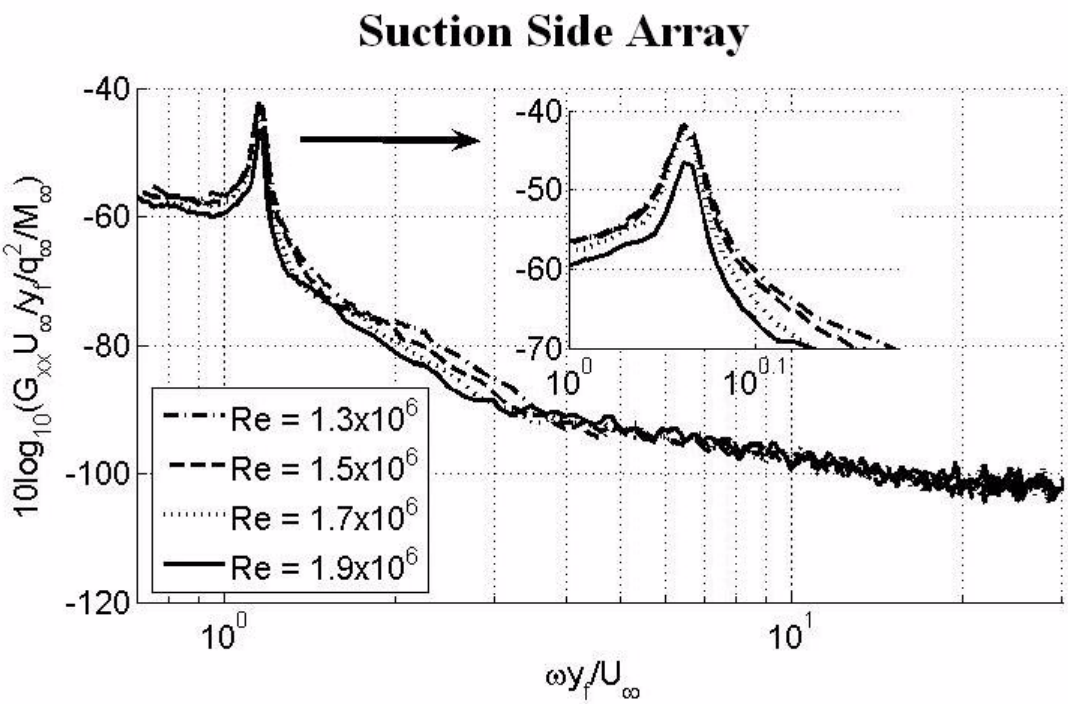

Figure 7.9: Trailing edge spectral density scaled as U_∞^5 for suction side array at Reynolds numbers ranging from $1.3\text{x}10^6$ to $1.9\text{x}10^6$.

$(2 < \omega y_f / U_\infty < 10)$ the spectral values match very well with both the pressure and suction side array results. At the higher frequencies there is relatively good agreement with the experimental and numerical results, especially for the pressure side array where the half-plane Green's function should better approximate the true Green's function.

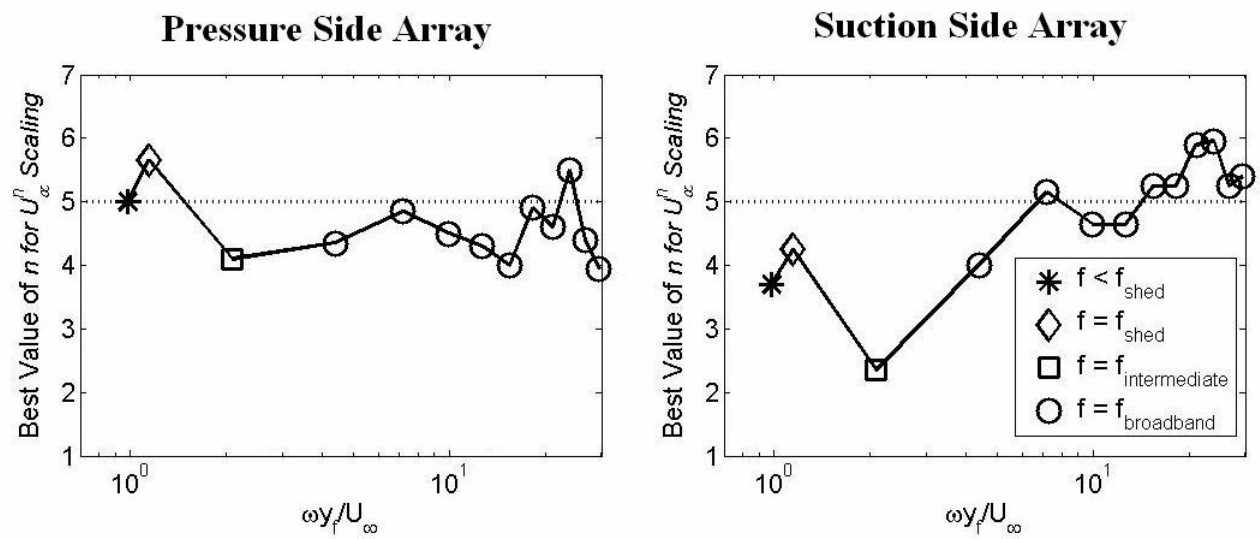

Figure 7.10: Optimal value of n for U^n scaling of trailing edge noise only for Reynolds numbers below 1.7×10^6.

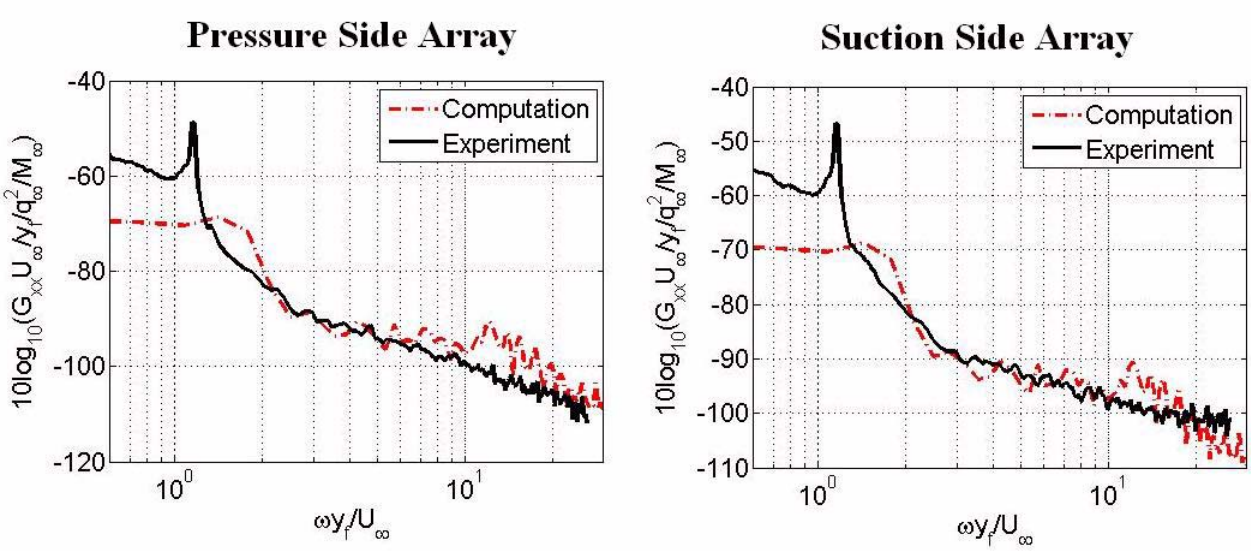

Figure 7.11: Comparison of experimental acoustic spectra to LES the prediction of trailing edge noise at Re = 1.9×10^6.

Discrepancies between the experimental and numerical results are likely the result the fact that the Green's functions are dissimilar. The use of the half-plane Green's function for the numerical predictions will include errors at frequencies where λ_a is of the same order as the model thickness (f $\lesssim$ 6800Hz) and where λ_a is of the same order as the model chord (f $\gtrsim$ 380Hz). This corresponds to a non-dimensional frequency range of $2 \lesssim \omega y_f / U_\infty \lesssim 35.6$ for the case shown in Figure 7.11. The Green's function related to the experimental results was also non-ideal because of the presence of the test geometry shown in Figure 4.1. Despite these discrepancies the results show good agreement between the experimental and numerical results.

7.4 Acoustic-Surface Pressure Correlations

It is of interest to study the correlation function between the unsteady surface pressure and the radiated acoustic field. Both surface pressure and phase array data were taken simultaneously in the AWT. The coherence function between surface pressure sensors E (suction side) and F (pressure side) and the beamformed acoustic signal from the suction side array is shown in Figure 7.12. These sensors were chosen because of their proximity to the sharp edge of the model. The acoustic propagation time between the surface pressure sensors and the array microphones was accounted for by the addition of a time delay to the surface pressure signals. This time delay was determined by the travel time of an acoustic wave from the mid-span of the model to the center of the array. The correlation function between the beamformed far field acoustic pressure signal (p') and the unsteady surface pressure (p) was computed using

$$\gamma(\omega)^2 = \frac{\left|G_{p'p}(\omega)\right|^2}{\sqrt{G_{p'p'}(\omega)}\sqrt{G_{pp}(\omega)}}, \tag{7.1}$$

where $G_{p'p'}$ and G_{pp} are the respective auto-correlation functions and $G_{p'p}$ is the cross-correlation function between the two signals.

The unsteady surface pressure and far field acoustic pressure were highly correlated at the vortex shedding frequency. It is of interest to note that the correlation of the pressure side sensor is much larger than that for the suction side sensor. This indicates that the tonal noise was more highly correlated with the large scale pressure fluctuations on the pressure side of the trailing edge. The PIV results have suggested that the flow originating from the lower boundary layer produces the most coherent structures related to the wake instability. It is these large scale structures that appear to be responsible for a majority the tonal noise produced by the trailing edge. This hypothesis is supported by the strong correlation at the shedding frequencies between the far field acoustics and the

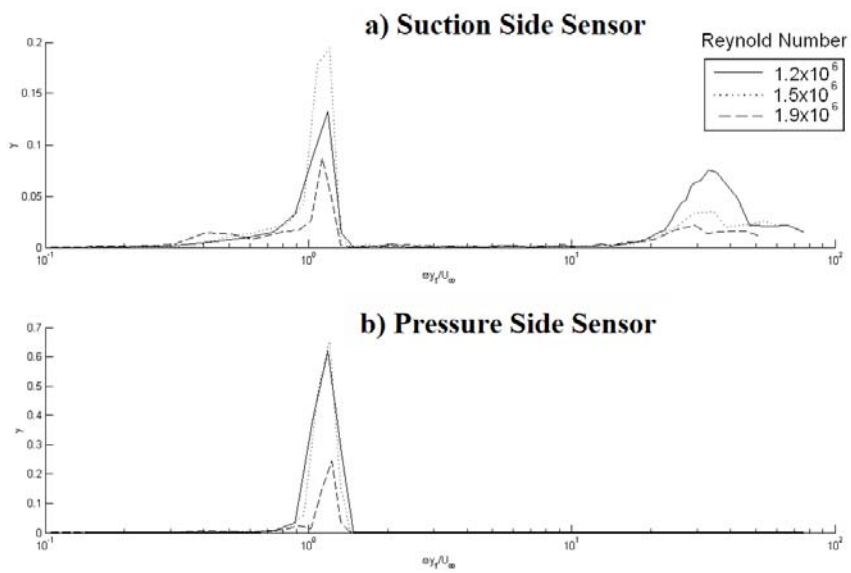

Figure 7.12: Coherence between beamformed acoustic signal and two unsteady surface pressure sensors located on pressure and suction side of sharp trailing edge.

pressure side unsteady surface pressure. The diminished tonal noise for the Re = 1.9×10^6 case is also observed in the correlation data for the pressure side sensor. This may be due to contamination of the acoustic signal by collector noise.

The only statistically significant correlation in the broadband frequency range was from the suction side surface pressure sensor. The small scale pressure fluctuations in the lower boundary layer just upstream of the sharp edge appear to have little correlation with the radiated broadband noise. This may be due in part to the fact the small scale turbulence may have changed its character by the time it has convected the 12.7mm from the pressure sensor to the sharp edge. However, this suggests that the high frequency pressure fluctuations located in the separated region above the trailing edge are more directly related to the radiated broadband sound than those in the boundary layer near the sharp trailing edge. The phase modulation of the broadband surface pressure at sensor E was observed to have a greater magnitude (Figure 5.5), implying that this modulation may be radiated to the far field.

7.5 Phase Averaged Acoustic Pressure

The acoustic pressure was phase averaged in a manner similar to the methods described in Section 5.3. The phase modulation of the broadband noise measured by the phased microphone array is illustrated in Figure 7.13. It can be seen that the oscillations about the phase mean were not as sinusoidal as was observed for the surface pressure. Rather, the oscillations remain below the phase mean for the majority of the shedding cycle and then “spike” well above this threshold for approximately 3/8 of the cycle. An apparent phase shift of the broadband “spike” was also observed for the lowest Reynolds number case. The same Reynolds number dependence of the phase averaged surface

pressure seen in Figure 5.5 was not observed for the phase averaged broadband noise. This may have resulted from the increase of unwanted (parasitic) sound produced by the operation of the AWT at the higher free stream velocities. There results support the conclusions about the phase modulation of broadband noise made in section 5.3.

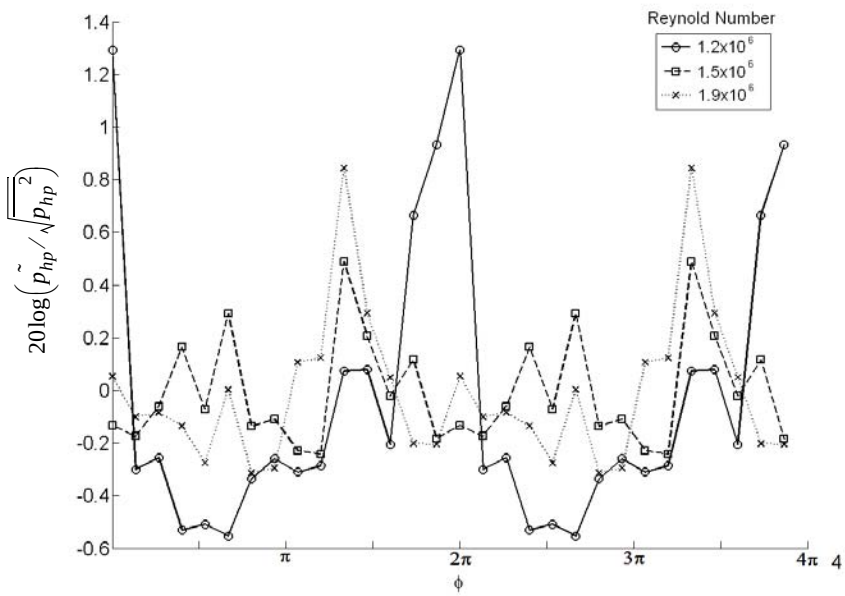

Figure 7.13: Broadband sound as a function of vortex shedding phase. Referenced to the broadband root mean square pressure.

CHAPTER 8

OPTIMIZED TRAILING EDGE SOUD MEASUREMENTS

The trailing edge geometry shown in Figure 1.1 was optimized by Wang et. al. (2006) in order to reduce the tonal noise produced by the trailing edge. The optimization techniques employed are summarized in Marsden et. al. (2004a and 2004b). The optimized geometry is shown in Figure 8.1. The curvature over the suction side of the optimized geometry was reduced and will produce a more gradual pressure gradient, thereby, delaying and possibly eliminating flow separation over the upper surface of the model. The pressure side of the optimized geometry model is cambered such that a weak favorable pressure gradient will be initially generated until approximately *t*/2 upstream of the sharp edge where the surface curvature changes direction and then a weak adverse pressure gradient will be produced just before the trailing edge. The addition of adverse pressure gradients just before the separation of the boundary layers on either side of the model may tend to "pull" the boundary layer turbulence away from the sharp edge,

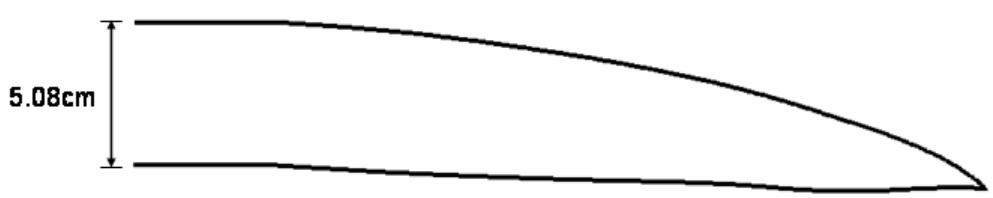

Figure 8.1: Sketch of optimized trailing edge geometry.

thereby, reducing the noise by moving turbulent source terms away from regions where the acoustic Green's function will be relatively large. The optimized geometry also makes a sharper angle of approximately 22 degrees making the edge appear more symmetrical than the original geometry. This suggests that the Green's function associated with the optimized edge will possibly be better approximate by a half plane Green's function.

In order to validate the numerical results for the optimized trailing edge sound measurements were acquired in the AWT in the same manner as previously described for the original trailing edge geometry.

8.1 Beamforming Maps for Optimized Trailing Edge

Figures 8.2 and 8.3 presents the beamforming maps for the optimized tailing edge and both pressure and suction side array, respectively. The frequencies illustrated are 352, 508, 1992, and 4004Hz at a chord Reynolds number of 1.9×10^6. The positions of the inlet, end plates, and collector are identical for those presented previously in Figures 7.1 and 7.2. The vertical dashed line at X_b = 0cm represents the location of the sharp trailing edge in the test section. Images (a)-(d) show the weighted CSM results and images (e)-(h) show the DAMAS results.

The trailing edge source in Figures 7.1 and 7.2 was observed to be separated from the parasitic tunnel source for frequencies at frequencies above around 500Hz. At frequencies below this value the trailing edge noise was observed to be intermixed with the inlet or collector noise meaning the spectral values will not be indicative of the trailing edge noise. Otherwise, the spectral values in the trailing edge region appear to be similar to those found in Section 7.1.

8.2 Optimized Trailing Edge Spectra

Spectra for the optimized trailing edge geometry were obtained in a manner similar to that described in Section 7.2. A combination of the weighted CSM and DAMAS methods were utilized to produce the spectral values. The delay-sum beamforming was not utilized as it was found to have no advantages over the weighted CSM and DAMAS methods over any frequency ranges. The DAMAS method was found to be most

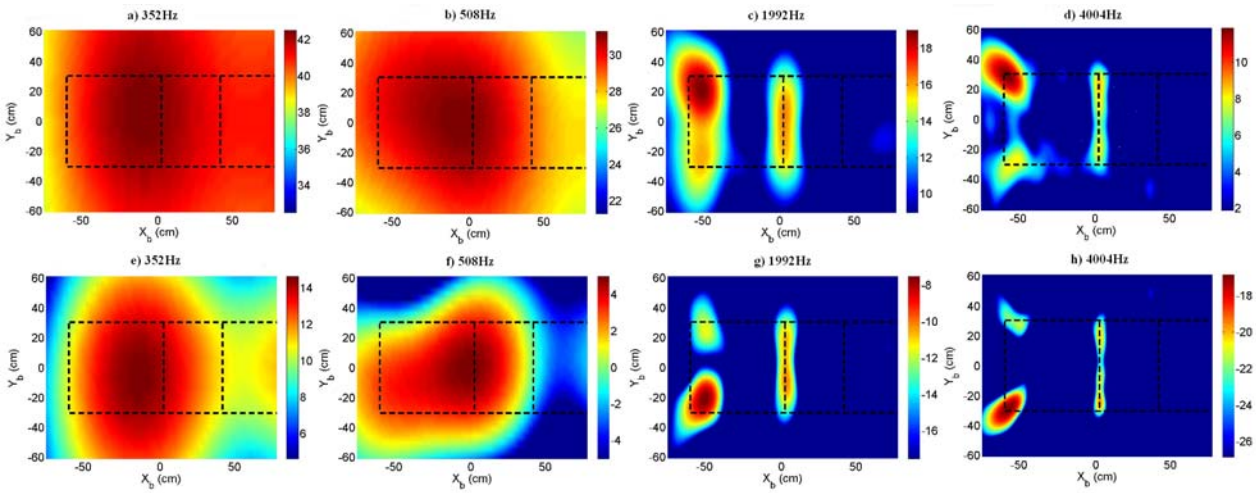

Figure 8.2: Beamforming (a-d) and DAMAS (e-h) maps for optimized trailing edge on pressure side phased array at $Re_c = 1.9x10^6$. Flow is from left to right.

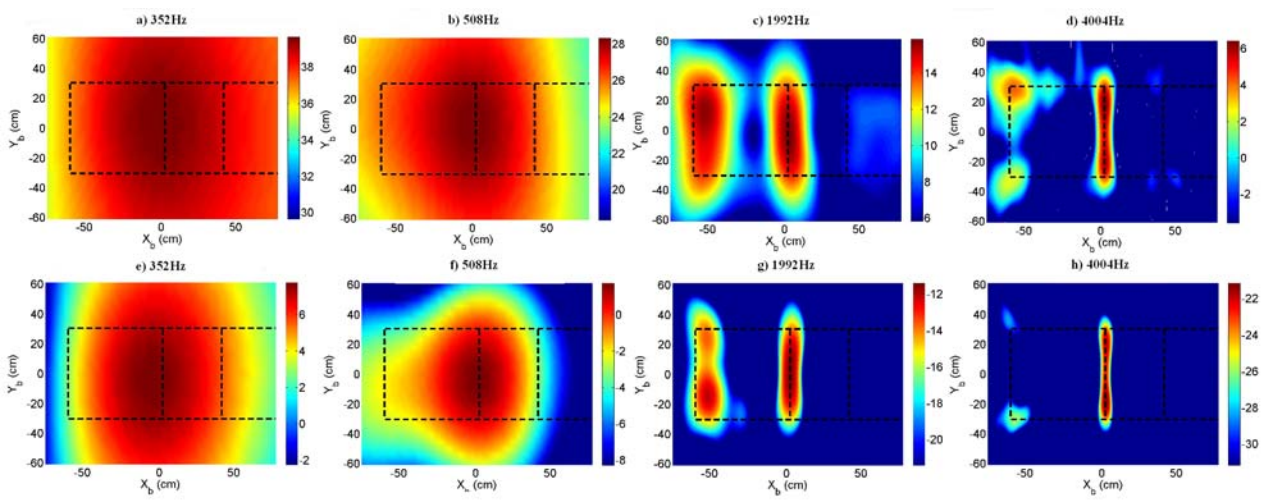

Figure 8.3: Beamforming (a-d) and DAMAS (e-h) maps for optimized trailing edge on suction side phased array at $Re_c = 1.9x10^6$. Flow is from left to right.

advantageous for frequencies above 550Hz. DAMAS was not possible for frequencies below 550Hz because the PSF does not have converging contour lines. The weighted CSM beamforming method was used for frequencies below this value.

The spectra for the optimized trailing edge and both arrays at chord Reynolds numbers of 1.3×10^6 and 1.9×10^6 are shown if Figure 8.4 and 8.5 compared with the spectra for the original trailing edge spectra and the empty tunnel background noise. It should be noted again that the background noise in these figures is not the true background noise because it was measured without the model in place. The additional camber associated with the optimized trailing edge model was found to create more parasitic tunnel noise than was observed with the original trailing edge geometry as the added lift modified the open jet shear layers in a more pronounced manner. Due to both these factors and the fact that the sound produced by the optimized trailing edge was reduced at the lower frequencies the signal to noise ratio below approximately 500Hz is greatly

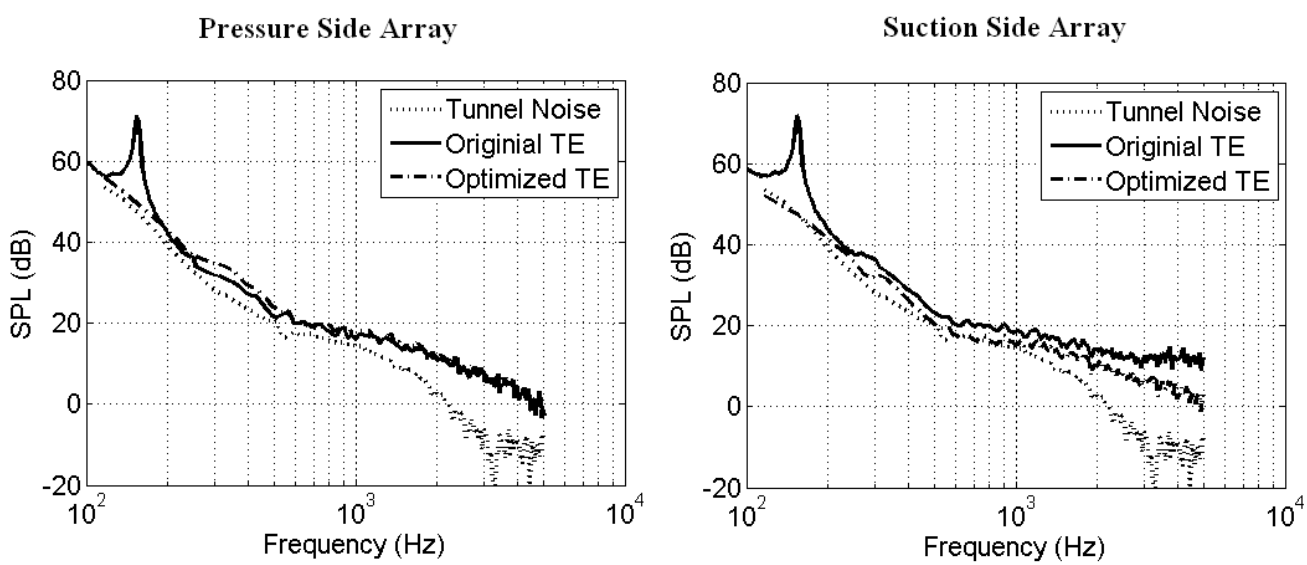

Figure 8.4: Optimized trailing edge spectra compared to that of a single microphone for trailing edge data at Re = 1.3×10^6.

increased such that the spectra in Figures 8.4 and 8.5 below this value should be interpreted as mostly parasitic tunnel noise.

The optimization of the original trailing edge geometry by Meng et. al. (2006) was successful in eliminating the relatively large contribution of the tonal noise to the total sound produced by the trailing edge as no tonal noise was observed at any of the Reynolds number investigated. This appears to have been accomplished by reducing or eliminating the separation region over the suction side of the model. PIV measurements in Chapter 3 showed that large scale vortical structures "rolled up" into the low momentum recirculation region caused by the separation of the pressure side boundary layer. The reduction or removal of this region appears to have eliminated the tonal noise produce by any vortex shedding motions that may still exist.

At frequencies above 500Hz the optimized trailing edge spectra on the pressure side of the model are nearly identical to that of the original geometry. For the suction side of the model the trailing edge sound has been appreciably reduced in comparison to the

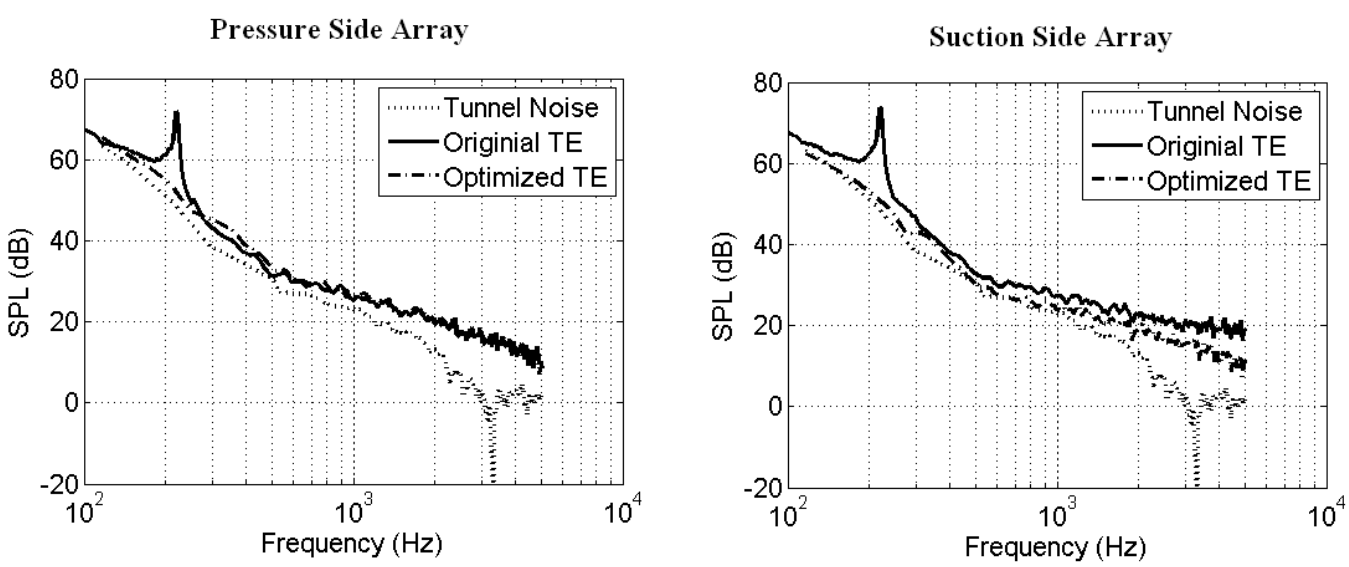

Figure 8.5: Optimized trailing edge spectra compared to that of a single microphone for trailing edge data at Re = 1.9×10^6.

original trailing edge noise. This may be due to the fact that the Green's function for the optimized geometry would be expected to be more symmetrical, causing the trailing edge noise to radiate more equally than was observed for the original geometry. In Chapter 3 the sound generated in this frequency range for the original geometry was found to be generated mostly by boundary layer turbulent from the pressure side of the model.

A comparison between the radiated pressure spectra as measured between the pressure side and suction side arrays is shown in Figure 8.6 at Re = 1.9×10^6. There is relatively good agreement between the radiated sound field for frequencies higher than 2000Hz. Below this value the spectra for the pressure side array are slightly higher. This is possibly due to the asymmetry of the optimized trailing edge geometry. The spectral values below 500Hz show that the parasitic noise measured on the pressure side of the optimized geometry was elevated for the pressure side array.

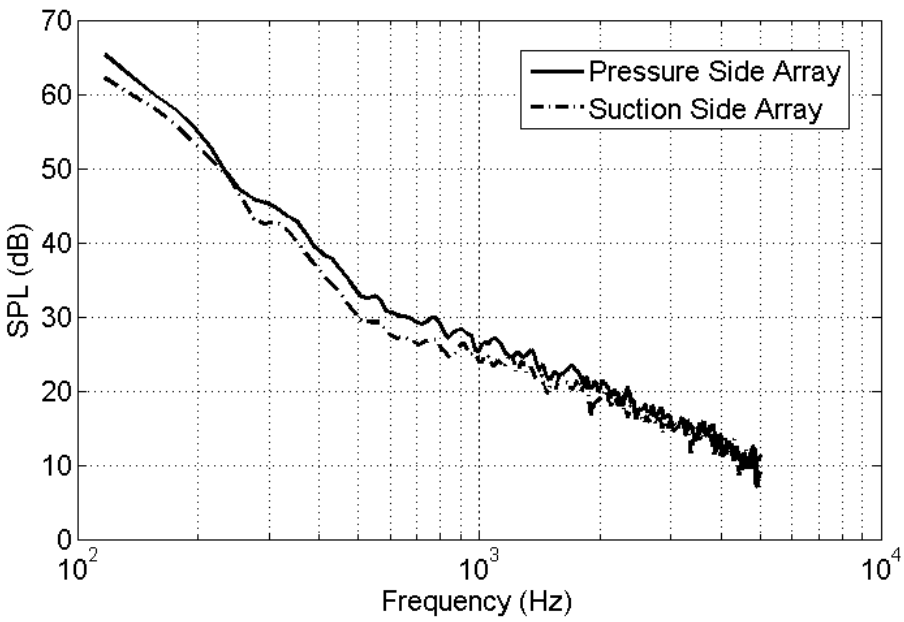

Figure 8.6: Comparison between the optimized trailing edge spectra obtained from the pressure and suction side array at Re = 1.9×10^6.

The auto spectral density as measured by both arrays are shown in Figure 8.7 for Reynolds numbers ranging from $1.3\text{x}10^6$ to $1.9\text{x}10^6$. The velocity scaling appears to be approximately constant for the range of frequencies shown. This velocity scaling for the optimized trailing edge noise was further investigated and the optimal value of *n* (6.14) in each 1/12th octave band is shown in Figure 8.8 for both arrays. Only value above 500Hz are shown in order to eliminate any possible effects that the tunnel noise might have on the

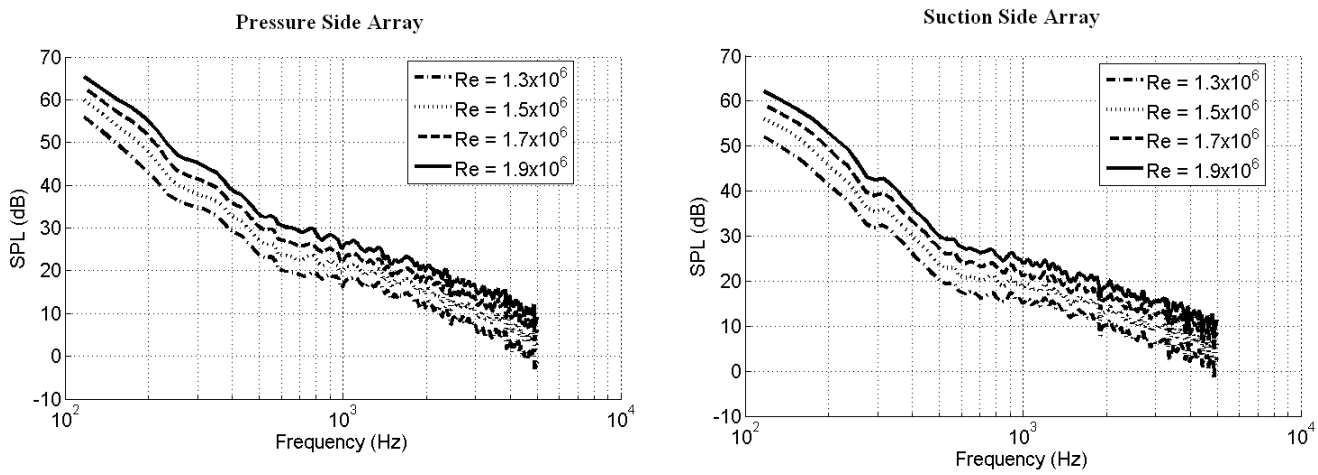

Figure 8.7: Optimized trailing edge spectral density vs. scaled frequency for both arrays at Reynolds numbers ranging from $1.3\text{x}10^6$ to $1.9\text{x}10^6$.

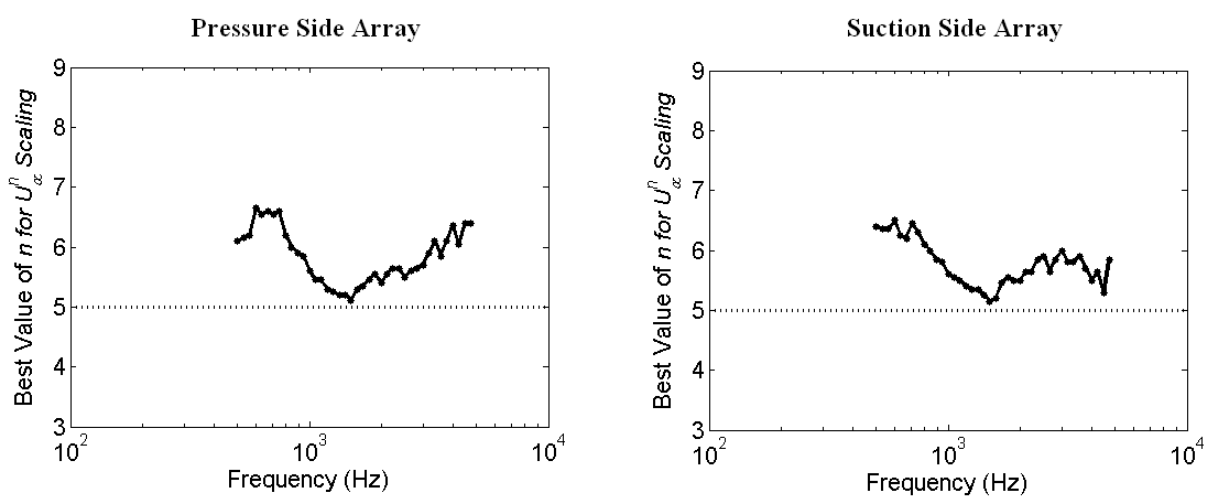

Figure 8.8: Best value of *n* for U^n scaling of optimized trailing edge noise for both arrays.

interpretation of these data. The velocity scaling fluctuates between U_∞^5 and U_∞^6. This implies that the edge is behaving somewhere between a compact source and a non-compact distribution of sources (Ffowcs Williams and Hall, 1970).

Figures 8.9 and 8.10 shows the power spectral density for both arrays with an equivalent U_∞^5 scaling achieved by applying the dynamic pressure and free stream Mach number appropriately. The broadband frequency range scales well for this range of Reynolds numbers. The frequencies lower than $\omega t / U_\infty \sim 9$ show what appear to be an increased velocity scaling. This may be due to the reduced signal to noise ratio at these frequencies.

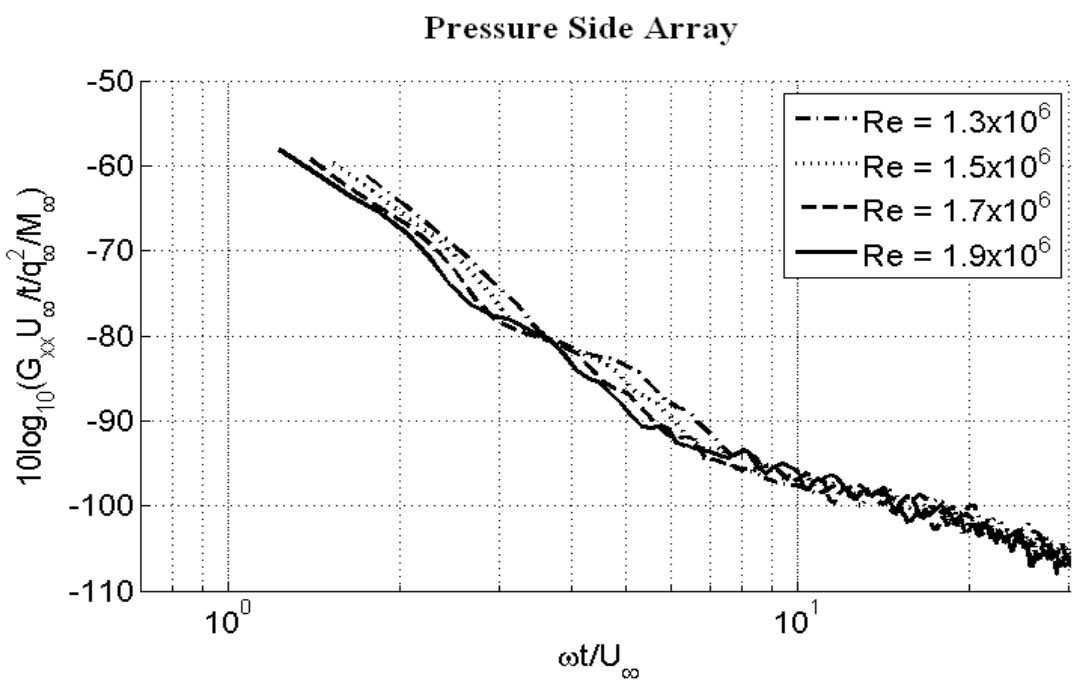

Figure 8.9: Optimized trailing edge spectral density scaled as U_∞^5 for pressure side array at Reynolds numbers ranging from $1.3\text{x}10^6$ to $1.9\text{x}10^6$.

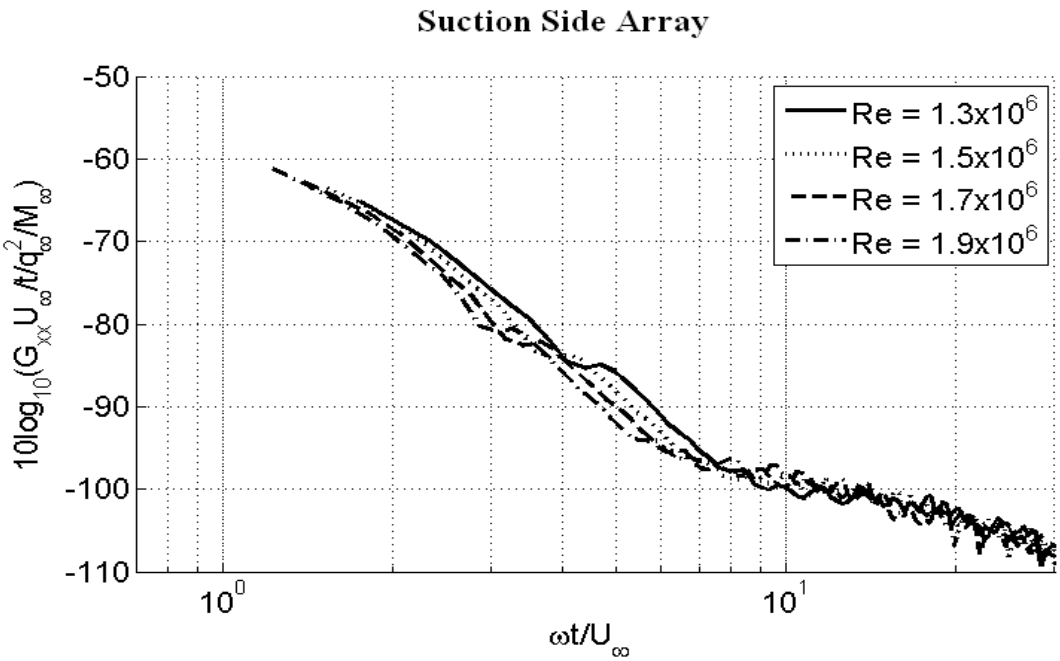

Figure 8.10: Optimized trailing edge spectral density scaled as U_∞^5 for suction side array at Reynolds numbers ranging from $1.3\text{x}10^6$ to $1.9\text{x}10^6$.

CHAPTER 9

CONCLUSIONS

The main objective of this project was to experimentally investigate the production of sound by self-generated turbulence over an airfoil with an asymmetric blunt trailing edge. This was achieved by acquiring various flow velocity and acoustic pressure measurements. The model used in this study allowed for the investigation of both tonal sound produced by large scale vortex shedding turbulence and broadband sound generated by smaller scale boundary layer turbulence. The model has also been previously documented in the literature.

Several measurement techniques were utilized in this project. Single point velocity measurements were acquired utilizing hot-wire anemometry. These measurements documented the boundary conditions relevant to the production of trailing edge sound (i.e. boundary layer thickness, wake thickness parameter y_f, and wake velocity profiles). PIV measurements of the velocity field at the trailing edge were obtained and allowed for resolution of the spatial characteristics relevant to the turbulent motions responsible for the production of trailing edge sound. In addition, the sound generated by the trailing edge was measured using a pair of phased microphone arrays in conjunction with several beamforming techniques.

The major conclusions drawn from this study are summarized below.

- The existence of large scale vortex shedding was observed in the near wake region of the trailing edge. Independent acoustic, surface pressure, and hot-wire measurements have confirmed the shedding frequency to be $2\pi f y_f / U_\infty = 1.15$, which is consistent with other published results. A phase averaged decomposition of the PIV data with respect to the vortex shedding was completed utilizing a new method based on a Karhunen-Loeve decomposition of the velocity field. This separated the velocity fluctuations occurring at the vortex shedding frequency from those occurring at higher frequencies and allowed for the direct examination of the turbulent motions responsible for tonal noise (phase average component) and broadband noise (phase fluctuating component). It was observed that the turbulence originating from the suction side boundary layer did not come into close proximity to the sharp trailing edge due to separation suggesting that little broadband noise will be generated by these turbulent motions. Conversely, the pressure side boundary layer turbulence was found to produce large coherent vortical structures in the near vicinity of the sharp edge as the boundary layer vorticity shed into the near wake. This implied that the majority of broadband sound produced by this trailing edge was most likely generated principally by smaller scale turbulent fluid motions origination from the pressure side boundary layer.
- Delay-sum, weighted CSM, and DAMAS beamforming algorithms were utilized to analyze the array data. The ability of these methods to ignore unwanted tunnel noise was investigated as a function of frequency and each method was found to be advantageous over differing frequency ranges. Specifically, the delay-sum and weighted CSM methods were found to work best in the lower frequency ranges

(below 500Hz), where DAMAS will not work due to prohibitively large acoustic wavelengths. Above 500Hz DAMAS was found to obtain the best results.

- The velocity scaling of the tonal noise produced by the vortex shedding was approximately U_∞^6 in the tonal frequency band for the pressure side array for tunnel speeds where the low frequency tunnel noise did not interfere with the trailing edge noise. This may be appropriate given the compactness of the source at the tonal frequency. The suction side array showed a lower velocity scaling of approximately $U_\infty^{4.5}$. This may have been due to the asymmetry of the trailing edge geometry and/or the fact that the measurements were acquired in the near field at the tonal frequency.
- The broadband sound generated by boundary layer turbulence as it encountered the trailing edge was found to scale as approximately U_∞^5 for both arrays, which is the same result obtained for a non-compact acoustic source caused by flow over an infinite half-plane. The spectral values for the broadband sound acquired from the suction side array were appreciably higher (2-8dB) than those from the pressure side array. This was possibly due to the model asymmetry as acoustic reflections off of the bevelled surface of the trailing edge may have increased the observed sound levels on the suction side of the model.
- Comparison of the measured trailing edge acoustic spectra to the numerical LES computations completed by Wang et al. (2006) show good agreement especially in an intermediate frequency range where the assumed half-plane Green's function used in the numerical results was most appropriate. In addition, the sound produced by an optimized trailing edge geometry in Wang et al. was also measured.

The optimized shape was observed to successfully eliminate the tonal noise generated by the original trailing edge geometry. The velocity scaling for the noise generated by the optimized geometry was found to be between U_∞^5 and U_∞^6. The spectral values measured on either side of the model showed similar magnitudes over the entire frequency range. The broadband noise measured by the pressure side array were similar for both the original and optimized trailing edge geometries. For the suction side array the optimized trailing edge showed reduced SPL values. This is most likely due to the sharper tip geometry of the optimized edge rather than a significant change in the acoustic source terms at these frequencies (i.e. the sharper tip caused a reduction in reflected sound off of the suction side surface).

REFERENCES

Blake, W. K. (1986). Mechanics of flow-induced sound and vibration. Orlando, FL: *Academic Press*.

Blake, W. K. (1975). A statistical description of pressure and velocity fields at the trailing edges of a flat strut No. 4241). Bethesda, MD: *David W. Taylor Naval Ship Research and Development Center.*

Blake, W. K., & Gershfeld, J. L. (1989). The aeroacoustics of trailing edges. In M. Gad-El-Hak (Ed.), Frontiers in experimental fluid mechanics (pp. 457-532). Berlin and New York: *Springer-Verlag*.

Brooks, T. F., & Hodgson, T. H. (1981). Trailing edge noise prediction from measured surface pressures. *Journal of Sound and Vibration*, 78(1), 69-117.

Brooks, T. F., & Humphreys, W. M. (2006). Extension of DAMAS phased array processing for spacial coherence determination (DAMAS-C). *12th AIAA/CEAS Aeroacoustics Conference*, Boston, MA.

Brooks, T. F., & Humphreys, W. M. (2004). A deconvolution approach for the mapping of acoustic sources (DAMAS) determined from phased microphone arrays. *10th AIAA/CEAS Aeroacoustics Conference*, Manchester, UK.

Curle, N. (1955). The influence of solid boundaries upon aerodynamic sound. *Proceedings of the Royal Society of London. Series A, Mathematical and Physical Sciences*, 231, 505-514.

Devenport, W. J., Muthanna, C., Ma, R., & Glegg, S. (2001). Two-point descriptions of wake turbulence with application to noise prediction. *American Institute of Aeronautics and Astronautics*, 39, 2302-2307.

Dougherty, R. P. (2005). Extensions of DAMAS and benefits and limitations of deconvolution in beamforming. *11th AIAA/CEAS Aeroacoustics Conference*, Monterey, CA.

Dougherty, R. P. (2002). Beamforming in acoustic testing. In T. J. Mueller (Ed.), Aeroacoustics measurements (pp. 62-97). Berlin: *Springer-Verlag*.

Ehrenfried, K., & Koop, L. (2006). A comparison of iterative deconvolution algorithms for the mapping of acoustic sources. *12th AIAA/CEAS Aeroacoustics Conference*, Boston, MA. , AIAA-2006-2711

Ffowcs Williams, J. E., & Hawking, D. L. (1969). Sound generation by turbulence and surfaces in arbitrary motion. *Philosophical Transactions of the Royal Society of London Series A-Mathematical Physical and Engineering Sciences*, 264, 321-342.

Ffowcs Williams, J. E., & Hall, L. H. (1970). Aerodynamics sound generation by turbulent flow in the vicinity of a scattering half-plane. *Journal of Fluid Mechanics*, 40, 657-670.

Gershfeld, J. L., Blake, W. K., & Knisely, C. W. (1988). Trailing edge flows and aerodynamic sound. *AIAA Thermophysics, Plasmadynamics and Lasers Conference*, San Antonio, TX. 2133-2140.

Holmes, P., Lumley, J. L., & Berkooz, G. (1996). Turbulence, coherent structures, dynamical systems and symmetryCambridge University Press.

Howe, M. S. (2003). Theory of vortex sound. *Cambridge University Press*.

Howe, M. S. (1999). Trailing edge noise at low mach number. *Journal of Sound and Vibration*, 225(2), 211-238.

Howe, M. S. (1978). A review of the theory of trailing edge noise. *Journal of Sound and Vibration*, 61(3), 437-465.

Howe, M. S. (1975). Contributions to the theory of aerodynamic sound, with application to excess jet noise and the theory of the flute. *Journal of Fluid Mechanics*, 71, 625-673.

Lee, Y. T., Blake, W. K., & Farabee, T. M. (2005). Modeling of wall pressure fluctuations based on time mean flow field. *Journal of Fluids Engineering*, 127, 233-240.

Lighthill, M. J. (1952). On sound generated aerodynamically. I. general theory. *Proceedings of the Royal Society of London. Series A, Mathematical and Physical Sciences*, 221, 564-587.

MacDonald, H. M. (1915) A class of diffraction problems. *Proceedings of London Mathematical Society*, 14, 410-427.

Mardson, A. L., Wang, M., Dennis, J. E., & Moin, P. (2004a). Optimal aeroacoustic shape design using the surrogate management framework. *Optimization and Engineering*, 5, 235-262.

Mardson, A. L., Wang, M., Dennis, J. E., & Moin, P. (2004b). Suppression of vortex shedding noise via derivative-free shape optimization. *Physics of Fluids*, 16(10), 83-86.

Mueller, T. J., Scharpf, D. F., Batill, S. M., Strebinger, R. B., Sullivan, C. J., & Subramanian, S. (1992). The design of a low-noise, low-turbulence wind tunnel for acoustic measurements. 1*7th AIAA Ground Testing Conference*, Nashville, TN.

Oberai, A. A., Roknaldin, F., & Hughes, T. (2002). Computation of trailing-edge noise due to turbulent flow over an airfoil. *AIAA Journal*, 40(11), 2206-2216.

Olson, S., & Mueller, T. J. (2004). Phases array acoustic imaging of an airfoil trailing edge flow. *11th International Symposium on Flow Visualization*, Notre Dame, IN.

Panton, R. J. (1996). Incompressible flow (2nd ed.). New York: *John Wiley & Son.*

Powell, A. (1964). Theory of vortex sound. *The Journal of the Acoustical Society of America*, (32), 982.

Roger, M., Moreau, S., & Guedel, A. (2006). Vortex-shedding noise and potential-interaction noise modeling by a reversed sears' problem. *12th AIAA/CEAS Aeroacoustics Conference*, Boston, MA. , 2006-2607

Scharpf, D. F. (1993). An experimental investigation of the sources of propeller noise due to turbulence ingestion. (Ph.D., University of Notre Dame).

Schroder, A., Dierksheide, U., Wolf, J., & Kompenhans, J. (2004). Investigation on trailing-edge noise sources by means of high-speed PIV. *12th International Symposium on Application of Laser Techniques to Fluid Mechanics*, Lisbon, Portugal.

Shannon, D. W., & Morris, S. C. (2006). Experimental investigation of a blunt trailing edge flow field with application to sound generation. *Experiments in Fluids*, 41(5), 777-788.

Shannon, D. W., Morris, S. C., & Mueller, T. J. (2006). Radiated sound and turbulent motions in a blunt trailing edge flow field. *International Journal of Heat and Fluid Flow*, 27(4), 730-736.

Underbrink, J. R. (1995). Practical considerations in focused array design for passive broad-band source mapping applications. (Masers, Pennsylvania State University).

Wang, M., Freund, J. B., & Lele, S. K. (2006). Computational prediction of flow generated sound, *Annual Reviews of Fluid Mechanics*, 38, 483-512.

Wang, M., & Moin, P. (2000). Computation of trailing-edge flow and noise using large-eddy simulation. *American Institute of Aeronautics and Astronautics*, 38, 2201-2209.